JETP Letters, Vol. 77, No. 7, 2003, pp. 335–338. From Pis'ma v Zhurnal Éksperimental'noĭ i Teoreticheskoĭ Fiziki, Vol. 77, No. 7, 2003, pp. 403–406.

Primordial Pairing and Binding of Superheavy Charged Particles in the Early Universe¶

V. K. Dubrovich*, [1] and M. Yu. Khlopov, ***, ****

** Special Astrophysical Observatory, Russian Academy of Sciences, St. Petersburg, 196140 Russia*

[1] *e-mail:dubr@MD1381.spb.edu*

*** Keldysh Institute of Applied Mathematics, Russian Academy of Sciences, Moscow, 125047 Russia*

**** Moscow Engineering Physics Institute, Moscow, 115409 Russia*

***** Physics Department, Università degli studi "La Sapienza," I 00185 Roma, Italy*

Received July 10, 2002; in final form, February 18, 2003

Primordial superheavy particles, considered as the source of Ultra High Energy Cosmic Rays (UHECR) and produced in local processes in the early Universe, should bear some strictly or approximately conserved charge to be sufficiently stable to survive to the present time. Charge conservation dictates that they be produced in pairs, and the estimated separation of particle and antiparticle in such a pair is shown to be in some cases much smaller than the average separation determined by the averaged number density of considered particles. If the new $U(1)$ charge is the source of a long-range field similar to the electromagnetic field, the particle and antiparticle, possessing that charge, can form a primordial bound system with an annihilation timescale, which can satisfy the conditions assumed for this type of UHECR source. These conditions severely constrain the possible properties of the considered particles. © *2003 MAIK "Nauka/Interperiodica".*

PACS numbers: 98.70.Sa; 98.80.Cq

The origin of cosmic rays with energies exceeding the GZK cutoff energy [1] is widely discussed, and one of the popular approaches is related to decays or annihilation in the Galaxy of primordial superheavy particles [2–5] (see [5] for review and references therein). The mass of such particles is assumed to be higher than the reheating temperature of the inflationary Universe, so it is assumed that the particles are created in some nonequilibrium processes, such as inflation decay [6] at the stage of preheating after inflation [7].

The problems related to this approach are as follows. If the source of ultrahigh-energy cosmic rays (UHECR) is related with particle decay in the Galaxy, the timescale of this decay necessary to reproduce the UHECR data needs a special nontrivial explanation. Indeed, the relic unstable particle should survive to the present time and, having mass m on the order of 10^{14} GeV or larger, should have the lifetime τ, exceeding the age of the Universe. On the other hand, even if particle decay is due to gravitational interaction and its probability is on the order of $1/\tau = (m/m_{Pl})^4 m$, where $m_{Pl} = 10^{19}$ GeV is the Planck mass, the estimated lifetime would be many orders of magnitude smaller. This implies some specific additional suppression factors in the probability of decay, which need a rather nontrivial physical realization [2, 5], e.g., in the model of cryptons [8] (see [9] for review).

If the considered particles are absolutely stable, the source of UHECRs is related with their annihilation in the Galaxy. But their averaged number density, constrained by the upper limit on their total density, is so low that a strongly inhomogeneous distribution is needed to enhance the effect of annihilation to the level desired to explain the origin of UHECR by this mechanism.

In the present note, we offer a new approach to the solution of the latter problem. If superheavy particles possess new $U(1)$ gauge charge, related to the hidden sector of particle theory, they are created in pairs. The Coulomb-like attraction (mediated by the massless $U(1)$ gauge boson) between particles and antiparticles in these pairs can lead to their primordial binding, so that the annihilation in the bound system provides the mechanism for UHECR origin.

Note, first of all, that in quantum theory particle stability reflects the conservation law, which according to Noether's theorem is related with the existence of a conserved charge possessed by the particle under consideration. Charge conservation implies that a particle should be created together with its antiparticle. This means that, being stable, the considered superheavy particles should bear a conserved charge, and such charged particles should be created in pairs with their antiparticles at the stage of preheating.

Being created in the local process of inflation field decay, the pair is localized within the cosmological horizon in the period of creation. If the momentum dis-

¶This article was submitted by the authors in English.

tribution of created particles peaks below $p \sim mc$, they do not spread beyond the proper region of their original localization, being in the period of creation $l \sim c/H$, where the Hubble constant H at the preheating stage is in the range $H_r \le H \le H_{end}$. Here, H_{end} is the Hubble constant at the end of inflation and H_r is the Hubble constant in the period of reheating. For relativistic pairs, the region of localization is determined by the size of the cosmological horizon in the period of their derelativization. In the course of successive expansion, the distance l between particles and antiparticles grows with the scale factor, so that, after reheating at the temperature T, it is equal to (here and further, if not indicated otherwise, we use the units $\hbar = c = k = 1$)

$$l(T) = \left(\frac{m_{Pl}}{H}\right)^{1/2}\frac{1}{T}. \quad (1)$$

The averaged number density of superheavy particles n is constrained by the upper limit on their modern density. If we take their maximum possible contribution in units of critical density, Ω_X, not to exceed 0.3, the modern cosmological average number density should be

$$n = 4\times 10^{-22}\frac{10^{14}\ \text{GeV}}{m}\frac{\Omega_X}{0.3}T^3.$$

This corresponds at the temperature T to a mean distance ($l_s \sim n^{-1/3}$) equal to

$$l_s \approx 1.6\times 10^{7}\left(\frac{m}{10^{14}\ \text{GeV}}\right)^{1/3}\left(\frac{0.3}{\Omega_X}\right)^{1/3}\frac{1}{T}. \quad (2)$$

$$\left(l_s \approx 4.6\times 10^{6}\left(\frac{m}{10^{14}\ \text{GeV}}\right)^{1/3}\left(\frac{0.3}{\Omega_X}\right)^{1/3}\text{cm}\right.$$

in ordinary units).

One finds that superheavy nonrelativistic particles created just after the end of inflation, when $H \sim H_{end} \sim 10^{13}$ GeV, are separated from their antiparticles by distances more than 4 orders of magnitude smaller than the average distance between these pairs. On the other hand, if the nonequilibrium processes of superheavy particle creation (such as decay of inflation) take place at the end of the preheating stage and the reheating temperature is as low as it is constrained from the effects of gravitino decays on ^{6}Li abundance ($T_r < 4\times 10^6$ GeV [10, 11]), the primordial separation of pairs given by Eq. (1) can exceed the value given by Eq. (2). This means that the separation between particles and antiparticles can be determined in this case by their averaged density, if they were created at

$$H \le H_s \sim 10^{-15} m_{Pl}\left(\frac{10^{14}\ \text{GeV}}{m}\right)^{2/3}\left(\frac{\Omega_X}{0.3}\right)^{2/3}$$

$$\sim 10^{4}\left(\frac{\Omega_X}{0.3}\right)^{2/3}\ \text{GeV}.$$

If the considered charge is the source of a long-range field similar to the electromagnetic field, which can bind a particle and antiparticle into an atomlike system analogous to positronium, it may have important practical implications for the UHECR problem. The annihilation timescale of such a bound system can provide a rate of UHE particle sources corresponding to UHECR data.

A pair of a particle and antiparticle with opposite gauge charges forms a bound system when, in the course of expansion, the absolute magnitude of the potential energy of the pair $V = \alpha_y/l$ exceeds the kinetic energy of the particle's relative motion $T_k = p^2/2m$. The mechanism is similar to that proposed in [12] for the binding of magnetic monopole–antimonopole pairs. It is not a recombination one. The binding of two oppositely charged particles is caused just by their Coulomb-like attraction, once it exceeds the kinetic energy of their relative motion.

In case plasma interactions do not heat superheavy particles created with relative momentum $p \le mc$ in the period corresponding to Hubble constant $H \ge H_s$, their initial separation, being on the order of

$$l(H) = \left(\frac{p}{mH}\right), \quad (3)$$

experiences only the effect of general expansion, proportional to the inverse first power of the scale factor, while the initial kinetic energy decreases as the square of the scale factor. Thus, the binding condition is fulfilled in the period corresponding to the Hubble constant H_c, determined by the equation

$$\left(\frac{H}{H_c}\right)^{1/2} = \frac{p^3}{2m^2\alpha_y H}, \quad (4)$$

where H is the Hubble constant in the period of particle creation and α_y is the "running constant" of the long range $U(1)$ interaction possessed by the superheavy particles. If the local process of pair creation does not involve nonzero orbital momentum, due to primordial pairing the bound system is formed in the state with zero orbital momentum. The size of the bound system strongly depends on the initial momentum distribution and for $p \le mc$ is equal to

$$l_c = \frac{p^4}{2\alpha_y m^3 H^2} = 2\frac{\alpha_y}{m\beta^2}, \quad (5)$$

where

$$\beta = \frac{2\alpha_y mH}{p^2}. \quad (6)$$

The annihilation timescale of this bound system can be estimated from the annihilation rate given by

$$w_{\rm ann} = |\Psi(0)|^2(\sigma v)_{\rm ann} \sim l_c^{-3}\frac{\alpha_y^2}{m^2}C_y, \quad (7)$$

where the "Coulomb" factor C_y arises similarly to the case of a pair of electrically charged particle and antiparticle. For the relative velocity $v/c \ll 1$, it is given by [13] $C_y = 2\pi\alpha_y c/v$. Finally, taking $v/c \sim \beta$, one obtains for the annihilation timescale

$$\tau_{\rm ann} \sim \frac{1}{8\pi\alpha_y^5}\left(\frac{p}{mc}\right)^{10}\left(\frac{m}{H}\right)^5\frac{1}{m} = \frac{4}{\pi m\beta^5}. \quad (8)$$

For $H_{end} \geq H \geq H_s$, the annihilation timescale is

$$\tau_{\rm ann} = 2\times 10^{19}\left(\frac{1}{50\alpha_y}\right)^5\left(\frac{p}{mc}\right)^{10} \times\left(\frac{10^4\ {\rm GeV}}{H}\right)^5\left(\frac{m}{10^{14}\ {\rm GeV}}\right)^4 {\rm s}, \quad (9)$$

where $p \sim mc$, $\alpha_y = 1/50$, and $m = 10^{14}$ GeV in the range from 10^{-26} s up to $2\times 10^{19}(0.3/\Omega_X)^{10/3}$ s. The size of the bound system is given by

$$l_c = 5\times 10^{-7}\left(\frac{p}{mc}\right)^4\frac{m}{10^{14}\ {\rm GeV}}\left(\frac{10^4\ {\rm GeV}}{H}\right)^2 {\rm cm}, \quad (10)$$

ranging for $2\times 10^{-10} \leq \Omega_X/0.3 \leq 1$ from 7×10^{-7} to 6×10^{-3} cm.

Provided that the primordial abundance of superheavy particles created at the preheating stage corresponds to the appropriate modern density $\Omega_X \leq 0.3$ and that the annihilation timescale exceeds the age of the Universe $t_U = 4\times 10^{17}$ s, owing to the strong dependence on the initial momentum p, the magnitude $r_X = \frac{\Omega_X}{0.3}\frac{t_U}{\tau_X}$ can reach the value $r_X = 2\times 10^{-10}$, which was found in [2] to fit the UHECR data on superheavy particle decay in the halo of our Galaxy.

For late particle production (i.e., at $H \leq H_s$), the binding condition can retain the form (4) if $l(H) \leq l_s$. In the opposite case, when $l(H) \geq l_s$, the primordial pairing is lost and even zero-orbital-momentum particles and antiparticles originating from different pairs form, in general, bound systems with nonzero orbital momentum. The size of the bound system is in this case obtained from the binding condition for the initial separation, determined by Eq. (2), and is equal to

$$l_c \approx \frac{10^{15}}{2\alpha_y m_{Pl}}\left(\frac{m}{10^{14}\ {\rm GeV}}\right)^{2/3}\left(\frac{0.3}{\Omega_X}\right)^{2/3}\left(\frac{p}{mc}\right)^2\left(\frac{m}{H}\right). \quad (11)$$

The lifetime of the bound system can be reasonably estimated in this case with the use of the well-known results of the classical problem of massive particles with opposite electric charges falling down the center due to radiation in the bound system. The corresponding timescale is given by (see [14] for details)

$$\tau = \frac{l_c^3}{64\pi}\frac{m^2}{\alpha_y^2}. \quad (12)$$

Using Eq. (11) and the condition $l(H) \geq l_s$, one obtains for this case the restriction

$$r_X = \frac{\Omega_X}{0.3}\frac{t_U}{\tau_X} \leq 3\times 10^{-10}\left(\frac{\Omega_X}{0.3}\right)^5\left(\frac{10^{14}\ {\rm GeV}}{m}\right)^9. \quad (13)$$

The gauge $U(1)$ nature of the charge possessed by superheavy particles assumes the existence of massless $U(1)$ gauge bosons (y photons) mediating this interaction. Since the considered superheavy particles are the lightest particles bearing this charge and they are not in thermodynamic equilibrium, one can expect that there should be no thermal background of y photons and that their nonequilibrium fluxes can not significantly heat the superheavy particles.

The situation changes drastically if the superheavy particles possess not only new $U(1)$ charge but also some ordinary (weak, strong, or electric) charge. Due to this charge, superheavy particles interact with the equilibrium relativistic plasma (with the number density $n \sim T^3$) and, for the mass of particles $m \leq \alpha^2 m_{Pl}$, the rate of heating $n\sigma v\Delta E \sim \alpha^2 T^3/m$ is sufficiently high to bring the particles into thermal equilibrium with this plasma. Here, α is the running constant of the considered (weak, strong, or electromagnetic) interaction.

Plasma heating causes the thermal motion of superheavy particles. At $T \leq m\left(\frac{m}{\alpha^2 m_{Pl}}\right)^2$, their mean free path relative to scattering with plasma exceeds the free thermal motion path, so it is not diffusion but free motion with thermal velocity v_T that leads to complete loss of initial pairing, since $v_T t$ formally exceeds l_s at

$$T \leq 10^{-10}m_{Pl}\left(\frac{\Omega_X}{0.3}\right)^{2/3}\left(\frac{10^{14}\ {\rm GeV}}{m}\right)^{5/3}.$$

While plasma heating keeps superheavy particles in thermal equilibrium, the binding condition $V \geq T_{\rm kin}$ cannot take place. At $T < T_N$ (where $N = e$, QCD, w, respectively, and $T_e \sim 100$ keV for electrically charged particles; $T_{\rm QCD} \sim 300$ MeV for colored particles and $T_w \approx 20$ GeV for weakly interacting particles; see [14] for details), the plasma heating is suppressed and superheavy particles go out of thermal equilibrium.

In the course of successive expansion, the binding condition is formally reached at T_c, given by

$$T_c = T_N\alpha_y 3\times 10^{-8}\left(\frac{\Omega_X}{0.3}\right)^{1/3}\left(\frac{10^{14}\ {\rm GeV}}{m}\right)^{1/3}. \quad (14)$$

However, for electrically charged particles, the binding does not in fact take place to the present time, since one gets from Eq. (14) $T_c \leq 1$ K. Bound systems of hadronic and weakly interacting superheavy particles can form, respectively, at $T_c \sim 0.3$ eV and $T_c \approx 20$ eV, but even for weakly interacting particles the size of such bound systems approaches half a meter (30 m for hadronic particles!). This leads to an extremely long annihilation timescale of these bound systems, which cannot fit UHECR data. This makes it impossible to realize the considered mechanism of UHECR origin if the superheavy $U(1)$ charged particles share ordinary weak, strong, or electromagnetic interactions.

Disruption of primordial bound systems in their collisions by tidal forces in the Galaxy reduces their concentration in the regions of enhanced density. Such spatial distribution, specific for these UHECR sources, makes it possible to distinguish them from other possible mechanisms [4, 9, 15] in the future AUGER and EUSO experiments.

The crucial physical condition for the formation of primordial bound systems of superheavy particles is the existence of new strictly conserved local $U(1)$ gauge symmetry, ascribed to the hidden sector of particle theory. Such symmetry can arise in the extended variants of GUT models (see, e.g., [10] for review), in heterotic string phenomenology (see [13] and references therein), and in D-brane phenomenology [16]. Note that in such models the strictly conserved $SU(2)$ symmetry can also arise in the hidden sector, which leads to a nontrivial mechanism of primordial binding of superheavy particles due to macroscopic size $SU(2)$ confinement, as was the case for "tetons" [17].

The proposed mechanism offers a link between the observed UHECRs and the predictions of particle theory, which cannot be tested by any other means and on which the analysis of primordial pairing and binding can put severe constraints. If viable, the considered mechanism makes UHECR a unique source of detailed information on the possible properties of the hidden sector of particle theory and on the physics of the very early Universe.

The work was partially performed in the framework of State Contract 40.022.1.1.1106 and supported in part by the Russian Foundation for Basic Research, grant nos. 02-02-17490 and UR.02.01.026. One of us (M.Yu.Kh.) expresses his gratitude to IHES and LUTH (Observatory Paris-Meudon) for hospitality, and both authors are grateful for support in their visit to College de France (Paris, April 2002). We are grateful to D. Fargion and S. Sarkar for useful comments.

REFERENCES

1. K. Greisen, Phys. Rev. Lett. **16**, 748 (1966); G. T. Zatsepin and V. A. Kuzmin, Pis'ma Zh. Éksp. Teor. Fiz. **4**, 114 (1966) [JETP Lett. **4**, 78 (1966)].
2. V. Berezinsky, M. Kachelriess, and A. Vilenkin, Phys. Rev. Lett. **79**, 4302 (1997).
3. V. A. Kuzmin and V. A. Rubakov, Yad. Fiz. **61**, 1122 (1998) [Phys. At. Nucl. **61**, 1028 (1998)].
4. D. Fargion, B. Mele, and A. Salis, astro-ph/9710029; Astrophys. J. **517**, 725 (1999); Preprint No. 1179/97, INFN (1997); T. J. Weiler, Astropart. Phys. **11**, 303 (1999).
5. H. Ziaeepour, Gravit. Cosmol. Suppl. **6**, 128 (2000).
6. D. Chung, E. W. Kolb, and A. Riotto, Phys. Rev. D **59**, 023501 (1999).
7. L. Kofman, A. D. Linde, and A. A. Starobinsky, Phys. Rev. D **56**, 3258 (1997).
8. J. Ellis, G. Gelmini, J. Lopes, *et al.*, Nucl. Phys. B **373**, 399 (1992); S. Sarkar, Nucl. Phys. A, Proc. Suppl. **28**, 405 (1992).
9. S. Sarkar and R. Toldra, Nucl. Phys. B **621**, 495 (2002).
10. M. Yu. Khlopov, *Cosmoparticle Physics* (World Sci., Singapore, 1999).
11. Yu. L. Levitan, E. V. Sedelnikov, I. M. Sobol, and M. Yu. Khlopov, Yad. Fiz. **57**, 1466 (1994) [Phys. At. Nucl. **57**, 1393 (1994)].
12. V. K. Dubrovich, Gravit. Cosmol. Suppl. **8**, 122 (2002).
13. M. Yu. Khlopov and K. I. Shibaev, Gravit. Cosmol. Suppl. **8**, 45 (2002).
14. V. K. Dubrovich, D. Fargion, and M. Yu. Khlopov, Astropart. Phys. (2003) (in press).
15. V. Berezinsky and A. A. Mikhailov, Phys. Lett. B **449**, 237 (1999).
16. G. Aldazabal, L. E. Ibanez, F. Quevedo, and A. M. Uranga, J. High Energy Phys. **0008**, 002 (2000); L. F. Alday and G. Aldazabal, J. High Energy Phys. **0205**, 022 (2002).
17. L. B. Okun', Pis'ma Zh. Éksp. Teor. Fiz. **31**, 156 (1980) [JETP Lett. **31**, 144 (1980)]; M. Yu. Khlopov, Yad. Fiz. **32**, 1600 (1980) [Sov. J. Nucl. Phys. **32**, 828 (1980)].

JETP Letters, Vol. 77, No. 7, 2003, pp. 339–343. From Pis'ma v Zhurnal Éksperimental'noĭ i Teoreticheskoĭ Fiziki, Vol. 77, No. 7, 2003, pp. 407–411.

Evolution of the Cosmological Constant in Effective Gravity¶

G. E. Volovik

Low-Temperature Laboratory, Helsinki University of Technology, FIN-02015 HUT, Finland
Landau Institute for Theoretical Physics, Russian Academy of Sciences, Moscow, 117334 Russia
e-mail: volovik@boojum.hut.fi

Received February 20, 2003; in final form, March 5, 2003

In contrast to the phenomenon of nullification of the cosmological constant in equilibrium vacuum, which is the general property of any quantum vacuum, there are many options in modifying the Einstein equation to allow the cosmological constant to evolve in a nonequilibrium vacuum. An attempt is made to extend the Einstein equation in the direction suggested by the condensed matter analogy of the quantum vacuum. Different scenarios are found depending on the behavior of and the relation between the relaxation parameters involved, some of these scenarios having been discussed in the literature. One of them reproduces the scenario in which the effective cosmological constant emerges as a constant of integration. The second one describes the situation when, after the cosmological phase transition, the cosmological constant drops from zero to a negative value; this scenario describes the relaxation from this big negative value back to zero and then to a small positive value. In the third example, the relaxation time is not a constant but depends on matter; this scenario demonstrates that vacuum energy (or its fraction) can play the role of cold dark matter. © *2003 MAIK "Nauka/Interperiodica"*.

PACS numbers: 04.20.Cv; 98.80.Es

1. INTRODUCTION

It is clear that the pressure of the vacuum in our Universe is very close to zero as compared to the Planck energy scale, and thus the experimental cosmological constant is close to zero. However, if at this almost zero pressure one starts calculating the vacuum energy by summing all the positive and negative energy states, one obtains a huge vacuum energy that by about 120 orders of magnitude exceeds the experimental limit. This is the main cosmological constant problem [1–4].

Exactly the same "paradox" occurs in any quantum liquid (or in any other condensed matter) at zero pressure. The experimental energy of the ground state of, say, the quantum liquid at zero pressure is zero. On the other hand, if one starts calculating the vacuum energy by summing the energies of all the positive and negative energy modes up to the corresponding Planck (Debye) scale, one obtains a huge energy. However, there is no real paradox in quantum liquids, since if one adds all the trans-Planckian (microscopic, atomic) modes one immediately obtains the zero value, irrespective of the details of the microscopic physics [5]. The fully microscopic consideration restores the Gibbs–Duhem relation $\epsilon = -p$ between the energy (the relevant thermodynamic potential) and the pressure of the quantum liquid at $T = 0$, which ensures that the energy of the vacuum state $\epsilon = 0$ if the external pressure is zero.

This is the first message from condensed matter to the physics of the quantum vacuum: One should not worry about the huge vacuum energy, the trans-Planckian physics with its degrees of freedom will do the job of the cancellation of the vacuum energy without any fine tuning and irrespective of the details of the trans-Planckian physics. There are other messages that are also rather general and do not depend much on the details of trans-Planckian physics. For example, if the cosmological constant is zero above the cosmological phase transition, it will become zero below the transition after some transient period.

Thus, from the quantum-liquid analogue of the quantum vacuum, it follows that the cosmological constant is not a constant but is an evolving physical parameter, and our goal is to find the laws of its evolution. In contrast to the phenomenon of the cancellation of the cosmological constant in the equilibrium vacuum, which is the general property of any quantum vacuum, there are many options in modifying the Einstein equation to allow the cosmological constant to evolve. However, condensed matter physics teaches us that we must avoid the discussion of the microscopic models of the quantum vacuum [6] and use instead the general phenomenological approach. That is why we do not follow the traditional way of description in terms of, say, the scalar field, which mediates the decay of the dark energy [7], and instead present an attempt at a purely phenomenological description by introducing dissipative terms directly into the Einstein equation.

¶This article was submitted by the author in English.

2. EINSTEIN EQUATION

Standard formulation. Let us start with the nondissipative equation for gravity—the Einstein equation. It is obtained from the action

$$S = S_E + S_\Lambda + S_M, \quad (1)$$

where S_M is the matter action;

$$S_E = -\frac{1}{16\pi G}\int d^4x\sqrt{-g}\mathcal{R} \quad (2)$$

is the Einstein curvature action; and

$$S_\Lambda = -\frac{\Lambda}{8\pi G}\int d^4x\sqrt{-g}, \quad (3)$$

where Λ is the cosmological constant [8]. Variation over the metric $g^{\mu\nu}$ gives

$$\frac{1}{8\pi G}(G_{\mu\nu} - \Lambda g_{\mu\nu}) = T^M_{\mu\nu}, \quad (4)$$

where

$$G_{\mu\nu} = R_{\mu\nu} - \frac{1}{2}\mathcal{R}g_{\mu\nu} \quad (5)$$

is the Einstein tensor and $T^M_{\mu\nu}$ is the energy–momentum tensor for matter. This form of the Einstein equation implies that the matter fields on the right-hand side of Eq. (4) serve as the source of the gravitational field, while the Λ term belongs to the gravity.

Moving the Λ-term to the right-hand side of the Einstein equation changes the meaning of the cosmological constant. The Λ-term becomes the energy–momentum tensor of the vacuum, which in addition to the matter is the source of the gravitational field [9]:

$$\frac{1}{8\pi G}G_{\mu\nu} = T^M_{\mu\nu} + T^\Lambda_{\mu\nu}, \quad T^\Lambda_{\mu\nu} = \rho_\Lambda g_{\mu\nu} = \frac{\Lambda}{8\pi G}g_{\mu\nu}. \quad (6)$$

Here, ρ_Λ is the vacuum energy density and $p_\Lambda = -\rho_\Lambda$ is the vacuum pressure.

Einstein equation in induced gravity. In the induced gravity introduced by Sakharov [10], the gravity is the elasticity of the vacuum, say, fermionic vacuum, and the action for the gravitational field is induced by the vacuum fluctuations of the fermionic matter fields. This kind of effective gravity, emerges in quantum liquids [5]. In the induced gravity, the Einstein tensor must also be moved to the matter side, i.e., to the right-hand side:

$$0 = T^M_{\mu\nu} + T^\Lambda_{\mu\nu} + T^{curv}_{\mu\nu}, \quad (7)$$

where

$$T^{curv}_{\mu\nu} = -\frac{1}{8\pi G}G_{\mu\nu} \quad (8)$$

has the meaning of the energy–momentum tensor produced by deformations of the fermionic vacuum. It describes such elastic deformations of the vacuum, which distort the effective metric field $g_{\mu\nu}$ and thus play the role of the gravitational field. As distinct from the $T^\Lambda_{\mu\nu}$ term, which is of the zeroth order in gradients of the metric, the $T^{curv}_{\mu\nu}$ term is of the second order in gradients of $g_{\mu\nu}$. The higher order gradient terms also naturally appear in induced gravity.

In the induced gravity, the free gravitational field is absent, since there is no gravity in the absence of the quantum vacuum. Thus, the total energy–momentum tensor comes from the original (bare) fermionic degrees of freedom. That is why all the contributions to the energy–momentum tensor are obtained by the variation of the total fermionic action over $g^{\mu\nu}$:

$$T^{total}_{\mu\nu} = \frac{2}{\sqrt{-g}}\frac{\delta S}{\delta g^{\mu\nu}} = -\frac{1}{8\pi G}G_{\mu\nu} + \rho_\Lambda g_{\mu\nu} + T^M_{\mu\nu}. \quad (9)$$

According to the variational principle, $\delta S/\delta g^{\mu\nu} = 0$, the total energy–momentum tensor is zero, which gives rise to the Einstein equation in the form of Eq. (7). Since $T^{total}_{\mu\nu} = 0$, it satisfies the conventional and covariant conservation laws, $T^{total\ \nu}_{\mu,\ \nu} = 0$ and $T^{total\ \nu}_{\mu;\ \nu} = 0$, and thus serves as the covariant and localized energy–momentum tensor of matter and gravity.

In this respect, there is not much difference between different contributions to the energy–momentum tensor: all come from the original fermions. However, in the low-energy corner, where the gradient expansion for the effective action works, one can distinguish between different contributions: (i) some part of the energy–momentum tensor ($T^M_{\mu\nu}$) comes from the excited fermions—quasiparticles—which in the effective theory form the matter. The other parts come from the fermions forming the vacuum—the Dirac sea. The contribution from the vacuum fermions contains (ii) the zeroth-order term in the gradients of $g_{\mu\nu}$; this is the energy–momentum tensor of the homogeneous vacuum—the Λ term. Of course, the whole Dirac sea cannot be sensitive to the change of the effective infrared fields $g_{\mu\nu}$: only small infrared perturbations of the vacuum, which we are interested in, are described by these effective fields; (iii) the stress tensor of the inhomogeneous distortion of the vacuum state, which plays the role of gravity; the second-order term $T^{curv}_{\mu\nu}$ in the stress tensor represents the curvature term in the Einstein equation.

The same occurs in induced QED [11], where the electromagnetic field is induced by the vacuum fluctuations of the same fermionic field. The total electric current

$$j^\mu = \frac{\delta S}{\delta A_\mu} = \frac{\delta S^{int}}{\delta A_\mu} + \frac{\delta S^{Maxwell}}{\delta A_\mu} = j^\mu_{\text{charged particles}} + j^\mu_{\text{field}}, \quad (10)$$

is produced by excited fermions (the first term) and by fermions in the quantum vacuum (the second term). The electric current in the second term is produced by such elastic deformations of the fermionic vacuum that play the role of the electromagnetic field, and the lowest order term in the effective action describing such distortion of the vacuum state is the induced Maxwell action

$$S^{\rm Maxwell} = \int dt d^3x \frac{\sqrt{-g}}{16\pi\alpha} F^{\mu\nu} F_{\mu\nu}, \qquad (11)$$

which is of the second order in gradients of A_μ. According to the variational principle, $\delta S/\delta A_\mu = 0$, the total electric current produced by the vacuum and excited fermions is zero. This means that the system is always locally electroneutral. This ensures that the homogeneous vacuum state without excitations has zero electric charge, i.e., our quantum vacuum is electrically neutral. The same occurs with the hypercharge, weak charge, and color charge of the vacuum: they are zero in the absence of matter and fields.

In the traditional approach, the cosmological constant is fixed, and it serves as the source for the metric field: in other words, the input in the Einstein equation is the cosmological constant, the output is de Sitter expansion, if matter is absent. In effective gravity, where the gravitational field, the matter fields, and the cosmological "constant" emerge simultaneously in the low-energy corner, one cannot say that one of these fields, is primary and serves as a source for the other fields, thus governing their behavior. The cosmological constant, as one of the players, adjusts to the evolving matter and gravity in a self-regulating way. In particular, in the absence of matter ($T^{\rm M}_{\mu\nu} = 0$), the nondistorted vacuum ($T^{\rm curv}_{\mu\nu} = 0$) acquires zero cosmological constant, since, according to the "gravi-neutrality" condition Eq. (7), it follows from equations $T^{\rm M}_{\mu\nu} = 0$ and $T^{\rm curv}_{\mu\nu} = 0$ that $T^{\Lambda}_{\mu\nu} = 0$. In this approach, the input is the vacuum configuration (in the given example, there is no matter and the vacuum is homogeneous), the output is the vacuum energy. In contrast to the traditional approach, here the gravitational field and matter serve as a source of the induced cosmological constant.

This conclusion is supported by the effective gravity and effective QED, which emerge in quantum liquids or any other condensed matter system of the special universality class [5]. The nullification of the vacuum energy in the equilibrium homogeneous vacuum state of the system also follows from the variational principle, or more generally from the Gibbs–Duhem relation applied to the equilibrium vacuum state of the fermionic system if it is isolated from the environment. In the absence of the environment, one has $p_\Lambda = 0$, while from the Gibbs–Duhem relation $\rho_\Lambda = -p_\Lambda$ at $T = 0$ it follows that $\rho_\Lambda = 0$. This corresponds to $T^{\Lambda}_{\mu\nu} = 0$ for a quiescent flat Universe at $T = 0$; i.e., a quiescent flat Universe without matter is not gravitating.

3. MODIFICATION OF EINSTEIN EQUATION AND RELAXATION OF THE VACUUM ENERGY

Dissipation in Einstein equation. The Einstein equation does not allow us to obtain the time dependence of the cosmological constant, because of the Bianchi identities $G^{\nu}_{\mu;\,\nu} = 0$ and covariant conservation law for matter fields (quasiparticles) $T^{\nu{\rm M}}_{\mu;\,\nu} = 0$, which together lead to $\partial_\mu \Lambda = 0$. But they allow us to obtain the value of the cosmological constant in different static Universes, such as the Einstein closed Universe [8], where the cosmological constant is obtained as a function of the curvature and matter density. To describe the evolution of the cosmological constant, the relaxation term must be added.

The dissipative term in the Einstein equation can be introduced in the same way as in two-fluid hydrodynamics [12], which serves as the nonrelativistic analogue of the self-consistent treatment of the dynamics of the vacuum (the superfluid component of the liquid) and matter (the normal component of the liquid) [5]:

$$T^{\rm M}_{\mu\nu} + T^{\Lambda}_{\mu\nu} + T^{\rm curv}_{\mu\nu} + T^{\rm diss}_{\mu\nu} = 0, \qquad (12)$$

where $T^{\rm diss}_{\mu\nu}$ is the dissipative part of the total energy–momentum tensor. In contrast to the conventional dissipation of the matter, such as viscosity and thermal conductivity of the cosmic fluid, this term is not a part of $T^{\rm M}_{\mu\nu}$. It describes the dissipative back reaction of the vacuum, which does not influence the matter conservation law $T^{\nu{\rm M}}_{\mu;\,\nu}$. The condensed-matter example of such a relaxation of the variables describing the fermionic vacuum is provided by the dynamic equation for the order parameter in superconductors—the time-dependent Ginzburg–Landau equation, which contains the relaxation term (see, e.g., the book [13]).

Let us consider how the relaxation occurs by the example of the spatially flat Robertson–Walker metric

$$ds^2 = dt^2 - a^2(t) d\mathbf{r}^2. \qquad (13)$$

The Ricci tensor and scalar and the Einstein tensor are

$$R^0_0 = -3\frac{\partial_t^2 a}{a}; \quad R^i_j = -\delta^i_j \left(\frac{\partial_t^2 a}{a} + 2\frac{(\partial_t a)^2}{a^2} \right), \qquad (14)$$

$$\mathcal{R} = -6\left(\frac{\partial_t^2 a}{a} + \frac{(\partial_t a)^2}{a^2} \right), \qquad (15)$$

$$G^0_0 = R^0_0 - \frac{1}{2}\mathcal{R} = 3\frac{(\partial_t a)^2}{a^2} \equiv 3H^2, \qquad (16)$$

$$G^j_i = R^j_i - \frac{1}{2}\mathcal{R}\delta^j_i = \delta^j_i\left(H^2 + 2\frac{\partial_t^2 a}{a}\right) = \delta^j_i(3H^2 + 2\dot{H}). \quad (17)$$

In the lowest order of the gradient expansion, the dissipative part $T^{\rm diss}_{\mu\nu}$ of the stress tensor describing the relaxation of Λ must be proportional to the first time derivative.

Cosmological constant as integration constant. Let us start with the following guess:

$$T^{\rm diss}_{\mu\nu} = \tau_\Lambda \frac{\partial \rho_\Lambda}{\partial t} g_{\mu\nu}. \quad (18)$$

This noncovariant term implies the existence of a preferred reference frame, which is a natural ingredient of the trans-Planckian physics, where general covariance is violated. The modified Einstein equations in the absence of matter are correspondingly

$$3H^2 = \Lambda + \tau_\Lambda \dot{\Lambda}, \quad (19)$$

$$3H^2 + 2\dot{H} = \Lambda + \tau_\Lambda \dot{\Lambda}. \quad (20)$$

This gives the constant Hubble parameter H = const, i.e., the exponential de Sitter expansion or contraction. The cosmological "constant" Λ relaxes to the value determined by the expansion rate:

$$\Lambda(t) = 3H^2 + (\Lambda(0) - 3H^2)\exp\left(-\frac{t}{\tau_\Lambda}\right). \quad (21)$$

This is consistent with the Bianchi identity, which requires that $\partial_t(\Lambda + \tau_\Lambda \dot{\Lambda}) = 0$. Actually, this situation corresponds to the well-known case when the cosmological constant arises as an integration constant (see reviews [1, 4]). Here it is the integration constant $\Lambda_0 = \Lambda + \tau_\Lambda \partial_t \Lambda$. Such a scenario emerges because the dissipative term in Eq. (18) is proportional to $g_{\mu\nu}$.

Model with two relaxation parameters. Since $T^{\rm diss}_{\mu\nu}$ is a tensor, the general description of the vacuum relaxation requires introduction of several relaxation times. This also violates the Lorentz invariance, but we have already assumed that the dissipation of the vacuum variables due to trans-Planckian physics implies the existence of the preferred reference frame. In isotropic space, we have only two relaxation times: in the energy and pressure sectors. In the presence of matter, one has

$$3H^2 = \Lambda + \tau_1 \dot{\Lambda} + 8\pi G \rho^{\rm M}, \quad (22)$$

$$3H^2 + 2\dot{H} = \Lambda + \tau_2 \dot{\Lambda} - 8\pi G p^{\rm M}. \quad (23)$$

Since the covariant conservation law for matter does not follow now from the Bianchi identities, these two equations must be supplemented by the covariant conservation law to prevent the creation of matter:

$$a\frac{\partial}{\partial a}(\rho^{\rm M} a^3) = p^{\rm M} a^3. \quad (24)$$

Let us consider the simplest case, when the relaxation occurs only in the pressure sector, i.e., $\tau_1 = 0$. We assume also that the ordinary matter is cold, i.e., its pressure $p^{\rm M} = 0$, which gives $\rho^{\rm M} \propto a^{-3}$. Then one finds two classes of solutions: (i) Λ = const and (ii) $H = 1/3\tau_2$. The first one corresponds to the conventional expansion with constant Λ term and cold matter, so let us discuss the second solution, $H = 1/3\tau_2$.

Relaxation after cosmological phase transition. In the simplest case, when $\tau_2 \equiv \tau$ = const, the Λ term and the energy density of matter $\rho^{\rm M}$ exponentially relax to $1/3\tau^2$ and to 0, respectively:

$$H = \frac{1}{3\tau}, \quad \Lambda(t) = \frac{1}{3\tau^2} - 8\pi G \rho^{\rm M}(t), \quad \frac{\rho^{\rm M}(t)}{\rho^{\rm M}(0)} = \exp\left(-\frac{t}{\tau}\right). \quad (25)$$

Such a solution describes the behavior after the cosmological phase transition. According to the condensed-matter example of the phase transition, the cosmological "constant" is (almost) zero before the transition, while after the transition it drops to a negative value and then relaxes back to zero [5]. Equation (25) corresponds to the latter stage, but it demonstrates that, in its relaxation after the phase transition, Λ crosses zero and finally becomes a small positive constant determined by the relaxation parameter τ, which governs the exponential de Sitter expansion.

Dark energy as dark matter. Let us now allow τ to vary. Usually the relaxation and dissipation are determined by matter (quasiparticles). The term that violates the Lorentz symmetry or the general covariance must contain the Planck scale $E_{\rm Planck}$, since it must disappear at infinite Planck energy. The lowest order term, which contains the $E_{\rm Planck}$ in the denominator, is $\hbar/\tau \sim T^2/E_{\rm Planck}$, where T is the characteristic temperature or energy of matter. In the case of radiation, it can be written in terms of the radiation density:

$$\frac{1}{3\tau^2} = 8\pi\alpha G \rho^{\rm M}, \quad (26)$$

where α is a dimensionless parameter. If Eq. (26) can be applied to the cold baryonic matter too, then the solution of class (ii) becomes again $H = 1/3\tau$, but now τ depends on the matter field. This solution gives the standard power law for the expansion of the cold flat

Universe and the relation between Λ and the baryonic matter density ρ^M:

$$a \propto t^{2/3}, \quad 8\pi G\rho^M = \frac{4}{3\alpha t^2}, \qquad H = \frac{2}{3t}, \quad \Lambda = (\alpha - 1)8\pi G\rho^M. \tag{27}$$

In terms of the densities normalized to $\rho_c = 3H^2/8\pi G$ (the critical density corresponding to the flat Universe in the absence of the vacuum energy), $\Omega_\Lambda = \rho_\Lambda/\rho_c$ and $\Omega^M = \rho^M/\rho_c$ one has

$$\Omega^M = \frac{1}{\alpha}, \quad \Omega_\Lambda = \frac{\alpha - 1}{\alpha}. \tag{28}$$

Since the effective vacuum pressure in Eq. (23) is $p_\Lambda \propto -(\Lambda + \tau\dot{\Lambda}) = 0$, in this solution the dark energy behaves as cold dark matter. Thus, the vacuum energy can serve as the origin of the nonbaryonic dark matter.

4. CONCLUSIONS

In the effective gravity, the equilibrium time-independent vacuum state without matter is nongravitating; i.e., its relevant vacuum energy, which is responsible for gravity, is zero. In a nonequilibrium situation, the cosmological constant is nonzero, but it is an evolving parameter rather than a constant. The process of relaxation of the cosmological constant, when the vacuum is disturbed and out of equilibrium, requires some modification of the Einstein equation violating the Bianchi identities to allow the cosmological constant to vary. In contrast to the phenomenon of nullification of the cosmological constant in the equilibrium vacuum, which is the general property of any quantum vacuum and does not depend on its structure or on the details of the trans-Planckian physics, the deviations from general relativity can occur in many different ways, since there are many routes from the low-energy effective theory to the high-energy "microscopic" theory of the quantum vacuum. However, it seems reasonable that such modification can be written in the general phenomenological way, as, for example, the dissipative terms are introduced in the hydrodynamic theory. Here we suggested to describe the evolution of the Λ term by two phenomenological parameters (or functions)—the relaxation times. The corresponding dissipative terms in the stress tensor of the quantum vacuum are determined by trans-Planckian physics and do not obey the general covariance.

We discussed here the simplest examples of the relaxation of the vacuum to equilibrium, described by a single relaxation parameter. The first example ($\tau_1 = \tau_2$) reproduces the well-known scenario in which the effective cosmological constant emerges as a constant of integration. The second example ($\tau_1 = 0$ and $\tau_2 = \text{const}$) describes the situation that occurs if, after the cosmological phase transition, Λ acquires a large negative value: Λ relaxes back to zero and then to a small positive value. The third example, when τ_2 is determined by the baryonic matter density, demonstrates that the vacuum energy (or its fraction) can play the role of cold dark matter.

These examples are too simple to describe the real evolution of the present Universe and are actually excluded by observations [2]. A general consideration with two relaxation functions is needed. In this general case, it corresponds to the varying in time of the parameter $w_Q = p_Q/\rho_Q$ describing the equation of state of the quintessence with $w_Q(t) = -(\Lambda + \tau_2\dot{\Lambda})/(\Lambda + \tau_1\dot{\Lambda})$. The recent observational bounds on w_Q can be found, for example, in [14].

I thank A. Achúcarro, T.W.B. Kibble, I.I. Kogan, L.B. Okun, A.K. Rajantie, and A.A. Starobinsky for fruitful discussions. This work was supported by ESF COSLAB Programme and by the Russian Foundation for Basic Research.

REFERENCES

1. S. Weinberg, Rev. Mod. Phys. **61**, 1 (1989).
2. V. Sahni and A. Starobinsky, Int. J. Mod. Phys. D **9**, 373 (2000).
3. P. J. E. Peebles and B. Ratra, astro-ph/0207347.
4. T. Padmanabhan, hep-th/0212290.
5. G. E. Volovik, *The Universe in a Helium Droplet* (Clarendon Press, Oxford, 2003).
6. R. B. Laughlin, gr-qc/0302028.
7. U. Alam, V. Sahni, and A. A. Starobinsky, astro-ph/0302302.
8. A. Einstein, Sitzungsber. K. Preuss. Akad. Wiss. **1**, 142 (1917).
9. M. Bronstein, Phys. Z. Sowjetunion **3**, 73 (1933).
10. A. D. Sakharov, Dokl. Akad. Nauk SSSR **177**, 70 (1968) [Sov. Phys. Dokl. **12**, 1040 (1968)].
11. Ya. B. Zel'dovich, Pis'ma Zh. Éksp. Teor. Fiz. **6**, 922 (1967) [JETP Lett. **6**, 345 (1967)].
12. I. M. Khalatnikov, *An Introduction to the Theory of Superfluidity* (Nauka, Moscow, 1965; Benjamin, New York, 1965).
13. N. B. Kopnin, *Theory of Nonequilibrium Superconductivity* (Clarendon Press, Oxford, 2001).
14. D. Pogosyan, J. R. Bond, and C. R. Contaldi, astro-ph/0301310.

JETP Letters, Vol. 77, No. 7, 2003, pp. 344–348. Translated from Pis'ma v Zhurnal Éksperimental'noĭ i Teoreticheskoĭ Fiziki, Vol. 77, No. 7, 2003, pp. 412–416.

Spectroscopy of the ^{5}H Superheavy Hydrogen Isotope

M. G. Gornov[1, †], M. N. Ber[1], Yu. B. Gurov[1, *], S. V. Lapushkin[1], P. V. Morokhov[1], V. A. Pechkurov[1], N. O. Poroshin[1], V. G. Sandukovsky[2], M. V. Tel'kushev[1], and B. A. Chernyshev[1]

[1] *Moscow Engineering Physics Institute, Kashirskoe sh. 31, Moscow, 115409 Russia*
** e-mail: Gurov@axpk40.mephi.ru*
[2] *Joint Institute for Nuclear Research, Dubna, Moscow region, 141980 Russia*
Received June 24, 2002; in final form, February 12, 2003

The formation of the ^{5}H superheavy hydrogen isotope was experimentally sought in the reactions induced by stopped π^- mesons absorbed by ^{9}Be nuclei. Peaks in missing-mass spectra were observed in two reaction channels, ^{9}Be(π^-, *pt*)X and ^{9}Be(π^-, *dd*)X, and were attributed to the ^{5}H resonance states. The lowest state has parameters $E_r = 5.5 \pm 0.2$ MeV and $\Gamma = 5.4 \pm 0.5$ MeV [E_r is the resonance energy measured from the (triton + two neutrons) threshold]. Therefore, ^{5}H is bound more weakly than ^{4}H. Excited states of ^{5}H were also observed. All three resonance levels ($E_{1r} = 10.6 \pm 0.3$ MeV, $\Gamma_{1r} = 6.8 \pm 0.5$ MeV; $E_{2r} = 18.5 \pm 0.4$ MeV, $\Gamma_{2r} = 4.8 \pm 1.3$ MeV; $E_{3r} = 26.7 \pm 0.4$ MeV, $\Gamma_{3r} = 3.6 \pm 1.3$ MeV) can decay into five free nucleons. © *2003 MAIK "Nauka/Interperiodica"*.

PACS numbers: 21.10.-k; 25.80.Hp

Nuclei near the nucleon stability boundary are of interest due both to their unique properties, among which the neutron halo is most brilliant [1], and to the importance of the precise determination of their parameters for testing and developing nuclear models. Superheavy hydrogen isotopes are lightest neutron-rich resonances and, therefore, allow the simplest description by theoretical models. At the same time, only superheavy hydrogen isotopes among all nuclei at the nucleon stability boundary have the unfilled proton 1*s* shell. Thus, the data concerning these nuclei can provide the possibility of a critical test of the models based on the helium and lithium spectroscopy.

The question of the existence of the ^{5}H isotope was open for a long time. Enhancement in the proton spectrum near the kinematic threshold of the ^{6}Li(π^-, *p*)X reaction was observed in [2]. However, the interpretation of experimental data was uncertain; this enhancement was possibly caused by a substantial contribution from the three-body reaction channels.

An indication of the formation of ^{5}H in the ^{9}Be(π^-, *pt*)^{5}H reaction induced by stopped pions was obtained in our previous work [3]. Attributing enhancement in the missing-mass spectrum to one state, we obtained the resonance parameters $E_r = 7.4 \pm 0.7$ MeV and $\Gamma = 8 \pm 3$ MeV [E_r is the resonance energy measured from the (triton + two neutrons) threshold]. More recently, we observed indications of the formation of ^{5}H in the inclusive spectra of protons and deuterons in the reactions ^{6}Li(π^-, *p*)X ($E_r = 11.8 \pm 0.7$ MeV, $\Gamma = 5.6 \pm 0.9$ MeV) and ^{7}Li(π^-, *d*)X ($E_r = 9.1 \pm 0.7$ MeV, $\Gamma = 7.4 \pm 0.6$ MeV), respectively [4]. Experimental results [3, 4] are close to each other, but the data obtained on the lithium isotopes were based on a smaller statistical sample.

For a long time, the formation of ^{5}H on heavy-ion beams was observed only in the ^{7}Li(^{6}Li, ^{8}B)^{5}H reaction, where the resonance state with $E_r \approx 5.2$ MeV and $\Gamma \approx 4$ MeV was identified [5]. A narrow ^{5}H state with energy $E_r = 1.7 \pm 0.3$ MeV and width $\Gamma = 1.9 \pm 0.4$ MeV was recently observed in the ^{1}H(^{6}He, *pp*)X reaction [6].

Thus, the experimental spectroscopy of ^{5}H remains uncertain. The parameters of the observed states differ from each other by more than the measurement errors presented above. These discrepancies are possibly caused by noticeable selectivity of the population of ^{5}H levels. In any case, new experimental data are necessary.

Theoretical calculations also strongly differ from each other [7–9]. All models predict the nucleon instability of ^{5}H, but the resonance energy of the ground state calculated in [7] (≈6 MeV) is significantly higher than the values of 2.5–3 MeV obtained in [8, 9]. In addition, the authors of [8] predicted the existence of ^{5}H excited states with resonance energies ≈4.5–7.5 MeV.

In this paper, we present the spectroscopic results obtained for ^{5}H in a joint experiment carried out at the Moscow Engineering Physics Institute and Northwestern University (Evanston, Illinois). In this experiment,

† Deceased.

the formation of neutron-rich isotopes was investigated in reactions induced by stopped pions absorbed by 1*p*-shell nuclei. A ^{9}Be target was again used to seek for ^{5}H, because results could be obtained with a significantly larger statistical sample and with the noticeably better energy resolution. Moreover, ^{9}Be is preferable over lithium targets, because the ratio between the yields of the ^{5}H-formation, channels and the physical background in the correlation data is higher than in the inclusive data [3, 4].

Experiment was carried out on the low-energy pion channel (LEP) at the Los Alamos Meson Physics Facility with a multilayer semiconductor spectrometer made at the Moscow Engineering Physics Institute [10]. A beam of 30-MeV pions passed through a beryllium moderator and stopped in a thin target with a thickness of 24 mg/cm^2. The ^{9}Be target included less than 1% of uncontrolled impurities. The rate of pion stops was equal to 6×10^4 s^{-1}. Charged particles formed after the absorption of pions by nuclei were detected by two telescopes set at an angle of 180° to each other. Each telescope consisted of silicon detectors. Two surface-barrier detectors with thicknesses 100 and 400 μm were placed at the beginning of a telescope, and 3-mm-thick lithium drift detectors followed them. The area of a sensitive region of each detector was equal to 8 cm^2. The total thickness of each telescope was equal to 43 mm, which was sufficient for all long-range nuclear particles formed in the absorption reaction to be completely decelerated in the sensitive volume of a telescope.

To calibrate the detectors in energy, a radioactive source of α particles and a precise-amplitude generator were used. For absolute scale calibration, two-body reactions with pion absorption and known final nuclear states were taken. The systematic error did not exceed 100 keV. The energy resolution of the spectrometer for the detection of single-charged ions (*p*, *d*, *t*) was better than 0.5 MeV.

In this work, ^{5}H states were sought in the missing-mass spectra obtained from correlation data. In this case, the energy resolution was determined from measurements made on a ^{11}B target in the same experimental run. When two single-charged ions are detected in three-body channels of the absorption reaction on this nucleus, $^{5-9}$He isotopes are formed. The ground states of these isotopes are reliably determined and well separated from excited levels [11, 12]. Data analysis, whose results were partially reported in [13, 14], indicated that the missing-mass resolution is ≤1.0 MeV, and the error in the absolute scale calibration does not exceed 0.1 MeV.

In the experiment with the ^{9}Be target, the energy resolution and calibration, as well as the possible time variation of these quantities, were checked by correlation measurements of *tt* events. Figure 1 shows the missing-mass spectrum obtained in these measurements. The triton mass is the reference point. A peak

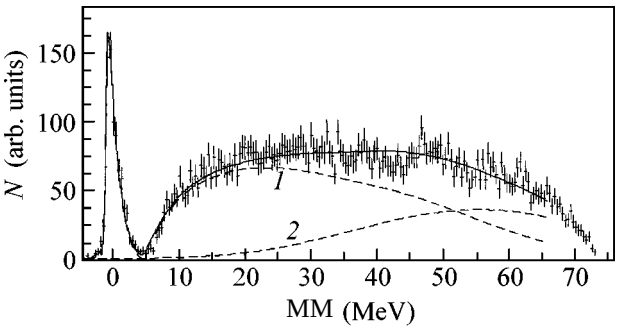

Fig. 1. Missing-mass spectrum for the ^{9}Be(π^-, *tt*)X reaction. The solid line is the complete description; lines *1* and *2* are the phase-space distributions for the ^{9}Be(π^-, *tt*)*dn* and ^{9}Be(π^-, *tt*)*p*2*n* reactions, respectively.

observed near the zero missing masses is assigned to the ^{9}Be(π^-, *tt*)*t* three-body reaction channel. The peak position ($E_{MM} = 0.0 \pm 0.1$ MeV) and its width ($\Delta \cong 1.2 \pm 0.1$ MeV) are consistent with the results obtained with ^{11}B. The peak is slightly broadened, because the angular acceptance of the spectrometer causes an increase in the width of a device line with decreasing mass of undetected reminder. The absence of time variations in the spectrometer characteristics was corroborated by the constant spectrum shape for different parts of the accumulated statistical sample.

The spectrometer and experimental procedure were described in more detail in [10].

Figures 2 and 3 show the missing-mass spectra for the ^{9}Be(π^-, *pt*)X and ^{9}Be(π^-, *dd*)X reactions, respectively. Missing masses are measured from the sum of masses of a triton and two neutrons. First, we note that there are no manifestations of ^{5}H bound states in the negative missing-mass region. The weak background in this region is caused by random coincidences in correlation measurements. At the same time, the structures, which can be attributed to the formation of resonance states, are observed in the positive missing-mass region in both spectra. To separate these ^{5}H states and to determine their parameters, we used the least-squares approximation in the description of measured spectra by the sum of *n*-body phase-space distributions ($n \geq 4$) and Breit–Wigner distributions. The angular and energy broadenings of the spectrometer, and the background of random coincidences, were also taken into account in the calculations.

The missing-mass spectra for the ^{9}Be(π^-, *pt*)X and ^{9}Be(π^-, *dd*)X reactions shown in Figs. 2a and 3a, respectively, are satisfactorily approximated (χ^2 per degree of freedom is equal to 1.05 and 0.94, respectively) by four ^{5}H resonance states and the sum of *n*-body phase-space distributions ($4 \leq n \leq 6$). The resonance parameters of the ^{5}H isotope that were obtained by fitting two spectra, together with their weighted

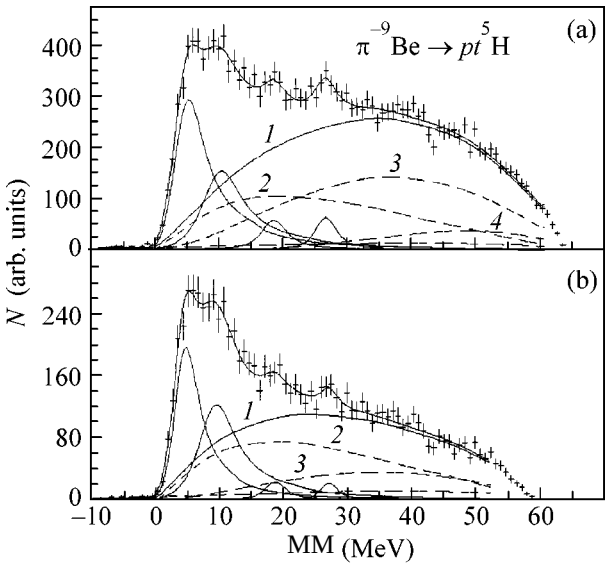

Fig. 2. Missing-mass spectra for the ^{9}Be(π^-, *pt*)X reaction: (a) measured spectrum and (b) spectrum measured under the restriction $Px \le 100$ MeV/c on the momentum of undetected residual. The solid lines are the total description and Breit–Wigner distributions, the numbered lines are the phase-space distributions for (*1*) all reaction channels, (*2*) ^{9}Be(π^-, *pt*)^{4}H*n*, (*3*) ^{9}Be(π^-, *pt*)*t*2*n*, and (*4*) ^{9}Be(π^-, *pt*)*d*3*n* channels.

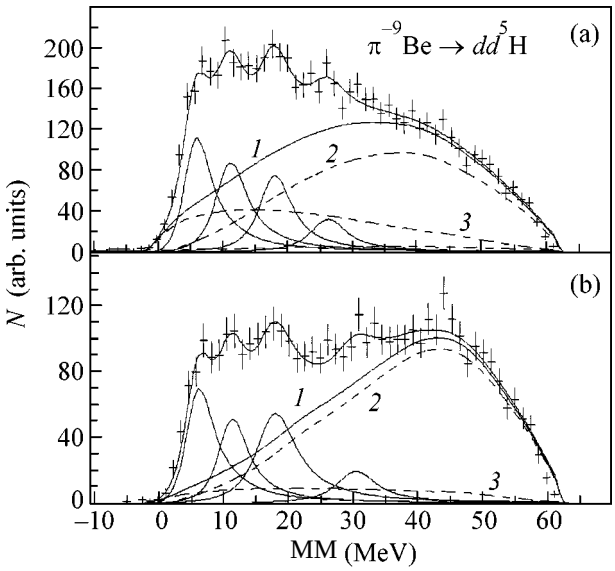

Fig. 3. Missing-mass spectrum for the ^{9}Be(π^-, *dd*)X reaction: (a) measured spectrum and (b) spectrum measured under the restriction $Px \le 100$ MeV/c on the momentum of undetected reminder. The solid lines are the total description and Breit–Wigner distributions, the numbered lines are the phase-space distributions for (*1*) all reaction channels, (*2*) ^{9}Be(π^-, *dd*)*t*2*n*, and (*3*) ^{9}Be(π^-, *pt*)^{4}H*n* channels.

averages, are listed in the table. The Γ values are the FWHMs of the peaks shown in the figures. Errors of the parameters presented in the table are caused by the statistical and systematic errors of measurements.

The spectral shapes and the relations between yields of resonances are noticeably different for the ^{9}Be(π^-, *pt*)X and ^{9}Be(π^-, *dd*)X reactions (Figs. 2a, 3a). This difference possibly indicates that the mechanisms of these reactions are different. Nevertheless, the parameters of the Breit–Wigner distributions for both channels coincide to within the measurement errors. Therefore, the results are reliable.

The stability of the spectroscopic data obtained for ^{5}H can be additionally tested by using the fact that quasifree processes, where the nucleons of residual nucleus are not directly involved in the reactions, contribute significantly to the three-body channels of pion-absorption reaction. With the aim of relative enrichment of the measured spectra with such events, we posed restriction on the momentum of residual nucleus ($Px < 100$ MeV/ c). This limit certainly does not exceed the expected value for the Fermi momentum of the cluster in a nucleus. The missing-mass spectra obtained with such a restriction are shown in Figs. 2b and 3b. These spectra were approximated by the Breit–Wigner distributions with parameters presented in the table. The χ^2 values per degree of freedom are equal to 1.2 and 1.1 for *pt* and *dd* events, respectively, which are consistent with the existence of four resonance states of the ^{5}H isotope.

Figures 2 and 3 also show the contributions from the multiparticle phase-space distributions to the spectra. The comparison of these distributions with the measured spectra shows that the observed features cannot be reproduced without resonance states. Since two high-excited states are less noticeable, two approximations of spectra with three resonance states sequentially excluding 18.5- and 26.7-MeV levels were tested using the χ^2 criterion. Both hypotheses can be rejected at a 10% significance level. We also note that a satisfactory approximation cannot be achieved without four-body phase-space distributions with a dineutron ^2n and (or) a ^{4}H resonance in the final state.

The ground-state resonance energy of the ^{5}H isotope, which was determined in this work, agrees with the experimental results obtained in [5] and theoretical calculations made in [8] but is higher ($\Delta E \sim 2$–3 MeV) than the experimental results from [6] and theoretical calculations [9, 10]. In our opinion, the discrepancy between the experimental data are too large. It is worth noting that the binding energy of the ^{5}H isotope, according to our measurements, is much less than for the ^{4}H isotope. This conclusion is valid even with the inclusion of uncertainty in the measurements of the resonance energy of ^{4}H, which varies from ~2 MeV [15, 16] to ~3.4 MeV [17]. This result is inconsistent with the conclusion made in [6] that the binding energy of

Resonance parameters of the ^{5}H isotope

Reaction channel				Weighted average	
^{9}Be(π^-, *pt*)^{5}H		^{9}Be(π^-, *dd*)^{5}H			
E_r, MeV	Γ, MeV	E_r, MeV	Γ, MeV	E_r, MeV	Γ, MeV
5.2 ± 0.3	5.5 ± 0.5	6.1 ± 0.4	4.5 ± 1.2	5.5 ± 0.2	5.4 ± 0.5
10.4 ± 0.3	7.4 ± 0.6	11.4 ± 0.7	5 ± 1	10.6 ± 0.3	6.8 ± 0.5
18.7 ± 0.5	3.9 ± 2.0	18.3 ± 0.5	5.5 ± 1.7	18.5 ± 0.4	4.8 ± 1.3
26.8 ± 0.4	3.0 ± 1.4	26.5 ± 1.0	6 ± 3	26.7 ± 0.4	3.6 ± 1.3

the superheavy hydrogen isotopes as a function of the number of neutrons behaves similarly to the binding energy of heavy helium isotopes: bonding is stronger for an even number of neutrons because of the neutron coupling.

The energy determined here for the ground state of ^{5}H is supported by the following arguments. First, the data are based on a larger statistical sample than in other experiments. Second, our experiment covered a wide missing-mass interval, which minimized the phase-space effects; in particular, this conclusion is illustrated by the spectra determined with a restriction on the residual momentum. Third, the phenomenological consideration of the three-body channel yields for the reactions induced by the absorption of stopped pions shows that the ground states of the residual nuclei are more populated than the excited states [13]. At the same time, the formation of other states in the ^{5}H isotope can possibly be suppressed in the reaction channels under investigation due to the effects of nuclear structure of ^{9}Be.

An important result of our measurements is the observation of several excited levels of the ^{5}H isotope. To date, experimental information about excited states of nuclei near the nucleon stability boundary is very limited and is absent for ^{5}H. At the same time, theory predicts the existence of, at least, two excited states with resonance energies ~4.5–7.5 MeV [8]. The excitation energies of these states (~2–5 MeV) are close to our value for the first excited state. The peak observed in the experiment is possibly the superposition of two levels. However, this assumption is inconsistent with the fact that its parameters are identical in two reaction channels.

We emphasize that the resonance energies of excited states of ^{5}H exceed the energy necessary for the decay into five nucleons. Excitations of this system of free nucleons are high and reach ~18 MeV (or 3.6 MeV per nucleon). The origin and the formation mechanism of such states are unclear. Compilations of light-nuclei spectroscopy [11, 12] show that the same high excitations above the decay threshold were observed only for the ^{5}He and ^{5}Li isotopes. The levels in ^{5}He and ^{5}Li with excitation energy E_x = 35.7 and 34 MeV, respectively, are, possibly, the isobar analogs for the level with E_{2r} = 18.0 MeV observed in our experiment.

In conclusion, we note that the continuation of studying superheavy hydrogen isotopes is of current interest. The solution to the problem of the effect of the structure of nuclei involved in a reaction on the population of the ^{5}H levels can possibly resolve contradictions between the results of different works. However, a search for the heavier isotopes such as ^{6}H and ^{7}H is of particular interest. At present, we continue to analyze the possible formation of these isotopes in the ^{9}Be(π^-, *pd*)X and ^{9}Be(π^-, *pp*)X reactions.

This work was supported by the Russian Foundation for Basic Research (project no. 00-02-17511), the program "Universities of Russia" (project no. UR.02.01.007), and by the U.S. Civilian Research and Development Foundation for the Independent States of the Former Soviet Union (grant no. MO-011-0).

REFERENCES

1. I. Tanihata, J. Phys. G **22**, 157 (1996).
2. K. K. Seth, in *Proceedings of 4th International Conference on Nuclei Far from Stability* (CERN, Helsingor, 1981), No. 81-90, p. 655.
3. M. G. Gornov, Yu. B. Gurov, V. P. Koptev, *et al.*, Pis'ma Zh. Éksp. Teor. Fiz. **45**, 205 (1987) [JETP Lett. **45**, 252 (1987)].
4. A. I. Amelin, M. G. Gornov, Yu. B. Gurov, *et al.*, Pis'ma Zh. Éksp. Teor. Fiz. **51**, 607 (1990) [JETP Lett. **51**, 688 (1990)].
5. D. V. Aleksandrov, E. Y. Nikol'skii, B. G. Novatskii, *et al.*, in *Proceedings of the International Conference on Exotic Nuclei and Atomic Masses (ENAM-95), Arles, France, 1995* (Frontiers, Gifsur-Yvette, France, 1995), p. 329.
6. A. A. Korsheninnikov, M. S. Golovkov, I. Tanihata, *et al.*, Phys. Rev. Lett. **87**, 092501-1 (2001).
7. A. M. Gorbatov, V. L. Skopich, P. Yu. Nikishov, *et al.*, Yad. Fiz. **50**, 1551 (1989) [Sov. J. Nucl. Phys. **50**, 962 (1989)].
8. B. Shul'gina, B. V. Danilin, L. V. Grigorenko, *et al.*, Phys. Rev. C **62**, 014312 (2000).

9. P. Descouvemont and A. Kharbach, Phys. Rev. C **63**, 027001 (2001).
10. M. G. Gornov, Yu. B. Gurov, P. V. Morokhov, *et al.*, Nucl. Instrum. Methods Phys. Res. A **446**, 461 (2000).
11. F. Ajzenberg-Selove, Nucl. Phys. A **490**, 1 (1988).
12. D. R. Tilley, C. M. Cheves, J. L. Godwin, *et al.*, Nucl. Phys. A **708**, 3 (2002).
13. M. G. Gornov, Yu. B. Gurov, S. V. Lapushkin, *et al.*, Izv. Ross. Akad. Nauk, Ser. Fiz. **62**, 1781 (1998).
14. M. G. Gornov, Yu. B. Gurov, S. V. Lapushkin, *et al.*, Phys. Rev. Lett. **81**, 4325 (1998).
15. D. V. Aleksandrov, E. Yu. Nikol'skiĭ, B. G. Novitskiĭ, *et al.*, Pis'ma Zh. Éksp. Teor. Fiz. **62**, 18 (1995) [JETP Lett. **62**, 18 (1995)].
16. M. G. Gornov, Yu. B. Gurov, S. V. Lapushkin, *et al.*, in *LI Meeting on Nuclear Spectroscopy and Atomic Nucleus Structure* (Sarov, 2001), p. 142.
17. D. R. Tilley, H. R. Weller, and G. M. Hale, Nucl. Phys. A **541**, 1 (1992).

Translated by R. Tyapaev

JETP Letters, Vol. 77, No. 7, 2003, pp. 349–352. From Pis'ma v Zhurnal Éksperimental'noĭ i Teoreticheskoĭ Fiziki, Vol. 77, No. 7, 2003, pp. 417–420.

J/ψ $c\bar{c}$ Production in e^+e^- and Hadronic Interactions¶

A. B. Kaidalov

Institute of Theoretical and Experimental Physics, Moscow, 117259 Russia

e-mail: kaidalov@heron.itep.ru

Received March 5, 2003

Predictions of the nonperturbative quark gluon strings model, based on the $1/N$ expansion in QCD and the string picture of interactions for production of states containing heavy quarks, are considered. Relations between fragmentation functions for different states are used to predict the fragmentation function of c quark to J/ψ mesons. The resulting cross section for J/ψ production in e^+e^- annihilation is in good agreement with recent the Belle result. It is argued that the associated production of $c\bar{c}$ states with open charm should give a substantial contribution to the production of these states in hadronic interactions at very high energies. © *2003 MAIK "Nauka/Interperiodica".*

PACS numbers: 13.66.Bc; 12.38.Qk

Investigation of heavy quarkonia production at high energies provides important information on QCD dynamics in an interesting region of intermediate distances from $1/m_Q$ to $r_{Q\bar{Q}}$, where m_Q is the heavy quark mass and $r_{Q\bar{Q}}$ is the radius of a heavy quarkonia state. For c and b quarks, this is the region 0.05 fm < r < 1 fm. In this region both perturbative and nonperturbative effects can be important. Production of J/ψ mesons is studied experimentally in e^+e^- annihilation, γp, hp, hA, and AA collisions. Analysis of hadronic interactions shows that the simplest perturbative approach (color singlet model) [1] does not reproduce experimental data [2]. This observation leads to an introduction of the color octet mechanism [3] of heavy quarkonia production. In this approach, a set of nonperturbative matrix elements is introduced, which is determined from a fit to data. A characteristic prediction of this approach is a large transverse polarization of J/ψ, and ψ' at large transverse momenta [4] is not supported by the Tevatron data [5].

A new mystery in the problem of heavy quarkonia production has been added by recent result of the Belle collaboration [6] on the large production of J/ψ mesons with charmed hadrons. The observed cross section at $\sqrt{s}$ = 10.6 GeV is an order of magnitude larger than theoretical predictions [7] based on perturbative QCD. It is interesting that at this energy the associated production of J/ψ with a $c\bar{c}$ pair is the dominant mechanism of J/ψ production [6].

In this paper, a nonperturbative approach, based on the $1/N$ expansion in QCD and the string picture of particle production, is used for description of heavy quarkonia production at high energies. A model based on this approach (the quark gluon strings model (QGSM) [8]) has been successfully applied to production of different hadrons at high energies. It has been also used for description of inclusive spectra of hadrons containing heavy (c, b) and light quarks [9–11]. In QGSM, the fragmentation functions, which describe transitions of strings to hadrons in many cases, can be predicted theoretically [8, 12] and are expressed in terms of intercepts of the corresponding Regge trajectories. We will show that the model naturally leads to the cross section of J/ψ production in e^+e^- annihilation consistent with the Belle result. Estimate of the contribution of the same mechanism in hadronic interactions indicates that it can be important at energies $\sqrt{s}$ = 10^2 GeV.

Let us first discuss heavy quarkonia production in e^+e^- collisions. In these reactions, a $c\bar{c}$ pair is produced directly by a virtual photon. However, the probability of transition of such a state at high energies (far above the threshold of charm production) to J/ψ is very small. The simplest diagram of QCD perturbation theory (Fig. 1a) corresponds to a transition to a white $c\bar{c}$ state with relative momentum characteristic to J/ψ by emission of two hard gluons. This cross section is sup-

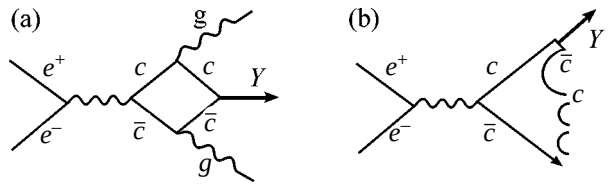

Fig. 1. Diagrams for J/ψ production in e^+e^- annihilation.

¶ This article was submitted by the author in English.

pressed at high energies by a factor $4m_c^2/s$ and at $\sqrt{s}$ = 10 GeV constitutes 10^{-3} of the total $c\bar{c}$ cross section [7].

J/ψ production in association with an extra charmed pair (Fig. 1b) does not have this suppression but contains a smallness due to the production of this pair and a high threshold of the processes. At high energies, this mechanism can be considered as a fragmentation of $c(\bar{c})$ to J/ψ. Calculation in the lowest order of QCD perturbation theory [7] shows that this mechanism is important at energies $\sqrt{s} \geq 50$ GeV but at $\sqrt{s} = 10$ GeV is smaller than the mechanism of Fig. 1a by an order of magnitude and is about 0.07 pb. This is in sharp contradiction with the Belle result: $\sigma(J/\psi c\bar{c}) = 0.87^{+0.21}_{-0.19} \pm 0.17$ pb.

Note that, for states of comparatively large radius, such as J/ψ and especially ψ' or χ_c, a nonperturbative fragmentation can be important. Thus, I shall estimate a fragmentation of $c(\bar{c})$ into J/ψ using the nonperturbative model mentioned above. In this model, particle production is described in terms of production and fragmentation of quark–gluon strings. The behavior of the fragmentation functions is determined in the limit $z \longrightarrow 1$ from the corresponding Regge limit and is expressed in terms of Regge intercepts $\alpha_i(0)$ [8, 12]. The fragmentation function of a c quark to J/ψ in this model is written in the form [12]

$$D_c^{\psi} = a_{\psi} z^{-\alpha_{\psi}(0)} (1-z)^{-\alpha_{\psi}(0)+\lambda}, \quad (1)$$

where $\alpha_{\psi(0)}$ is an intercept of the J/ψ Regge trajectory, which is known from analysis of data on the spectrum of $c\bar{c}$ states and analysis of inclusive spectra of charmed particles (see below), $\lambda = 2\alpha'_{D^*}\overline{p_{\perp D}^2} \approx 1$. Thus, this fragmentation function is characterized by one constant, a_{ψ}. In order to determine this constant, we will use a relation between the fragmentation function of a c quark to J/ψ and the fragmentation function of a light quark to a D (D^*) meson in the limit $z \longrightarrow 1$. According to the rules formulated in [12, 13], both functions have the same behavior on z: $(1-z)^{(-\alpha_{\psi}(0)+\lambda)}$ as $z \longrightarrow 1$ and differ only by a kinematic factor related to the mass difference between the J/ψ and D (D^*) meson

$$R^{D/\psi} \equiv \frac{D_u^D}{D_c^{\psi}} = \left(\frac{s_{0D}^{uc}}{s_{0\psi}^{uc}}\right)^{2(1-\alpha_{D^*}(0))}. \quad (2)$$

The quantities s_{0i} will be determined below.

Now we shall find the fragmentation function D_u^D in the limit $z \longrightarrow 1$. In this limit, it is related to the fragmentation function of a light quark to π meson [12]

$$R_u^{D^+/\pi^+} \equiv \frac{D_u^{D^+}}{D_u^{\pi^+}} = \frac{\Gamma^2(1-\alpha_D^*(0))}{\Gamma^2(1-\alpha_{\rho}(0))}\left(\frac{s_0^{uc}}{\overline{m_{D\perp}^2}}\right)^{2(1-\alpha_{D^*}(0))} \times \left(\frac{\overline{m_{\pi\perp}^2}}{s_0^{uu}}\right)^{2(1-\alpha_{\rho}(0))} (1-z)^{2(\alpha_{\rho}(0)-\alpha_{D^*}(0))}, \quad (3)$$

where α_{ρ}, $\alpha_{D^*}(0)$ are intercepts of the ρ and D^* Regge trajectories. They are related to $\alpha_{\psi}(0)$ by the equation [14]

$$\alpha_{\rho}(0) + \alpha_{\psi}(0) = 2\alpha_{D^*}(0). \quad (4)$$

I shall use the following values for these intercepts: $\alpha_{\rho}(0) = 0.5$, $\alpha_{\psi}(0) = -2$, and $\alpha_{D^*}(0) = -0.75$, in accord with Eq. (4). The uncertainty in the value of $\alpha_{\psi}(0)$ discussed in [9] is eliminated at present by experimental data on the inclusive spectra of charmed hadrons in hadronic collisions.

The gamma functions in Eq. (3) appear from Regge residues of the corresponding trajectories, which were chosen in accord with dual models and are in a good agreement with data on widths of hadronic resonances [15]. The coupling is assumed to be universal (with an account of $SU(4)$ and heavy quark symmetry).

The quantities s_{0i} entering in Eq. (3) can be easily calculated using the formulas and parameters of [13]

$$(s_0^{uc})^{2\alpha_{D^*}(0)} = (s_0^{uu})^{\alpha_{\rho}(0)} (s_0^{D\bar{D}})^{\alpha_{\psi}(0)}; \quad (5)$$

$$s_0^{uu} = 4m_{u\perp}^2 = 1 \text{ GeV}^2; \quad s_0^{D\bar{D}} = (m_{c\perp} + m_{u\perp})^2. \quad (6)$$

With $m_{u\perp} = 0.5$ GeV and $m_{c\perp} = 1.6$ GeV [13], we obtain $(s_0^{uc}) = 3.57$ GeV. Using these values for s_{0i} in Eq. (3) and $\overline{m_{\pi\perp}^2} = 0.18$ GeV^2, $\overline{m_{D\perp}^2} = 5$ GeV^2, and the fragmentation function $D_u^{\pi^+} = 0.44$ [8], we obtain the function $D_u^{D^+}$ at $z \longrightarrow 1$ in the form $0.01(1-z)^{(-\alpha_{\psi}(0)+\lambda)}$. This value is in reasonable agreement with phenomenological studies of charmed particle production in hadronic interactions in the framework of QGSM [10, 11].

The value of $s_{0\psi}^{uc}$ in Eq. (2) can be calculated in the same way with the substitution $s_0^{D\bar{D}} \longrightarrow s_0^{\psi\bar{D}} = 6.72$ GeV^2. Finally, we obtain from Eq. (2)

$$D_c^{\psi} = 0.05(1-z)^{(-\alpha_{\psi}(0)+\lambda)}; \quad z \longrightarrow 1. \quad (7)$$

Thus, $a_{\psi} = 0.05$.

At asymptotic energies $s \longrightarrow \infty$, the cross section for J/ψ production in e^+e^- annihilation is equal to

$$\sigma_\psi = 2\sigma_{c\bar{c}}\int_0^1 D_c^\psi(z)dz; \quad (8)$$

the factor of 2 in Eq. (8) takes into account J/ψ production by both c and $\bar{c}$ quarks. At energy $\sqrt{s} \sim 10$ GeV, there is an extra suppression due to phase space corrections for production of a heavy state. We estimate it by introducing an extra factor $\gamma = \sqrt{1-4M_D^2/M_{c\bar{c}}^2}$ into Eq. (8). The distribution in $M_{c\bar{c}}^2$ is related to the z distribution. It has a maximum at $M^2 \approx 0.27$ s. For the energy of Belle experiment, the correction factor $\gamma = 0.7$. Thus, we obtain the following cross section for J/ψ $c\bar{c}$ production at $\sqrt{s} = 10.6$ GeV $\sigma_\psi = 1.2$ pb. This value is in a good agreement with the Belle result [6] and is much larger than the perturbative QCD prediction [7]. The estimated uncertainty in the value of the cross section due to possible variation of quantities s_{0i}, $m_{i\perp}$, and $\alpha_i(0)$ is about 50%.

Let us consider now J/ψ production in hadronic interactions. In the approach based on the $1/N$ expansion [16], the main diagrams for particle production correspond to two-chain configurations, shown for pp interactions in Fig. 2a [8]. They can be considered as production and fragmentation of two q–qq strings. It is important to emphasize that production of one $c\bar{c}$ pair together with light quark pairs in this approach always leads to an open charm production (Fig. 2b), and J/ψ in this case is produced by the OZI forbidden mechanism [17]. This leads to a strong suppression ($\sim 10^{-2}$) for heavy quarkonia production in hadronic collisions compared to open charm (beauty) production. To produce J/ψ in the chains by the OZI allowed mechanism, it is necessary to produce two $c\bar{c}$ pairs close in rapidity (Fig. 2c). Though this mechanism is suppressed due to production of extra heavy quark pairs, it can compete at very high energy with the mechanism of single $c\bar{c}$-pair production. Its contribution can be estimated from charm quark fragmentation into heavy quarkonia in e^+e^- annihilation. Consider production of a $c\bar{c}$ pair in the q–qq string of Fig. 2. In each of the q–$\bar{c}$ and c–qq substrings, an extra $c\bar{c}$ pair can be produced and fragment to a given quarkonium state. So it is possible to use the estimate of the fragmentation function of c ($\bar{c}$) quarks given above or direct experimental data from e^+e^- to determine the contribution of the corresponding diagrams to quarkonia production. This calculation is rather straightforward except for a threshold suppression factor. It is clear that, at the energies of fixed-target experiments $\sqrt{s} = 10$–40 GeV, there is a strong suppression of the production of J/ψ and extra $D\bar{D}$ pair. I shall estimate this suppression factor for the energy of the HERA-B experiment [18] $E_{\text{lab}} = 920$ GeV. Let us denote an extra suppression factor compared to the suppression of a single $c\bar{c}$ pair by γ_{pp}. For its estimation, it is possible to introduce the same kinematical factors as in e^+e^- collisions for each q–$\bar{c}$ and c–qq subchain. For J/ψ production at rapidity $y = 0$, $\gamma_{pp} \approx 0.5$. Another estimate can be made by assuming that the J/ψ–$D\bar{D}$ system is produced by gluon fusion. This gives $\gamma_{pp} \approx 0.4$. Using these estimates and taking into account that $\sigma_{pp}^\psi/\sigma_{pp}^{c\bar{c}} \approx 10^{-2}$, we find that the associated production of J/ψ with charmed hadrons constitutes at this energy ~10%. At Tevatron energies, the role of this mechanism is more important, and it can (at least partly) explain the excess of J/ψ production at Tevatron compared to the color singlet model.

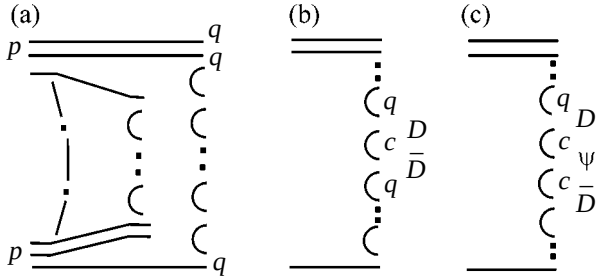

Fig. 2. Diagrams for J/ψ production in pp interactions.

For ψ', associated production with $c\bar{c}$ in e^+e^- annihilation is not yet known experimentally. However, its total inclusive yield is close to the one for J/ψ [19]. If the probability of ψ' production by c-quark fragmentation is the same as for J/ψ, it will have an even stronger impact on ψ' production in hadronic collision, because the experimental ψ' cross section is smaller than for J/ψ: $\sigma_{pp}^{\psi'}/\sigma_{pp}^{c\bar{c}} \approx 1.6 \times 10^{-3}$, and associated production can constitute a large fraction of the ψ' production.

In conclusion, it was demonstrated that the nonperturbative QGSM model predicts a sizable J/ψ $c\bar{c}$ production in e^+e^- annihilation at high energies, consistent with recent experimental results [6]. In the approach based on the $1/N$ expansion in QCD, it was shown that a large fraction of $c\bar{c}$-quarkonia production in hadronic collisions at very high energies can be due to associated production with charmed hadrons.

I thank K. Boreskov and O.V. Kancheli for useful discussions. I am especially grateful to M.V. Danilov for drawing my attention to this problem and discussion of results of the Belle collaboration.

This work is supported in part by INTAS (grant no. 00-00366), NATO (grant no. PSTCLG-977275), and the Russian Foundation for Basic Research (grant nos. 00-15-96786 and 01-02-17383).

REFERENCES

1. J. H. Kuhn, J. Kaplan, and E. G. O. Safiani, Nucl. Phys. B **157**, 125 (1979); C. H. Chang, Nucl. Phys. B **172**, 425 (1980); E. L. Berger and D. Jones, Phys. Rev. D **23**, 1521 (1981).
2. M. Cacciari, in *Proceedings of the XXX Rencontres de Moriond, Les Arcs, France, 1995*, Ed. by J. Tran Thanh Van (Frontiers, Paris, 1995), p. 327.
3. E. Braaten and T. C. Yuan, Phys. Rev. Lett. **71**, 1673 (1993); M. Cacciari and M. Greco, Phys. Rev. Lett. **73**, 1586 (1994); D. P. Roy and K. Stridhar, Phys. Lett. B **339**, 141 (1994).
4. P. Cho and M. B. Wise, Phys. Lett. B **346**, 129 (1995).
5. T. Affolder *et al.* (CDF Collaboration), hep-ex/0004027.
6. K. Abe *et al.* (Belle Collaboration), Phys. Rev. Lett. **89**, 142001 (2002).
7. P. Cho and A. K. Leibovich, Phys. Rev. D **54**, 6690 (1996).
8. A. B. Kaĭdalov, Yad. Fiz. **33**, 1369 (1981) [Sov. J. Nucl. Phys. **33**, 733 (1981)]; A. B. Kaidalov, Phys. Lett. B **116**, 459 (1982); A. B. Kaidalov and K. A. Ter-Martirosyan, Phys. Lett. B **117**, 247 (1982); A. B. Kaĭdalov and K. A. Ter-Martirosyan, Yad. Fiz. **39**, 1545 (1984) [Sov. J. Nucl. Phys. **39**, 979 (1984)]; Yad. Fiz. **40**, 211 (1984) [Sov. J. Nucl. Phys. **40**, 135 (1984)]; A. B. Kaidalov, in *QCD at 200 TeV*, Ed. by L. Cifarelli and Yu. Dokshitzer (Plenum, New York, 1992), p. 1.
9. A. B. Kaĭdalov and O. I. Piskunova, Yad. Fiz. **43**, 1545 (1986) [Sov. J. Nucl. Phys. **43**, 994 (1986)].
10. O. I. Piskunova, Yad. Fiz. **56** (8), 176 (1993) [Phys. At. Nucl. **56**, 1094 (1993)].
11. G. G. Arakelyan, Yad. Fiz. **61**, 1682 (1998) [Phys. At. Nucl. **61**, 1570 (1998)].
12. A. B. Kaĭdalov, Yad. Fiz. **45**, 1452 (1987) [Sov. J. Nucl. Phys. **45**, 902 (1987)].
13. K. G. Boreskov and A. B. Kaĭdalov, Yad. Fiz. **37** (1), 174 (1983) [Sov. J. Nucl. Phys. **37**, 100 (1983)].
14. A. B. Kaidalov, Z. Phys. C **12**, 63 (1982).
15. A. B. Kaĭdalov and P. E. Volkovitskiĭ, Yad. Fiz. **35**, 1556 (1982) [Sov. J. Nucl. Phys. **35**, 909 (1982)].
16. G. t'Hooft, Nucl. Phys. B **72**, 461 (1974); G. Veneziano, Phys. Lett. B **52**, 220 (1974); G. Veneziano, Nucl. Phys. B **117**, 519 (1976).
17. G. G. Arakelyan, K. G. Boreskov, and A. V. Turbiner, Yad. Fiz. **41**, 1015 (1985) [Sov. J. Nucl. Phys. **41**, 651 (1985)].
18. HERA-B: Report on Status and Prospects, DESY-PRC 00/04.
19. K. Abe, K. Abe, T. Abe, *et al.*, Phys. Rev. Lett. **88**, 052001 (2002).

JETP Letters, Vol. 77, No. 7, 2003, pp. 353–357. Translated from Pis'ma v Zhurnal Éksperimental'noĭ i Teoreticheskoĭ Fiziki, Vol. 77, No. 7, 2003, pp. 421–425.

Spatiotemporal Self-Organization upon Two-Wave Mixing in a Photorefractive Medium

P. A. Prudkovskiĭ

Faculty of Physics, Moscow State University, Vorob'evy gory, Moscow, 119992 Russia

e-mail: pasha@qopt.phys.msu.su

Received 2003

Nonlinear dynamics of recording volume holographic gratings upon two-wave mixing in an inertial photorefractive media were studied. It is found that the space–time dependence of the grating diffraction efficiency can be quasi-regular, allowing the understanding of the experimentally observed irregular behavior of the diffracted light intensity. © *2003 MAIK "Nauka/Interperiodica".*

PACS numbers: 42.40.Pa; 42.40.Lx; 42.70.Nq; 42.65.Hw

Investigations into photorefraction, i.e., into the processes of light-induced change in the refractive index of a medium, have allowed one to discover many new photorefractive materials in the last several decades and find numerous applications for them [1, 2]. However, with the development of the hologram record technique and information storage in such media, it has become clear that wave-mixing processes may be much more complicated than was assumed previously [3].

In this work, we discuss certain features of wave mixing in a photorefractive medium in the course of recording volume holographic grating by two crossing light beams. The time dependence of the diffraction efficiency of the recorded grating, as a rule, is smooth and practically monotonic at low light intensities or in media with weak photorefractive nonlinearity [4, 5]. However, an increase in the light intensity or the use of stronger nonlinearities may be accompanied by sharp differentials in the diffraction efficiency and their sensitivity to the experimental conditions. In this work, it is shown that such a jumpwise behavior of diffraction efficiency of a volume holographic grating is a consequence of the formation of a regular spatiotemporal structure in the course of recording grating in an inertial photorefractive medium.

Description of the model. We consider the standard model of recording holographic grating in a medium with photorefractive response. Two coherent light beams intersect in a medium to form an interference pattern. Due to the diffusion or photovoltaic effect, the electric-charge carriers are rearranged in the medium to produce an electrostatic field which modulates the refractive index through the electrooptical effect. Therefore, the state of light and medium is specified by three complex field variables: slowly varying field amplitudes of two beams $E_{1,2}(x, t)$ and spatially oscillating amplitude of electrostatic field $\mathscr{E}(x, t)$. In the approximation of a perfectly transparent medium, their spatiotemporal evolution is described by a set of partial differential equations, which can be written in the form [6–8]

$$\begin{gathered}\frac{\tau_m \partial \mathscr{E}}{\partial t} + \mathscr{E} = \gamma E_1, E_2^*, \\ \frac{\partial E_2}{\partial x} = i\mathscr{E}^* E_1, \quad \frac{\partial E_1}{\partial x} = i\mathscr{E} E_2,\end{gathered} \tag{1}$$

where $\tau_m = \varepsilon/4\pi\sigma$ is the characteristic Maxwellian response time of the medium, ε is its dielectric constant, σ is conductivity, and $\gamma = Ge^{i\varphi}$ is the effective photorefraction coefficient, which includes a combination of the photovoltaic and electrostatic tensor components and the diffusion coefficient.

From the second and third equations, it follows that the total light intensity in the system is constant: $|E_1|^2 + |E_2|^2 = \text{const} = I_0$. Taking into account this conservation law, it is convenient to make the change of variables $E_1 = \sqrt{I_0}e^{i\psi_1}\cos(\beta/2)$ and $E_2 = \sqrt{I_0}e^{i\psi_2}\sin(\beta/2)$. In the new variables, system (1) takes the form

$$\begin{gathered}\frac{\partial \mathscr{E}}{\partial \tau} + \mathscr{E} = \sin\beta e^{-i\psi}, \\ \frac{\partial \beta}{\partial y} - i\tan\beta\frac{\partial \psi}{\partial y} = -i\mathscr{E}e^{i(\psi+\varphi)},\end{gathered} \tag{2}$$

where the variables $\mathscr{E} = 2\mathscr{E}/\gamma I_0$, $\psi = \psi_2 - \psi_1$, and new time and length scales

$$\tau = t/\tau_m, \quad y = GI_0 x \tag{3}$$

are introduced. Therefore, the behavior of the system depends qualitatively on a single parameter φ, which determines the ratio between the real and imaginary components of the photorefraction coefficient γ. The behavior of all remaining parameters can be taken into

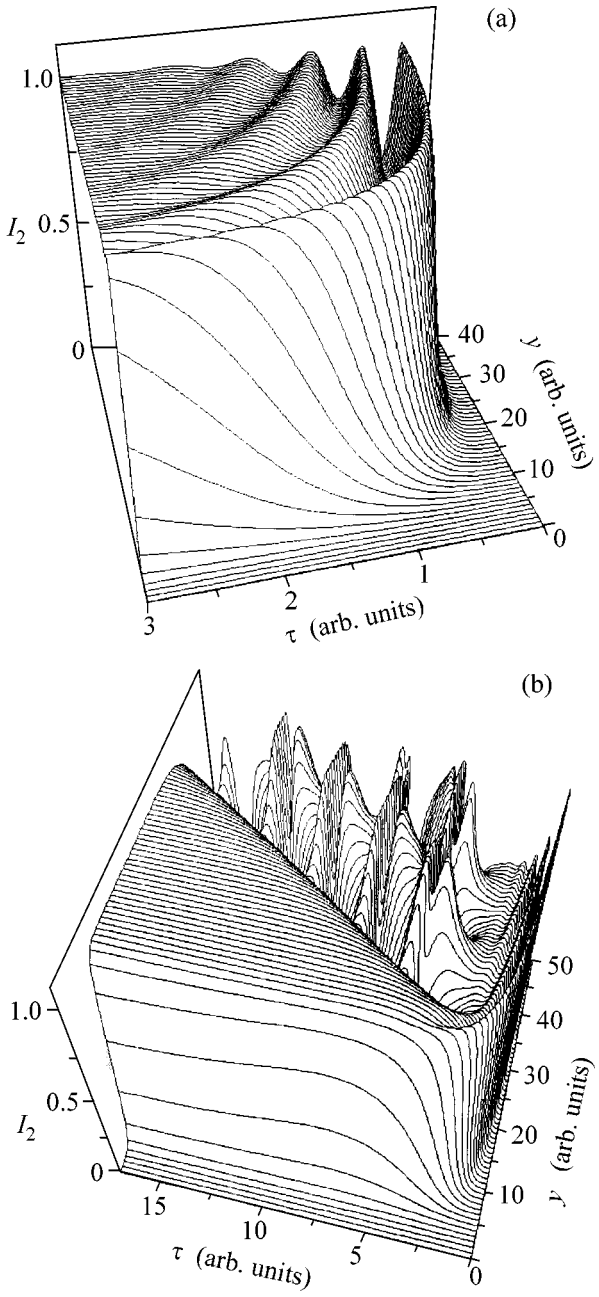

Fig. 1. Three-dimensional intensity profile for the secondary light beam I_2 as a function of time τ and thickness y of the photorefractive medium for (a) purely imaginary coefficient γ of photorefractive nonlinearity ($\varphi = \pi/2$) and (b) equal real and imaginary parts of this coefficient ($\varphi = \pi/4$).

account by changing the space and time scales. In particular, the variation of light intensity I_0 is equivalent to changing the thickness of photorefractive medium.

It is known [9, 10] that the recorded holographic grating for real γ is not shifted relative to the interference pattern. In this case, stationary energy exchange is impossible; after the termination of recording grating, the beam intensities in the photorefractive medium are not rearranged. In all other cases, the intensity of one beam will transfer to another (in our notation, energy transfer occurs from the first to the second beam if $0 < \varphi < \pi$).

In the case of imaginary photorefractive nonlinearity $\varphi = \pi/2$ (which corresponds, in particular, to the diffusional photorefraction mechanism), the system can be simplified, because there is a stable solution of the form $\arg\mathscr{E} = \pi n - \psi = \text{const}$. The rest of the set of Eqs. (2) amounts to the equation

$$\frac{\partial^2\beta}{\partial y\partial\tau} + \frac{\partial\beta}{\partial\tau} = \sin\beta, \qquad (4)$$

which has the form of a modified sine-Gordon equation with the additional first derivative. The analytic solution to this equation and to the complete set of Eqs. (2) cannot be found. For this reason, we present here only numerical solutions.

Results of numerical integration. The set of Eqs. (2) consists of four real equations, two of which contain only time derivatives and the other two contain only spatial derivatives. Due to this, one can easily develop a computational algorithm based on the numerical integration of the two parts of system (2), similar to the usual differential equations, to obtain the solution by specifying the intensity ratio $I_2/I_1|_{y=0} \equiv I_{02}/I_{01} = \tan(\beta_0/2)$ and phase difference $\psi|_{y=0} \equiv \psi_0$ for two light beams at the medium input as boundary conditions and the absence of electrostatic field $\mathscr{E}$ at $\tau = 0$ as the initial condition. The numerical integration gave the spatiotemporal dependences for the second-beam intensity normalized to the total intensity I_0, with the boundary conditions $\psi_0 = 0$, $I_{02}/I_0 = 10^{-4}$ and various phases of the photorefractive nonlinearity coefficient φ. For such a low initial input intensity of the second beam, its output intensity is a measure of the diffraction efficiency of the recorded grating.

Figure 1a shows the three-dimensional intensity profile of the second beam for the imaginary coefficient γ ($\varphi = \pi/2$). It demonstrates the dependence of intensity on both time and length. One can see that the obtained solution describes a smooth increase in the intensity of the second beam at the output of photorefractive medium with small damping oscillations near the maximum. This is precisely the behavior that was considered classical for the processes of recording holograms and photoinduced light scattering at the dawn of photorefraction [5].

However, in the general case, the behavior of light intensity at the output of the photorefractive medium may be much more complicated. Figure 1b shows the three-dimensional intensity map for the second beam in the case of γ with equal real and imaginary parts ($\varphi = \pi/4$). One can see that the evolution of beam intensity at short lengths is almost the same as in the case of imaginary γ. Recall that, on the scale adopted, the effective

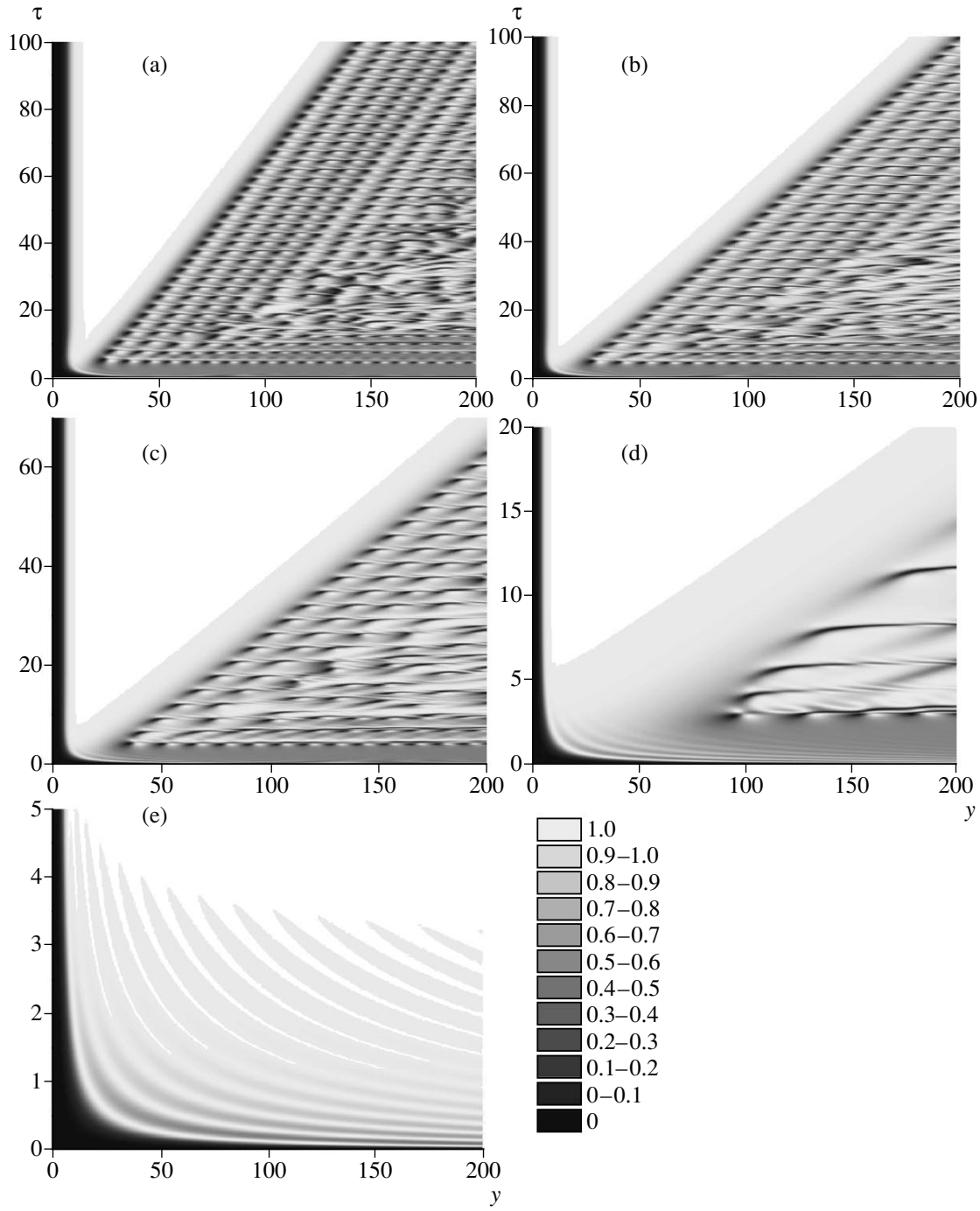

Fig. 2. Two-dimensional intensity distribution for the second beam I_2 as a function of time τ and thickness y of the photorefractive medium for different phases φ of the photorefractive nonlinearity coefficient γ: φ = (a) $\pi/5$, (b) $\pi/4$, (c) $3\pi/10$, (d) $2\pi/5$, and (e) $\pi/2$.

length unit depends both on the total light intensity and on the magnitude of photorefractive nonlinearity (3). Since the laser intensity in the early studies of photorefraction was too low to produce a strong light field, the effective thicknesses of photorefractive media were rather small, so that almost all observed dependences were smooth and monotonic. However, for the larger interaction lengths (or beam intensities), the time dependences contain a strongly fluctuating region, whose length increases approximately proportional to the interaction length.

Let us consider a set of spatiotemporal dependences for the intensity of second beam and various values of phase φ. The corresponding dependences are shown in Fig. 2 in the form of two-dimensional brightness distributions (Fig. 2a corresponds to Fig. 1a, and Fig. 2d cor-

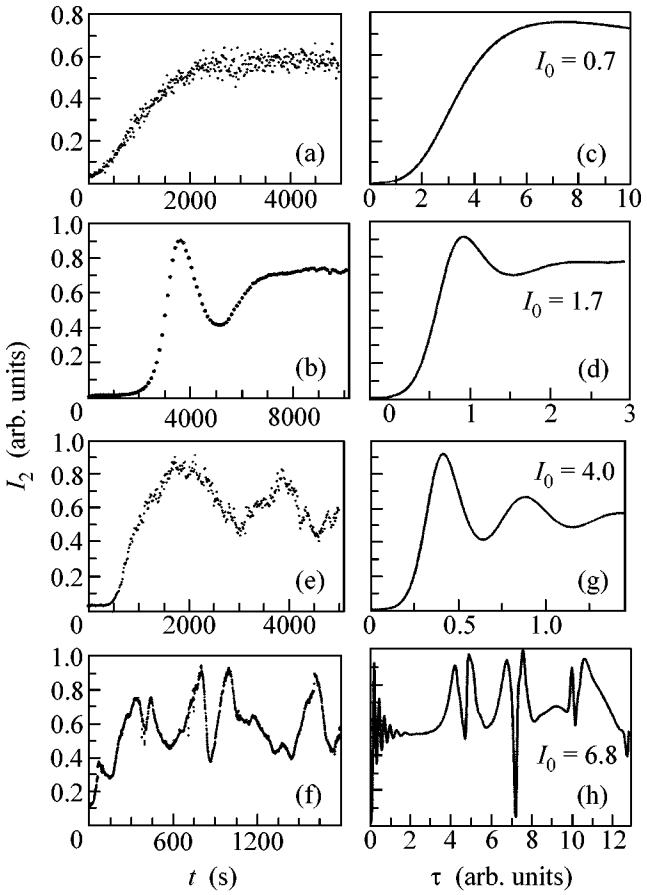

Fig. 3. Comparison of the experimental time dependences of the intensity I_2 of the second beam (a, b, e, f) with the analogous theoretical dependences for different total light intensities I_0 (c, d, g, h).

responds to Fig. 1b). One can see that, if the photorefraction coefficient has a nonzero real part, the whole τ–y plane can be separated into two regions divided by a near-straight line emerging from the origin of coordinates. In the upper part adjacent to the time axis, the intensity I_2 rapidly and more or less monotonically increases and becomes saturated at $I_2 = I_0$. At the same time, the two-dimensional structure formed in the region adjacent to the spatial axis is rather complicated and has a regular quasiperiodic character. It should be noted that the slope of the line separating the regions increases with decreasing phase φ.

Let us now compare these results with the experimental data.

Comparison with experiment. The experimental curves presented below were obtained while studying two-wave mixing, photoinduced light scattering, and parametric scattering of holographic type in photorefractive copper-doped lithium niobate crystals [11, 12]. Two light beams were brought together in a photorefractive crystal, with the intensity of one of them being approximately four orders of magnitude higher than for the other. The Maxwellian time in such crystals equals several tens of minutes and decreases with increasing light intensity because of an increase in the photoelectron conductivity. As the process of holographic grating evolves, the intensity of the first beam is partly transferred to the second beam.

To compare with the experimental data, the $I_2(\tau)$ dependences were extracted from the complete solution to Eqs. (2) with various effective thicknesses of the photorefractive medium.

The experimental curves for the intensity I_2 of the second beam at the output of a photorefractive crystal are shown in Figs. 3a and 3b for relatively low intensities of the first beam, and the appropriate theoretical curves obtained for various effective thicknesses are shown in Figs. 3c and 3d. As was pointed out above, the length scale depends on the total light intensity; because of this, the increase in the effective thickness corresponds to the increase in the intensity of the first beam for a fixed crystal thickness. Figures 3e and 3f and Figs. 3g and 3h show, respectively, the corresponding theoretical curves for higher intensities of the first beam; I_1 in Fig. 3e is higher than the intensity of the first beam in Fig. 3a by almost an order of magnitude, and I_1 in Fig. 3e is one order of magnitude higher than the analogous intensity in Fig. 3b. It is seen from these graphs that the theoretical curves obtained by the numerical integration of Eqs. (2) describe not only the smooth evolution of the energy-exchange process at low intensities but also the sharp changes in the diffraction efficiency of holographic grating at high light intensities or large thicknesses of the photorefractive medium (Fig. 3e).

Thus, it is shown in this work that the spatiotemporal dependence of the diffraction efficiency of a holographic grating may have a complex quasi-regular structure if the coefficient of photorefraction nonlinearity is complex and the pumping is strong enough (Fig. 2). This is manifested experimentally in the form of sharp intensity differences in the intensity of diffracted light (Fig. 3e). The boundary of this structure in the τ–y plane is a straight line emerging from the origin of coordinates. Its slope depends on the phase of the coefficient of photorefractive nonlinearity. This, in principle, provides an original method of measuring the ratio between the real and complex parts of the photovoltaic tensor components.

This work was supported by the Russian Foundation for Basic Research (project no. 02-02-16843) within the framework of the program “Fundamental Optics and Spectroscopy.”

REFERENCES

1. T. R. Volk, N. V. Razumovski, A. V. Mamaev, and N. M. Rubinina, J. Opt. Soc. Am. B **13**, 1457 (1996).

2. V. A. Vysloukh, V. Kutuzov, and V. V. Shuvalov, Kvantovaya Élektron. (Moscow) **23**, 157 (1996).
3. V. A. Vysloukh, V. Kutuzov, V. M. Petnikova, and V. V. Shuvalov, Zh. Éksp. Teor. Fiz. **111**, 705 (1997) [JETP **84**, 388 (1997)].
4. F. S. Chen, J. T. La Macchia, and D. V. Fraser, Appl. Phys. Lett. **13**, 223 (1968).
5. K. N. Zabrodin and A. N. Penin, Kvantovaya Élektron. (Moscow) **18**, 622 (1991).
6. M. Cronin-Golomb, J. O. White, B. Fisher, and A. Yariv, Opt. Lett. **7**, 313 (1982).
7. A. Novicov, S. Odoulov, O. Oleinik, and B. Sturman, Ferroelectrics **66**, 1 (1986).
8. P. A. Prudkovskiĭ, O. V. Skugarevskiĭ, and A. N. Penin, Vestn. Mosk. Univ., Ser. 3: Fiz., Astron. **5**, 38 (1998).
9. B. Ya. Zel'dovich, Kratk. Soobshch. Fiz. **5**, 20 (1970).
10. V. L. Vinetskiĭ, N. V. Kukhtarev, S. G. Odulov, and M. S. Soskin, Usp. Fiz. Nauk **129**, 113 (1979) [Sov. Phys. Usp. **22**, 742 (1979)].
11. P. A. Prudkovskiĭ, O. V. Skugarevskiĭ, and A. N. Penin, Zh. Éksp. Teor. Fiz. **112**, 1490 (1997) [JETP **85**, 812 (1997)].
12. P. A. Prudkovskiĭ and A. N. Penin, Pis'ma Zh. Éksp. Teor. Fiz. **70**, 660 (1999) [JETP Lett. **70**, 673 (1999)].

Translated by V. Sakun

JETP Letters, Vol. 77, No. 7, 2003, pp. 358–361. Translated from Pis'ma v Zhurnal Éksperimental'noĭ i Teoreticheskoĭ Fiziki, Vol. 77, No. 7, 2003, pp. 426–429.

Direct Observation of Anomalously Low Longitudinal Electron Heat Conductivity in the Course of Collective Relaxation of a High-Current Relativistic Electron Beam in Plasma

A. V. Arzhannikov, V. T. Astrelin, A. V. Burdakov*, I. A. Ivanov, V. S. Koĭdan, K. I. Mekler, V. V. Postupaev, A. F. Rovenskikh, S. V. Polosatkin, and S. L. Sinitskiĭ

Budker Institute of Nuclear Physics, Siberian Division, Russian Academy of Sciences, pr. Akademika Lavrent'eva 11, Novosibirsk, 630090 Russia

** e-mail: A.V.Burdakov@inp.nsk.su*

Received January 28, 2002; in final form, February 18, 2003

The experimental results on a multiple-mirror trap GOL-3 with a short section of reduced magnetic field ("magnetic pit") are presented. The reduced specific energy release from a relativistic electron beam in the pit brings about a region with a temperature several times lower than in the surrounding plasma. The existence of the low-temperature region directly demonstrates that the longitudinal electron heat conductivity is suppressed in the collective electron-beam interaction with plasma. © *2003 MAIK "Nauka/Interperiodica".*

PACS numbers: 52.25.Fi; 52.40.Mj; 52.55.Jd

1. Introduction. It is generally believed in plasma physics that turbulence enhances transport coefficients and, correspondingly, reduces plasma temperature and energy confinement time. This is largely caused by the fact that the overwhelming majority of experimental and theoretical studies on the physics of fusion plasma mainly deal with devices of the tokamak type or other toroidal systems, in which the plasma energy is lost transverse to a magnetic field. As distinct from such devices, high electron temperature in open magnetic systems, as a rule, cannot be attained because of the energy loss through the longitudinal electron heat-conductivity channel. The reactor horizons of open systems largely depend on whether these losses can be reduced or not.

In the GOL-3 experiments with plasma heating by a high-current microsecond relativistic electron beam [1], an electron temperature of ~1 keV was achieved, and, after modernization of this device [2], up to 2–3 keV at a density of $\sim 10^{15}$ cm^{-3}. Both the absolute value of temperature and its nonuniform distribution along the device length during ~5 μs could not be explained by the assumption that the plasma energy is lost due to the classical electron heat conductivity. To explain these experimental results, it was assumed in [3] that an abnormally high electron-scattering frequency caused by a strong turbulence occurring in the course of electron-beam injection into plasma reduces the longitudinal electron heat conductivity by two to three orders of magnitude, as compared to the classical conductivity (this problem is considered in more detail in [4]). Such effects were probably observed in the experiments on the collective interaction of nanosecond electron beams with plasma (see, e.g., [5]); however, due to the short duration of the process (~50 ns), they did not appreciably alter the dynamics of beam-heated plasma. Various mechanisms of anomalous collision frequency in turbulent plasma (see, e.g., [6] and review [7]) and in the electron-beam systems are known (see, e.g., review [8]). In our case, the following mechanism can be responsible for this anomaly: during the collective relaxation, the electron beam excites intense resonance (Langmuir) plasma oscillations. In the case of nonlinear relaxation of these oscillations, whose level can achieve the modulation instability threshold, an intense ion sound can arise, together with density modulations associated with Langmuir collapse processes (a detailed study of turbulent processes accompanying the relativistic electron-beam relaxation in a magnetized plasma was performed on a device with different parameters [9, 10]).

Recently, the magnetic system of the GOL-3 device has been modernized. The main purpose of the modernization was to produce corrugated magnetic-field sections at the solenoid ends (with the aim of studying plasma heating and confinement in a multiple-mirror magnetic system). In the course of these developments, an experiment with a reduced magnetic-field section in the center of a solenoid was also carried out. It is the purpose of this work to discuss some results of this experiment.

2. Statement of the experiment and diagnostics. In the experiments under discussion, the solenoid of the

GOL-3 device was comprised of 110 coils with independent power supply and a total length of 12 m and arranged as three sections. A four-meter section with a uniform magnetic field of 4.8 T was in the center. The corrugated-field sections, each composed of 20 corrugation periods with a maximum field of 5.2 T, a minimum field of 3.2 T, and a step of 22 cm, were adjacent at both its sides. The solenoid was ended by single magnetic mirrors with a field of 9 T. The initial hydrogen or deuterium plasma with an average density of ~10^{15} cm^{-3} and a temperature of 2–3 eV along the length was produced using a special linear discharge in a 10-cm-diameter metallic vacuum chamber placed inside the solenoid. Then a relativistic electron beam was injected into this plasma, with the following parameters: electron energy ~0.9 MeV, current ~25 kA, base duration ~8 μs, and energy content ~120 kJ. The beam diameter in the uniform-field section was about 6 cm.

In the experiments, a special region with a reduced magnetic field was created in the central section of the solenoid, with the center at Z = 659 cm (hereafter, the longitudinal coordinate is measured from the middle of the input mirror) and a distance between neighboring coils 4 cm larger than in the remaining part of the solenoid. The diameter of the vacuum chamber was also increased to 150 mm in a region of length 42 cm. The coils adjacent to Z = 659 cm had an independent power supply and could be switched off in some experiments. The magnetic field at this point was 3.8 T for the switched-on adjacent coils and 1.3 T for the switched-off coils. In the latter case, the magnetic field formed a local trap (“magnetic pit”) with a length of about 30 cm.

Plasma heating and confinement were examined using several diagnostics (see, e.g. [2]). In this work, we will mainly focus on the results of diamagnetic measurements (about 25 coils were placed along the length of the device). Each of the “standard” coils was a loop enveloping the plasma column (the walls of vacuum chamber can be considered as pit-conducting for times discussed in this work). The coil placed in the magnetic-pit region had a different design and was shaped like a ring segment. It was placed at Z = 659 cm in a diagnostic port near the plasma column boundary. This fact should be taken into account in the discussion of the experimental results (the absolute calibration accuracy for this coil in a magnetic field of 1.3 T was low because of the difficulties associated with taking into account the skin currents in the device elements in this regime; it can be estimated at 30%).

3. Results and discussion. The typical signal oscillograms for the strong and weak field in the central magnetic pit are presented in the Fig. 1. For reference, the signals from a voltage divider of the beam generator and a detector of hard X-ray emission from the surface of an output beam collector are also shown in Fig. 1.

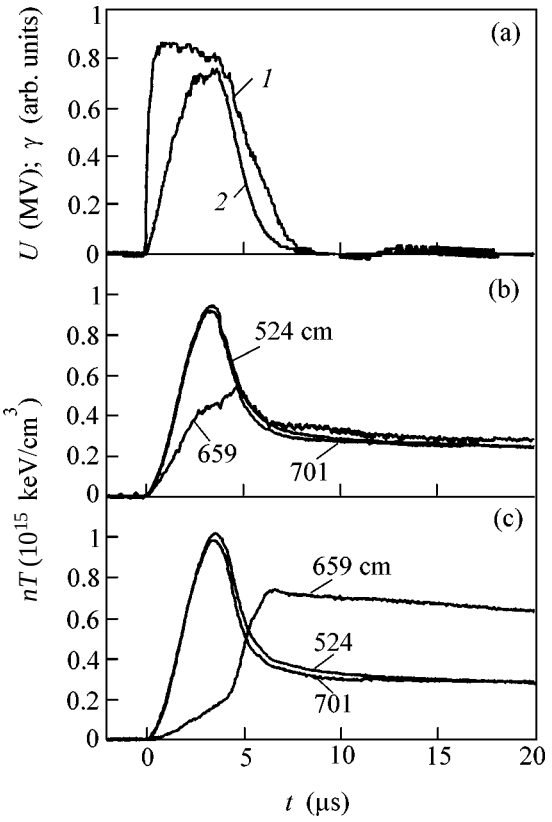

Fig. 1. (a) Dependence of U on t. (*1*) Diode voltage and (*2*) bremsstrahlung radiation from the exit collector; (b) and (c) plasma pressure measured near the reduced-field section (numbers near the curves correspond to the longitudinal coordinates of the coils): (b) B = 3.8 T in the central section with the center at 659 cm and (c) B = 1.3 T at the same site.

We first consider the case with the completely switched-on solenoid (Fig. 1b). After the beam injection, the plasma pressure increases until the injected beam power starts to decrease. As pointed out above, plasma electrons are heated in the course of beam injection because of the collective effects that are mainly due to the excitation of Langmuir oscillations. The excess of beam instability increment over the effective electron-collision frequency in plasma is the necessary condition for the efficient beam relaxation. This condition signifies that, for a given plasma density, the beam current density must exceed a certain critical value. In the GOL-3 experiments, the maximal plasma density for which electrons are efficiently heated is equal to about 2×10^{15} cm^{-3} for the beam current density on the scale of 1 kA/cm^2.

As in [1, 2], the heating in our experiments was highly nonuniform along the device length, especially at few starting meters; however, the signal shapes of the diamagnetic coils were similar to the one shown in Fig. 1b for the Z = 701 cm coil. The signal amplitude of this diamagnetic coil corresponds to the cross-sectional

average value $D = n_eT_e + n_iT_i \sim 10^{15}$ keV/cm^3 of the plasma column (here, n and T are the concentration and temperature, respectively, and e and i refer, respectively, to electrons and ions). In the central section of the device, the pressure longitudinal gradient in plasma is already low, and the signals of five diamagnetic coils placed in a uniform magnetic field from $Z = 475$ cm to $Z = 844$ cm coincide with each other to within 5% at the plasma heating stage. The coil signal shape at $Z = 659$ cm in a field of 3.8 T is slightly different from the others (Fig. 1b). Plasma is heated slowly at this point, because the ratio of electron-beam density to the plasma electron density (which, all things being the same, determines the beam relaxation efficiency in plasma; see, e.g., [11]) is reduced due to the expansion of the magnetic-field tube in this region. After the termination of heating, plasma is rapidly cooled, the temperature levels off along the length, and the reading of the $Z = 659$ cm coil becomes close to the readings of the neighboring coils.

A different behavior of plasma pressure in the central section is observed if the field in the magnetic pit is weak after switching off the adjacent solenoid coils (Fig. 1c). On the whole, the character of plasma heating in this case does not change over most of the solenoid, and the plasma pressure distribution along the device length is also unchanged. However, substantial changes in the pressure dynamics are detected by the coil at $Z = 659$ cm. The magnetic field in the central section decreases to ~1.3 T, and the beam-current density becomes 3.7 times lower than in the region of uniform field, so that the beam practically does not interact with plasma at this site. As a result, the plasma pressure, being determined by the electron temperature in the course of beam injection, is 5 to 10 times lower in the low-field section than the pressure detected by the coils at a distance of ~40 cm in the region of uniform field. It is important that, due to the suppression of the longitudinal electron heat conductivity (see Introduction), the energy transfer to the region of magnetic-field minimum from the neighboring regions of hot plasma is almost zero. A high electron-temperature gradient along the length (up to 2.5 keV/m) exists during the heating stage and characterizes the degree of suppression of electron heat conductivity over this time. After the termination of heating, the effect of anomalously low heat conductivity disappears, the effective collision frequency in plasma becomes classical, and the temperature along the plasma-column length starts to rapidly level off. At this instant of time, plasma pressure in the magnetic pit rises drastically (although it drops in the remaining regions of the device), and β in the magnetic pit reaches a value of 15–20%.

Yet another two circumstances are noteworthy. First, the plasma pressure in this region of central section slightly increases immediately also after heating in a high magnetic field (Fig. 1b). Second, preliminary hydrodynamic calculations using the modified ISW code (its first version was used in [4]) show that, due to the appearance of a longitudinal pressure gradient near the magnetic pit at the heating stage, plasma is "accumulated" in this region even during the beam pulse. Due to the energy thermalization of these counterpropagating plasma flows, the plasma pressure in the magnetic-pit region may be higher (for a while) than in the regions adjacent to the trap.

4. Conclusions. A short section with a magnetic field of 1.3 T (i.e., 3.7 times lower than in the adjacent regions with a uniform magnetic field) has been formed in a middle of the solenoid of the GOL-3 device. Due to a decrease in the local electron density of a relativistic beam in this section, beam-induced plasma heating almost did not occur in the weak-field region. As a result, a short region with a temperature several times lower than in the surrounding plasma was formed during the course of beam injection into the initially homogeneous plasma. The measured longitudinal plasma pressure gradient corresponded to an electron temperature gradient of ~1 keV/40 cm (for the above-mentioned parameters of beam-induced plasma heating and characteristic time of few microseconds, the ion temperature is much lower than the electron temperature [1]). The existence of a low-temperature region is direct evidence of the suppression of longitudinal electron heat conductivity at the stage of collective beam–plasma interaction and plasma heating. After heating, the heat conductivity regains its classical value (for details, see [3, 4]), which is manifested by a rapid increase in plasma pressure in the weak-field section and simultaneous plasma cooling in the remaining part of the device.

We are grateful to R.Yu. Akent'ev, V.G. Ivanenko, V.V. Konyukhov, S.A. Kuznetsov, A.G. Makarov, S.S. Perin, Yu.S. Sulyaev, V.D. Stepanov, and A.A. Shoshin for assistance in preparing and conducting experiments on the GOL-3 device and I.A. Kotel'nikov for helpful discussions. This work was supported by the Ministry of Science of the Russian Federation and the Russian Foundation for Basic Research, project no. 00-02-17649.

REFERENCES

1. A. V. Burdakov, S. G. Voropaev, V. S. Koĭdan, *et al.*, Zh. Éksp. Teor. Fiz. **109**, 2078 (1996) [JETP **82**, 1120 (1996)].
2. A. V. Arzhannikov, V. T. Astrelin, A. V. Burdakov, *et al.*, Trans. Fusion Technol. **39** (1T), 17 (2001).
3. A. V. Burdakov and V. V. Postupaev, Preprint No. 92-9, IYaF SO RAN (Inst. of Nuclear Physics, Siberian Division, Russian Academy of Sciences, Novosibirsk, 1992).
4. V. T. Astrelin, A. V. Burdakov, and V. V. Postupaev, Fiz. Plazmy (Moscow) **24**, 450 (1998) [Plasma Phys. Rep. **24**, 414 (1998)].

5. A. V. Arzhannikov, A. V. Burdakov, V. S. Koidan, and L. N. Vyacheslavov, Phys. Scr. T **2/2** (1), 303 (1982).
6. M. V. Babykin, P. P. Gavrin, E. K. Zavoĭskiĭ, *et al.*, Zh. Éksp. Teor. Fiz. **52**, 643 (1967) [Sov. Phys. JETP **25**, 421 (1967)].
7. A. A. Galeev and R. Z. Sagdeev, in *Basic Plasma Physics*, Ed. by A. A. Galeev and R. N. Sudan (Énergoatomizdat, Moscow, 1984; North-Holland, Amsterdam, 1984), Vol. 2 (Suppl.).
8. R. N. Sudan, in *Basic Plasma Physics*, Ed. by A. A. Galeev and R. N. Sudan (Énergoatomizdat, Moscow, 1984; North-Holland, Amsterdam, 1984), Vol. 2 (Suppl.).
9. V. S. Burmasov, L. N. Vyacheslavov, I. V. Kandaurov, *et al.*, Fiz. Plazmy (Moscow) **23**, 142 (1997) [Plasma Phys. Rep. **23**, 126 (1997)].
10. V. S. Burmasov, V. F. Gurko, I. V. Kandaurov, *et al.*, in *Abstracts of 28th EPS Conference on Controlled Fusion and Plasma Physics* (Madeira, Portugal, 2001), p. 521.
11. B. N. Breizman and D. D. Ryutov, Nucl. Fusion **14**, 873 (1974).

Translated by V. Sakun

JETP Letters, Vol. 77, No. 7, 2003, pp. 362–365. Translated from Pis'ma v Zhurnal Éksperimental'noĭ i Teoreticheskoĭ Fiziki, Vol. 77, No. 7, 2003, pp. 430–433.

Subthreshold Sputtering at High Temperatures

M. I. Guseva, V. M. Gureev, B. N. Kolbasov, S. N. Korshunov, Yu. V. Martynenko, V. B. Petrov, and B. I. Khripunov

Russian Research Centre Kurchatov Institute, pl. Kurchatova 1, Moscow, 123182 Russia

Received February 25, 2003

Abstract—The sputtering of tungsten from a target at a temperature of 1470 K during irradiation by 5-eV deuterium ions in a steady-state dense plasma is discovered. The literature values of the threshold for the sputtering of tungsten by deuterium ions are 160–200 eV. The tungsten sputtering coefficient measured by the loss of weight is found to be 1.5×10^{-4} atom/ion at a deuterium ion energy of 5 eV. Previously, such a sputtering coefficient was usually observed at energies of 250 eV. The sputtering is accompanied by a change in the target surface relief, i.e., by the etching of the grain boundaries and the formation of a wavy structure on the tungsten surface. The subthreshold sputtering at a high temperature is explained by the possible sputtering of adsorbed tungsten atoms that are released from the traps around the interstitial atoms and come to the target surface from the space between the grains. The wavy structure on the surface results from the merging of adsorbed atoms into ordered clusters. © *2003 MAIK "Nauka/Interperiodica".*

PACS numbers: 52.55.Rk; 61.80.Jh; 81.15.Cd

INTRODUCTION

The sputtering of materials by fast ions is a phenomenon that has been studied fairly well and whose major features seem to be well established. Thus, it is well known that, at ion energies below a certain threshold energy E_{tr}, there is no sputtering [1]. Since the sputtering results from binary elastic collisions between the ions and the atoms of the target, the existence of the threshold is a consequence of the condition that the maximum energy that the ion can transfer to the target atom in a collision,

$$\Delta E_{\max} = E\lambda, \quad \lambda = 4M_iM_a/(M_i + M_a)^2,$$

is higher than the binding energy of the target atoms to the target surface (the sublimation energy U). For light ions and target materials with high atomic numbers, the sputtering threshold is especially high. The theoretical threshold energy for the sputtering of tungsten (U = 8.7 eV) by deuterium ions is equal to 201 eV, while experimental measurements yielded thresholds of 178 eV [2] and 160 eV [3]. In this work, we have detected the sputtering of tungsten from a target at a temperature of 1470 K during irradiation by 5-eV deuterium ions in a steady-state dense plasma.

The phenomenon observed is important not only from the standpoint of general physics but also from the point of view of practical applications in which low-energy ions interact with a material at a high temperature. Thus, in the International Thermonuclear Experimental Reactor (ITER), it is proposed to utilize a tungsten divertor capable of operating at high temperatures [3]. The tungsten components of the divertor are expected to undergo erosion only during plasma disruptions [3], because the energy threshold for the physical sputtering of tungsten is high. In the concept of a gas divertor that was developed in [4] in order to reduce the divertor erosion, a tungsten divertor is exposed to a dense plasma with a temperature of several electronvolts. In the context of the above problems, we have carried out experiments aimed at modeling the operation of a gas divertor for ITER by investigating the sputtering of tungsten from a target at temperatures of 1200 to 1470 K during the irradiation by 5-eV deuterium ions in a steady-state dense plasma in the LENTA device.

The phenomena revealed in our experiments are also important for the problem of the passage of space objects through the Earth's atmosphere. Under atmospheric conditions, the relative kinetic energy of the gas atoms and molecules is several electronvolts, and the surface of the space object is heated to a high temperature. From a practical standpoint, the most interesting phenomena are the etching of the grain boundaries and the possible accompanying changes in the mechanical properties of the grain material.

EXPERIMENT

Our experiments on modeling a gas divertor in the LENTA device were carried out with tungsten samples in a deuterium plasma under beam–plasma discharge conditions in a longitudinal magnetic field (see Fig. 1) [5]. The experiment is organized as follows. In the discharge zone of the device, an electron beam generates a steady-state plasma flow (a beam–plasma discharge) with an electron density of 10^{12}–10^{13} cm^{-3} and electron temperature of 5–20 eV. The plasma flows along the magnetic field and enters the adjacent region—the interaction zone (or the "gas target"), which is fed with

0021-3640/03/7707-0362$24.00

neutral gas at a pressure of up to 10 mtorr. As the plasma interacts with the gas, its parameters change considerably. In the interaction process, the energy of the initial plasma flow is dissipated; in particular, the electron temperature decreases substantially (to 0.5–1.5 eV), as is the case in the divertor of a tokamak operating with gas injection (the phenomenon of "plasma detachment") [4]. As a result, the energy content of the plasma that comes to the surface of the cooled collector plate (Fig. 1) is reduced. Tungsten samples (W + 0.04% Mo) are placed at and near the collector plate surface and are oriented along and across the magnetic field. The temperature of the irradiated surface of the samples is determined by the energy of the incident plasma flow. The sample temperature, which is controlled by thermocouples and an optical pyrometer, changes from 1200 to 1470 eV. In our experiments, the energy of the ions bombarding the tungsten surface corresponds to the potential jump across the wall sheath and is about 5 eV (in which case the electron temperature in the deuterium plasma is about $T_e \sim 1.5$ eV). The plasma flow density is determined from the density of the ion saturation current measured by Langmuir probes near the target surface and also from direct measurements of the ion current to the samples. The ion flow density is maintained at a level of $(1–5) \times 10^{21}$ m^{-2} s^{-1}, and the irradiation dose is about 5×10^{25}–10^{26} m^{-2}, which corresponds to the dose that is expected to be accumulated by the divertor plate surface in ITER during one cycle of normal operation.

Before irradiation, the tungsten samples were polished both mechanically and electrolytically. Also, the samples were weighted before and after irradiation. The sputtering coefficient, which was defined as the average number of target atoms sputtered by one ion, was determined from the loss of weight and the accumulated dose.

The microstructure of the tungsten surfaces was investigated using a scanning electron microscope. The surface of a polished sample is shown in Fig. 2.

The tungsten sputtering coefficient measured by determining the loss of weight at a deuterium ion energy of 5 eV and a tungsten temperature of 1470 K was found to be $(1–1.5) \times 10^{-4}$ atom/ion. It should be noted that these values of the tungsten sputtering coefficient are characteristic of 250-eV D^+ ions. This new result is quite unexpected.

As tungsten is sputtered, its surface structure changes. Figure 3 presents the microstructure of the tungsten surface after irradiation at a temperature of 1470 K by a flow of 5-eV D^+ ions in a steady-state deuterium plasma. The topography of the irradiated surface shows that it has been deeply eroded. The plasma etches the surfaces of the grains, making the grains and their orientation apparent. The tungsten surface becomes wavy; the waves originate and propagate from the grain boundaries.

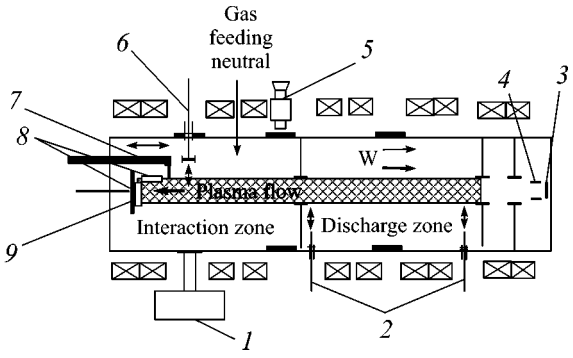

Fig. 1. Schematic of the experiment on modeling a gas divertor by irradiating tungsten samples in the LENTA device: (*1*) mass spectrometer, (*2*) Langmuir probes, (*3*) cathode, (*4*) anode, (*5*) optical monochromator, (*6*) Mach region, (*7*) movable calorimeter, (*8*) samples, and (*9*) collector plate.

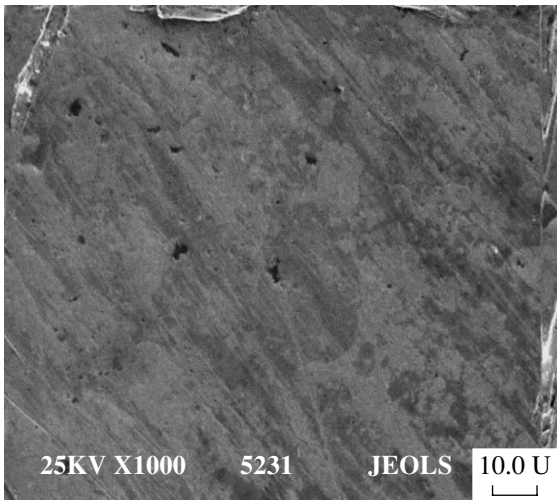

Fig. 2. Microstructure of an electrolytically polished tungsten surface.

In our experiments, tungsten samples were also irradiated in a plasma at lower temperatures, all other conditions being the same. At temperatures below 1250 K, no tungsten sputtering was detected. The microstructure of the tungsten surface irradiated at temperatures of 1210–1250 K is shown in Fig. 4, in which the etching of tungsten is not observed. Consequently, the effect of etching of a tungsten surface by low-energy deuterium ions also has a threshold in terms of the temperature.

THEORETICAL MODEL

The most natural assumption is that, at low (subthreshold) ion energies, the only atoms that can be sputtered are weakly bonded atoms that are adsorbed on the surface and whose binding energy to the surface is

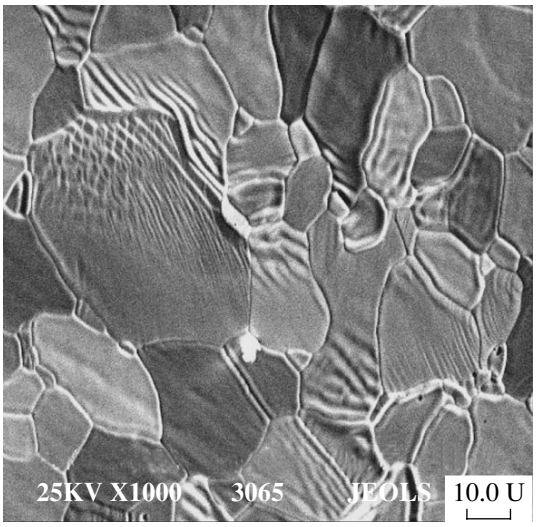

Fig. 3. Microstructure of a tungsten surface after irradiation at a temperature of 1470 K in a steady-state plasma by a flow of deuterium ions with the energy $E = 5$ eV and the current density $J = (1–5) \times 10^{21}$ m^{-2} s^{-1}, the irradiation dose being 10^{26} m^{-2}.

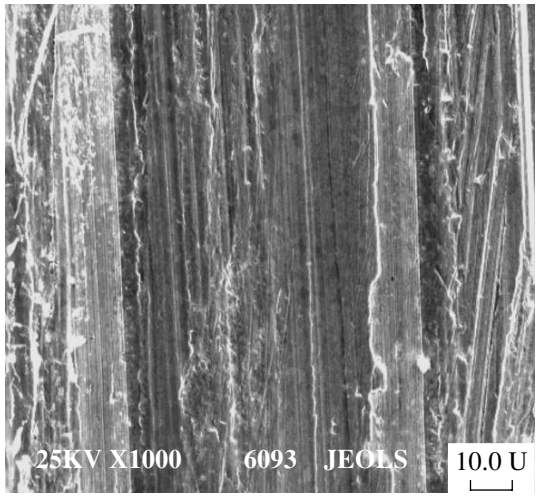

Fig. 4. Microstructure of a tungsten surface after irradiation at temperatures of 1210–1250 K in a steady-state plasma by a flow of deuterium ions with the energy $E = 5$ eV and the current density $J = (1–5) \times 10^{21}$ m^{-2} s^{-1}, the irradiation dose being 10^{26} m^{-2}.

about $\varphi \approx 0.4U$. The coupling between the adsorbed ions that merge into clusters, as well as their binding to the surface, is stronger. Therefore, the sputtering of clusters can be neglected.

At the same time, the energy transferred from a deuterium ion with the energy $E = 5$ eV to a tungsten ion can be significantly lower than the binding energy of an adsorbed tungsten atom to the surface,

$$\Delta E = \lambda E \approx 0.215 \text{ eV} \ll \varphi = 3.4 \text{ eV}.$$

This indicates that, at such energies, the elastic sputtering of the adsorbed atoms is also impossible.

However, the weak coupling of an adsorbed atom to the atoms of the metal also indicates that its energy levels are narrower than the zone in the metal. This makes possible the sputtering of adsorbed atoms by slow ions. The mechanism for this sputtering is as follows. The field of an incident ion excites an electron of an adsorbed atom from the ground state to a repulsing term. Physically, an incident ion attracts an electron and causes it to move from a position between an adsorbed atom and a metal (in this position, the electron binds the adsorbed atom to the metal) to a position above the adsorbed atom. This possible mechanism, which is an analogue of the mechanism for the desorption of impurity atoms from metal surfaces, acts as if the binding of an adsorbed atom to the surface were eliminated by the electron excitation. In terms of the cross section σ for this process (estimates show that $\sigma \approx 10^{-15}$ cm^2) and the density n of adsorbed atoms at the surface, the sputtering coefficient is equal to

$$Y = \sigma n.$$

In thermodynamic equilibrium, the density of adsorbed atoms at the surface is very low:

$$n = a^{-2} \exp[-(U - \varphi)/kT] \approx 10^{-3} \text{ cm}^{-2}.$$

However, at high temperatures, adsorbed atoms can come from the boundaries of the grains; i.e., interstitial atoms can move from the grain boundaries to the surface and can become adsorbed atoms. This is evidenced by the etching of the grain boundaries.

The boundaries of the grains, which are usually far from being perfect crystals, are composed of chaotically arranged atoms, which, however, are trapped at the boundary or, in other words, are in bound states. As the temperature increases, these atoms are detrapped and start to migrate along the boundary of the grain. The grain boundaries are etched as a result of escape of the interstitial atoms from the intergrain space either at a high temperature or under ion irradiation.

The number of interstitial atoms that escape from a unit area of the grain boundary to the surface per unit time as a result of thermal excitation is equal to $q = Cd/\tau$, where C is the density of interstitial atoms in the space between the grains (this density is assumed to be constant over the entire intergrain space because of the high mobility of the interstitial atoms), d is the width of the intergrain space, $\tau = \nu^{-1} \exp(-E_a/T)$ is the time during which an interstitial atom escapes from the intergrain space to the surface as a result of thermal excitation, ν is the oscillation frequency of the atoms, and $E_a \approx 1$ eV is the activation energy (this energy is set equal to the Peierls potential [6] for the motion of an atom along a dislocation. In this case, the number Q of

adsorbed atoms that come to a unit area of the surface per unit time is equal to

$$Q = q/r = (C/\tau)(d/r),$$

where r is the size of the grains.

The adsorbed atoms are either sputtered with probability $j\sigma_s$ or merge with probability αDn^2 to form the grain structures on the surface. Here, the cross section σ_s for the sputtering of adsorbed atoms by an incident ion is estimated to be $(1/3–1) \times 10^{-15}$ cm^2; $D \approx 10^{-6}$ cm^2/s is the coefficient of diffusion of adsorbed atoms along the surface [7, 8]; and $\alpha = 4\pi R/a$, where R is the distance within which an adsorbed atom is trapped at the surface by another adsorbed atom and a is the atomic size. Since $\alpha Dn^2 \gg j\sigma_s n$, we have $C = (Q/\alpha D)^{1/2}$. Estimates show that the density C can be as high as about $\sim 10^{12}$ cm^{-2}. In this case, the sputtering coefficient is equal to $Y = \sigma_s C \approx (1/3–1) \times 10^{-3}$, which satisfactorily explains the experimentally measured values of this coefficient.

The formation of wavy structures near the grain boundaries can be attributed to the merging of individual adsorbed atoms into extended clusters, which are stretched along the direction of diffusion of the adsorbed atoms from the boundary of the grain. This mechanism for the formation of clusters is analogous to that for the formation of a porous lattice during the vacancy expansion, the only difference being that, in our case, the two-dimensional geometry and the directed diffusive flow of the adsorbed atoms lead to the formation of clusters stretched along the flow direction. The wavelength of the wavy structures is on the order of the diffusion length of the adsorbed atoms over a period of time t_1 during which they are trapped in the wave; i.e., we have $\lambda \approx (Dt_1)^{1/2}$. Setting $t_1 = \nu^{-1}\exp(E_t/kT)$, where $\nu \approx 10^{13}$ s^{-1} is the oscillation frequency of the atom and $E_t \approx 0.4U = 3.5$ eV is its binding energy at the wave crest, we obtain $\lambda \approx 1$ μm.

It should be emphasized that, in the model proposed here, the effects of subthreshold sputtering and a change in the surface structure are possible only for polycrystals. Monocrystals do not possess a grain structure and do not have sufficiently intense sources of adsorbed atoms. According to the model, the sputtering coefficient increases with decreasing grain size, $Y \sim r^{-1/2}$. The way the polycrystalline material is obtained can affect the density of interstitial atoms in the space between the grains and, consequently, the value of the sputtering coefficient.

CONCLUSIONS

(i) We have discovered the phenomenon of the sputtering of tungsten from a target at a temperature of 1470 K during the irradiation by 5-eV deuterium ions in a steady-state dense plasma. The known threshold for tungsten sputtering by deuterium ions is 160 eV. For 5-eV deuterium ions, the tungsten sputtering coefficient is equal to 1.5×10^{-4} atom/ion.

(ii) The sputtering is accompanied by the following two processes: the etching of the grain boundaries and the formation of a wavy structure on the tungsten surface. The waves originate and propagate from the grain boundaries.

(iii) The subthreshold sputtering at a high temperature is explained by the possible sputtering of adsorbed tungsten atoms that are released from the traps around the interstitial atoms and come to the target surface from the space between the grains. The wavy structure on the surface results from the merging of adsorbed atoms into ordered clusters.

REFERENCES

1. *Sputtering by Particle Bombardment*, Ed. by R. Behrisch (Springer, Berlin, 1981; Mir, Moscow, 1984).
2. J. W. Davis, V. R. Barabash, V. R. Makhankov, *et al.*, J. Nucl. Mater. **258–263**, 308 (1998).
3. M. I. Guseva, A. L. Suvorov, S. N. Korshunov, and N. E. Lazarev, J. Nucl. Mater. **266–269**, 222 (1999).
4. Nucl. Fusion **39**, 2391 (1999).
5. N. V. Antonov, B. I. Khripunov, V. B. Petrov, *et al.*, J. Nucl. Mater. **220–222**, 943 (1995).
6. T. Suzuki, H. Yosinaga, and S. Takeucti, *Dislocation Dynamics and Plasticity* (Syokabo, Tokyo, 1986; Mir, Moscow, 1989), Chap. 4.
7. A. N. Orlov and Yu. V. Trushin, *Energy of Point Defects in Metals* (Énergoatomizdat, Moscow, 1983).
8. V. P. Zhdanov, *Elementary Physicochemical Processes on Surface* (Nauka, Novosibirsk, 1988).

Translated by G. Shepekina

JETP Letters, Vol. 77, No. 7, 2003, pp. 366–370. Translated from Pis'ma v Zhurnal Éksperimental'noĭ i Teoreticheskoĭ Fiziki, Vol. 77, No. 7, 2003, pp. 434–438.

Dynamically Induced Kondo Effect in Double Quantum Dots

M. N. Kiselev[1, *], K. A. Kikoin[2], and L. W. Molenkamp[3]

[1] *Institut für Theoretische Physik und Astrophysik, Universität Würzburg, D-97074 Wärzburg, Germany*
**e-mail: kiselev@physik.uni-wuerzburg.de*
[2] *Ben-Gurion University of the Negev, Beer-Sheva 84105, Israel*
[3] *Physikalisches Institut (EP-3), Universität Wärzburg, D-97074 Wärzburg, Germany*

Received February 18, 2003

A new mechanism of resonance Kondo tunneling via a composite quantum dot (QD) is proposed. It is shown that, owing to the hidden dynamic spin symmetry, the Kondo effect can be induced by a finite voltage eV applied to the contacts at an even number N of electrons in a QD with zero spin in the ground state. As an example, a double QD is considered in a parallel geometry with $N = 2$, which possesses the SO(4) type symmetry characteristic of a singlet–triplet pair. In this system, the Kondo peak of conductance appears at an eV value compensating for the exchange splitting. © *2003 MAIK "Nauka/Interperiodica".*

PACS numbers: 72.10.Fk; 72.15.Qm; 73.63.Kv

The Kondo effect, originally observed in the form of an anomalously strong resonance scattering of electrons by magnetic impurities in metals, has proved to be a universal mechanism of interaction between an electron gas and localized quantum objects possessing internal degrees of freedom [1]. In particular, a magnetic impurity within the barrier between two metal contacts, as well as a quantum dot (QD) with uncompensated spin occurring in a tunneling junction between metal electrodes, can account for anomalously high tunneling transparency of the barrier for electrons from the contacts [2, 3]. Shortly after the experimental discovery of such Kondo resonances in the tunneling via planar QDs [4], it was established that the spectrum of phenomena related to the effective magnetic exchange in QDs is by no means restricted to simple passage from the problem of Kondo scattering to that of Kondo transfer. In particular, it was found that the resonance Kondo tunneling via QDs with an even number of electrons and zero total spin is possible under the action of an external magnetic field [5] or the electric field of a gate [6].

The large variety of manifestations of the Kondo effect in QDs is related to the fact that these nanodimensional objects are essentially a kind of artificial atom possessing complicated spectra. The tunneling of electrons from outside via QDs breaks their spin symmetry and induces transitions to low-lying excited states. The transitions at energies comparable with the Kondo temperature (T_K) are involved into resonance interactions and modify the pattern of the Kondo scaling as compared to that typical of the canonical Kondo effect in metals. Thus, within the limits of the Kondo energy scale, it is necessary to take into account the dynamic symmetry of a given QD [7]. This symmetry is determined both by the spin and by other vectors involved in the algebra of the corresponding dynamic group. As a result, the effective Hamiltonian describing the Kondo tunneling acquires a more complicated form than that of the *sd*-exchange Hamiltonian describing the Kondo effect in metals: all the above vectors contribute to the cotunneling with spin reversal via the QD. A theory of the dynamic symmetry of composite (double and triple) QDs has been recently developed in [8], where it is also demonstrated how an external magnetic field or the gate electric field can influence the dynamic symmetry.

Below, we consider a new class of phenomena related to the dynamic symmetry of QDs. It will be demonstrated that violation of the thermodynamic equilibrium between contacts may induce resonance Kondo tunneling not observed in the equilibrium system. The nonequilibrium Kondo effect in QDs at a finite voltage applied between the source and sink has been extensively studied (see, e.g., [9]). In most cases, however, researchers were interested in the influence of nonequilibrium conditions on the Kondo effect existing in the equilibrium state. In such a situation, relaxation of the system related to the finite lifetime of excited states probably hinders attaining a strong coupling regime (see, e.g., the discussion in [10, 11]).

We are interested in a different situation, whereby no channel of nonequilibrium induced spin relaxation exists in the ground state (e.g., for $S = 0$). In this case, the spin degrees of freedom are excited only in QDs possessing a dynamic symmetry. Such a symmetry is inherent, for example, in a double quantum dot (DQD) structure experimentally realized and studied recently [12]. In the simplest nontrivial case, the DQD contains two electrons occupying energy levels according to the Heitler–London scheme (Fig. 1). The system occurs under the conditions of a strong Coulomb blockade Q

suppressing the tunneling v between potential wells. The spectrum of spin states represents a singlet–triplet (S–T) pair with zero spin in the ground state (because the effective exchange between the two valleys, $I \approx v^2/Q$, has an antiferromagnetic character). As demonstrated previously [6, 8], an isolated DQD represents a quantum spin rotator with the $SO(4)$ symmetry, in contrast to the $SU(2)$ symmetry of a QD with odd occupation usually considered in the theory of the Kondo type tunneling. The $SO(4)$ group is generated by the spin vector **S** and the vector **P** describing the S–T transition matrix.

The Hamiltonian of an isolated QD can be written as

$$H_d = E_S|S\rangle\langle S| + \sum_{\eta} E_T|T\eta\rangle\langle T\eta|, \qquad (1)$$

where $E_T = E_S + \delta$; $\eta = \pm, 0$ are the projections of the spin total $S = 1$; and $\delta = I$ is the exchange coupling. Since the direct tunneling W of electrons from contacts to the DQD is suppressed by the Coulomb blockade Q, the charge transfer is possible only by means of second-order processes (cotunneling). The effective Hamiltonian describing these processes is as follows [6, 8]:

$$H_{\rm int} = J\sum_{\alpha\alpha'}(\mathbf{S} + \mathbf{P})\mathbf{s}_{\alpha\alpha'},$$
$$\mathbf{s}_{\alpha\alpha'} = \sum_{kk'} c^{\dagger}_{k\alpha\sigma}\hat{\tau}c_{k'\alpha'\sigma'}, \quad n_{\alpha\alpha'} = \sum_{kk'} c^{\dagger}_{k\alpha\sigma}\hat{1}c_{k'\alpha'\sigma}, \qquad (2)$$

where the subscript $\alpha = L, R$ denotes electrons in the left- and right-hand contacts, respectively; $\hat{\tau}$ are the Pauli matrices; $\hat{1}$ is the unit matrix; and $J \approx W^2/(\epsilon_F - E_S/2)$is the effective constant of exchange between the DQD and contacts (we neglect a difference between tunneling parameters in the S and T states of the QD). The **S** and **P** vectors defined above are written in matrix form as follows:

$$S^+ = \sqrt{2}\begin{pmatrix} 0&1&0&0\\ 0&0&1&0\\ 0&0&0&0\\ 0&0&0&0\end{pmatrix}, \quad S^z = \begin{pmatrix} 1&0&0&0\\ 0&0&0&0\\ 0&0&-1&0\\ 0&0&0&0\end{pmatrix},$$

$$P^+ = \sqrt{2}\begin{pmatrix} 0&0&0&1\\ 0&0&0&0\\ 0&0&0&0\\ 0&0&-1&0\end{pmatrix}, \quad P^z = -\begin{pmatrix} 0&0&0&0\\ 0&0&0&1\\ 0&0&0&0\\ 0&1&0&0\end{pmatrix},$$

where a singlet state corresponds to the last row. The corresponding algebra (o_4) is described by the commutations relations

$$[S_j, S_k] = ie_{jkl}S_l, \quad [P_j, P_k] = ie_{jkl}S_l,$$
$$[P_j, S_k] = ie_{jkl}P_l,$$

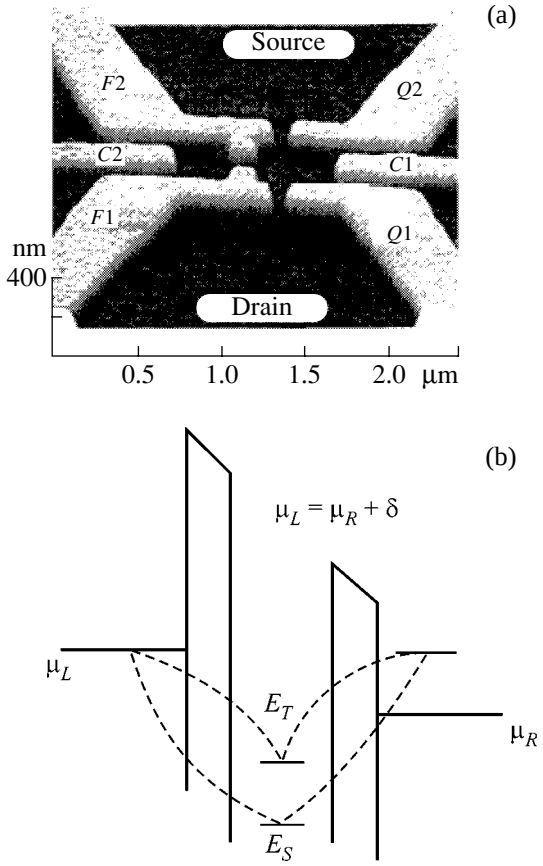

Fig. 1. (a) A parallel double quantum dot configuration (Hofmann *et al.* [12]) and (b) an energy band diagram illustrating tunneling and cotunneling processes contributing to the differential conductance in this system.

where j, k, l are the coordinate indices and e_{jkl} is the Levi–Civita tensor.

As can be seen, both **S** and **P** vectors are involved in the tunneling with spin reversal. However, since the threshold energy for excitation of the spin degrees of freedom is δ, the spin scattering under equilibrium conditions is effective only provided that $T_K > \delta$. It will be shown below that this threshold can also be surmounted in the opposite limit, $T_K \ll \delta$, at a finite source–sink voltage $eV \approx \delta$ compensating for the S–T splitting energy. In the weak coupling regime, $T > T_K$, we use the thermodynamic perturbation theory and assume that electrons in the contacts obey the Fermi statistics with the chemical potentials μ_R and $\mu_R + eV$ in the right- and left-hand contacts, respectively. We can also assume that weak tunneling currents do not violate thermodynamic quasi-equilibrium (the validity of this approach is discussed below).

In order to construct the perturbation theory, let us perform fermionization of the generators of $SO(4)$

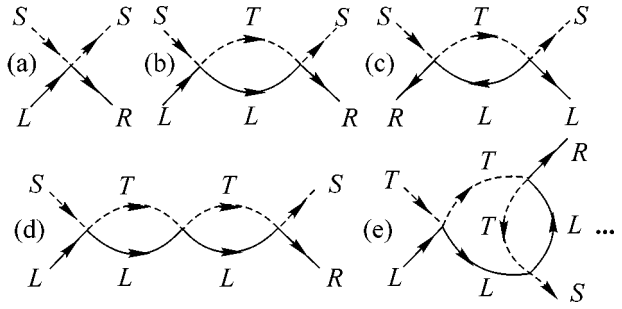

Fig. 2. Perturbation theory diagrams determining (a) J, (b, d) the main corrections to J, and (c, e) corrections containing a lower power of the logarithm. Solid curves refer to electron between contacts; dashed curves refer to the QD states.

group—a generalizing procedure originally suggested for $SU(2)$ group [13, 14]:

$$S^+ = \sqrt{2}(f_0^\dagger f_{-1} + f_1^\dagger f_0), \quad S^- = \sqrt{2}(f_{-1}^\dagger f_0 + f_0^\dagger f_1),$$
$$P^+ = \sqrt{2}(f_1^\dagger f_s - f_s^\dagger f_{-1}), \quad P^- = \sqrt{2}(f_s^\dagger f_1 - f_{-1}^\dagger f_s),$$
$$S_z = f_1^\dagger f_1 - f_{-1}^\dagger f_{-1}, \quad P^z = -(f_0^\dagger f_s + f_s^\dagger f_0). \quad (3)$$

Here, $f_{\pm 1}^\dagger$ are the operators of creation for fermions with the spin projections 1 and –1; f_0^+ and f_s are the operators of creation for zero-spin fermions in the triplet and singlet states, respectively. Representation (3) automatically takes into account the local kinematic constraint $\sum_\Lambda f_\Lambda^\dagger f_\Lambda = 1$. A diagram technique of the perturbation theory is provided by the temperature Green's functions for electrons between contacts, $G_{L,R}(\mathbf{k}, \tau) = -\langle T_\tau c_{L,R\sigma}(k, \tau) c_{L,R\sigma}^\dagger(k, 0)\rangle$, and for fermions in the DQD, $\mathcal{G}_\Lambda(\tau) = -\langle T_\tau f_\Lambda(\tau) f_\Lambda^\dagger(0)\rangle$. The Fourier transform in imaginary time yields

$$G_{k\alpha}^0(\epsilon_n) = (i\epsilon_n - \epsilon_{k\alpha} + \mu_{L,R})^{-1},$$
$$\mathcal{G}_\eta^0(\omega_m) = (i\omega_m - E_T)^{-1}, \quad \eta = -1, 0, 1, \quad (4)$$
$$\mathcal{G}_s^0(\epsilon_n) = (i\epsilon_n - E_S)^{-1},$$

where $\epsilon_n = 2\pi T(n + 1/2)$, $\omega_m = 2\pi T(m + 1/3)$ [13, 14].

Figure 2 shows the main diagrams of the perturbation theory. The first diagrams (Figs. 2b and 2c) determining the Kondo tiling in a standard theory give the following expressions for the renormalized exchange vertices:

$$\Gamma_{LR}^{(2b)}(\omega) \sim J^2 \sum_{\mathbf{k}} \frac{1 - f(\epsilon_{kL} - eV)}{\omega - \epsilon_{kL} + \mu_L - \delta},$$
$$\Gamma_{LR}^{(2c)}(\omega) \sim J^2 \sum_{\mathbf{k}} \frac{f(\epsilon_{kL} - eV)}{\omega - \epsilon_{kL} + \mu_L + \delta}. \quad (5)$$

Replacing ϵ_{kL} by $\epsilon_{kL} - eV$ at the vertex (Fig. 2b), we obtain

$$\Gamma_{LR}^{(2b)}(\omega) \sim J^2 \nu \ln(D/\max\{\omega, (eV - \delta), T\}).$$

where $D \sim \varepsilon_F$ is the truncation parameter determining the effective width of continuum between contacts, ν is the density of states on the Fermi level, and $f(\varepsilon)$ is the Fermi function. As can be seen, a bias compensating for the exchange splitting $|eV - \delta| \ll \max[eV, \delta]$ gives rise to a logarithmic singularity (typical of the Kondo effect) independent of eV. In the second vertex correction (Fig. 2c), the compensation is absent and the corresponding contribution for $eV \sim \delta \gg T$, ω can be estimated as

$$\Gamma_{LR}^{(2c)}(\omega) \sim J^2 \nu \ln(D/(eV + \delta)) \ll \Gamma_{LR}^{(2b)}(\omega).$$

Analogous estimates for the diagrams in Figs. 2d and 2e give

$$\Gamma_{LR}^{(2d)}(\omega) \sim J^3 \nu^2 \ln^2(D/\max\{\omega, (eV - \delta), T\}),$$
$$\Gamma_{LR}^{(2e)}(\omega) \sim J^3 \nu^2 \ln(D/\max\{\omega, (eV - \delta), T\}) \quad (6)$$
$$\times \ln(D/\max\{\omega, eV, T\}).$$

Only the first of these contributions survives in the main logarithmic approximation. Thus, a logarithmic singularity in the tunneling amplitude is actually restored by applying an electric field to a DQD with zero spin in the ground state, whereby a sequence of divergent tiling diagrams degenerates into the sequence of ladder diagrams.

The perturbation theory diagrams at $T > T_K$ can be summed using the renorm group method, which is applicable under both equilibrium and nonequilibrium conditions [15]. The set of renorm group equations for the tunneling vertices $J_{\alpha\alpha'}^{\Lambda\Lambda'}$ obtained upon reduction of the high-energy part of the spectrum is as follows:

$$\frac{dJ_{LL}^T}{d\ln D} = -\nu (J_{LL}^T)^2, \quad \frac{dJ_{LL}^{ST}}{d\ln D} = -\nu J_{LL}^{ST} J_{LL}^T,$$
$$\frac{dJ_{LR}^T}{d\ln D} = -\nu J_{LL}^T J_{LR}^T, \quad \frac{dJ_{LR}^{ST}}{d\ln D} = -\nu J_{LL}^{ST} J_{LR}^T, \quad (7)$$
$$\frac{dJ_{LR}^S}{d\ln D} = \frac{1}{2}\nu\left(J_{LL,+}^{ST} J_{LR,-}^{TS} + \frac{1}{2} J_{LL,z}^{ST} J_{LR,z}^{TS}\right).$$

Solving these equation with the boundary conditions $J_{\alpha\alpha'}^{\Lambda\Lambda'}(D) = J$, we obtain

$$J_{\alpha,\alpha'}^{TT} = \frac{J}{1 - \nu J \ln(D/T)}, \quad J_{\alpha,\alpha'}^{ST} = \frac{J}{1 - \nu J \ln(D/T)},$$
$$J_{LR}^{SS} = J - \frac{3}{4}\nu J^2 \frac{\ln(D/T)}{1 - \nu J \ln(D/T)}. \quad (8)$$

The structure of the renorm group equations (Fig. 3) shows that the Kondo singularity arising in the T-chan-

nel influences conductance in the *S*-channel. This influence is related to the presence of the operator **P** in the tunneling Hamiltonian, which breaks the spin symmetry of the DQD. Thus, the Kondo effect in this system exists only due to the dynamic symmetry inherent in the DQD.

The differential conductance $G(eV, T)/G_0 \sim \left|J_{LR}^{ST}\right|^2$ [15], where $G_0 = e^2/\pi\hbar$, is a function of the universal parameters T/T_K and eV/T_K,

$$G/G_0 \sim \ln^{-2}(\max[(eV - \delta), T]/T_K), \qquad (9)$$

with a maximum at $eV - \delta = 0$ (see Fig. 4). Thus, in contrast to the usual situation [9], whereby the Kondo peak (representing a zero bias anomaly) exhibits evolution or splitting at finite eV values, the Kondo peak in our case appears at a threshold bias of $eV_0 = \delta$. Owing to this threshold character, the peak is asymmetric (cf., e.g., [11]).

The asymmetry, as well as the broadening of the Kondo resonance are related to nonequilibrium character of the tunneling process. In contrast to the usual situation [11, 16], when relaxation takes place in the ground state of the QD, the spin triplet in our case appears only as a virtual state (Fig. 3) and, hence, the nonequilibrium effects are not as destructive. Both relaxation and asymmetry are determined by the imaginary part of the self-energy of the Green's function $\mathcal{G}_T(\omega)$. Figure 5 shows diagrams describing the self-energy in the same order as the renormalization of vertices. The diagrams of Figs 5a and 5b determine the main contribution to the imaginary part $\hbar/\tau_d$. For $\omega \sim eV$, this contribution amounts to $\sim(eV)(J/D)^2$ and contains no logarithmic corrections. Such corrections appear in the third order, but still outside the limits of the main logarithmic approximation, and are estimated as $eV(J/D)^3\ln(D/eV)$. As a result, we obtain as an estimate

$$\hbar/\tau_d \sim eV(\nu J_0^{ST})^2[1 + O(J_0^S \ln(D/(eV)))].$$

Comparing this damping to T_K and taking into account that (under the resonance conditions) $eV \sim \delta \sim J$, we arrive at the following condition for the existence of the anomalous Kondo peak at a finite bias:

$$\delta(\delta/D)^2 \ll T_K \ll \delta. \qquad (10)$$

Here, the right-hand inequality resembles the Doniach criterion for the stability of a Kondo singlet with respect to antiferromagnetic correlations (see, e.g., [1]). The conditions (10) are satisfied in a broad range of parameters since $\delta/D \ll 1$.

Another contribution, related to the reoccupation of levels as a result of the tunneling of nonequilibrium electrons, leads to asymmetry of the resonance line. These processes are described by the diagrams in Figs. 5e and 5f, in which at least one of the virtual sates is triplet. Such transitions, as well as the corresponding second-order processes, possess a threshold character and give small contributions to $\hbar/\tau_d$. As can be seen from Fig. 4, the asymmetry is small even at a significant damping.

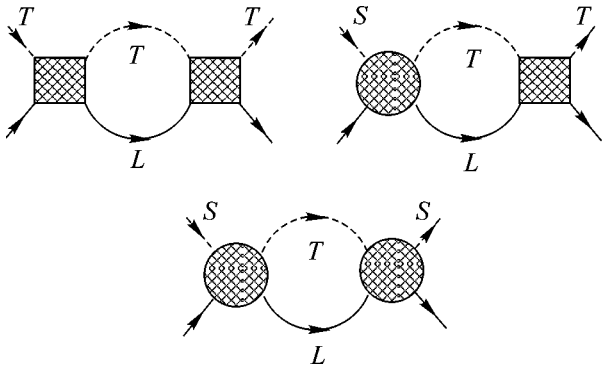

Fig. 3. Irreducible diagrams determining renorm group equations. Cross-hatched squares and circles represent vertices of the *T*–*T* and *S*–*T* transitions, respectively; other notations as in Fig. 2.

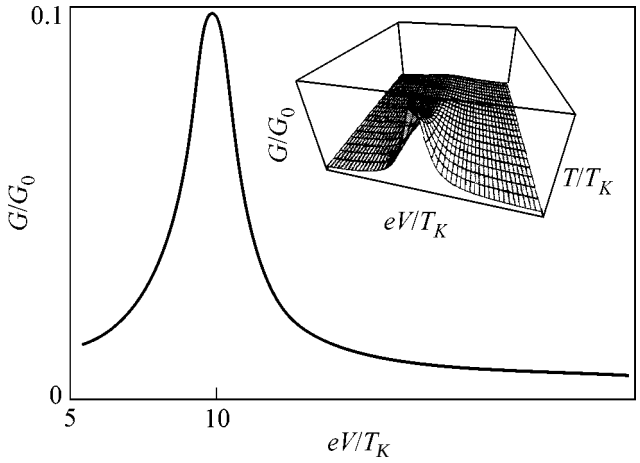

Fig. 4. The Kondo peak of the differential conductance as a function of two universal parameters eV/T_K and T/T_K (inset) and a curve for $\delta/T_K = 10$ and $\hbar/\tau T_K = 0.1$.

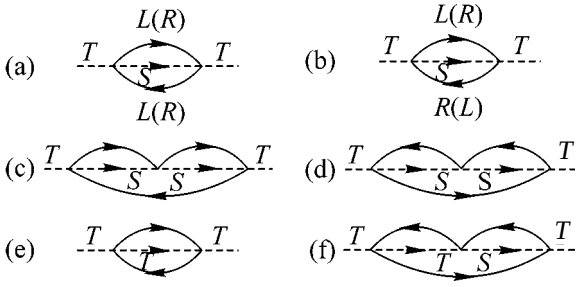

Fig. 5. The diagrams determining the main contribution to $\hbar/\tau T_K$ (a–d) (see text). The diagrams (e–f) describe threshold processes leading to the Kondo peak asymmetry.

Thus, we have described a situation in which the Kondo effect exists only under nonequilibrium conditions and is induced by an external voltage applied to electrodes in tunneling contact with a composite QD. In this case, the Kondo-type tunneling is induced by dynamic processes of the excitation of low-lying spin states of the QD, the ground state of which is a spin singlet. The simplest example of such a system is offered by a double QD with even occupation under the conditions of strong Coulomb blockade. The spin symmetry of such a QD is essentially that of a quantum spin rotator. Since a singlet ground state in quantum mechanics is always accompanied by triplet excitations, this situation is not very unusual and can probably be manifested as a peak in the differential conductance, observed at a nonzero bias in a Coulomb window with an even number of electrons. Such a peak should be distinguished from a maximum corresponding to the cotunneling via excited electron states [17].

This study was supported in part (M.N.K.) by the European Commission (LF Project) via the Weizman Institute (Israel) (contract #HPRI-CT-1999-00069) and by the Deutsche Forschungsgemeinschaft (SFB-410). The authors are grateful to P. Wölfle for fruitful discussions.

REFERENCES

1. D. Cox and A. Zawadowski, Adv. Phys. **47**, 599 (1998); L. Kouwenhoven and L. Glazman, Phys. World **253**, 33 (2001).
2. J. Appelbaum, Phys. Rev. Lett. **17**, 91 (1966).
3. L. I. Glazman and M. E. Raikh, Pis'ma Zh. Éksp. Teor. Fiz. **47**, 378 (1988) [JETP Lett. **47**, 452 (1988)]; T.-K. Ng and P. A. Lee, Phys. Rev. Lett. **61**, 1768 (1988).
4. D. Goldhaber-Gordon, J. Göres, M. A. Kastner, *et al.*, Phys. Rev. Lett. **81**, 5225 (1998); S. M. Cronenwett, T. H. Oosterkamp, and L. P. Kouwenhoven, Science **281**, 540 (1998); F. Simmel, R. H. Blick, J. P. Kotthaus, *et al.*, Phys. Rev. Lett. **83**, 804 (1999).
5. M. Pustilnik, Y. Avishai, and K. Kikoin, Phys. Rev. Lett. **84**, 1756 (2000); M. Eto and Yu. Nazarov, Phys. Rev. Lett. **85**, 1306 (2000).
6. K. Kikoin and Y. Avishai, Phys. Rev. Lett. **86**, 2090 (2001).
7. I. A. Malkin and V. I. Man'ko, *Dynamic Symmetries and Coherent States of Quantum Systems* (Nauka, Moscow, 1979).
8. K. Kikoin and Y. Avishai, Phys. Rev. B **65**, 115 329 (2002); T. Kuzmenko, K. Kikoin, and Y. Avishai, Phys. Rev. Lett. B **89**, 156 602 (2002).
9. Y. Meir and N. S. Wingreen, Phys. Rev. Lett. **68**, 2512 (1992); Phys. Rev. B **49**, 11 040 (1994); T.-K. Ng, Phys. Rev. Lett. **76**, 487 (1996); M. H. Hettler, J. Kroha, and S. Hershfield, Phys. Rev. B **58**, 5649 (1998).
10. O. Parcollet and C. Hooley, Phys. Rev. B **66**, 085 315 (2002); P. Coleman and W. Mao, cond-mat/0203001; cond-mat/0205004.
11. A. Rosch, J. Paaske, J. Kroha, and P. Wölfle, Phys. Rev. Lett. **90**, 076804 (2003).
12. L. W. Molenkamp, K. Flensberg, and M. Kemerink, Phys. Rev. Lett. **75**, 4282 (1995); F. Hofmann, T. Heinzel, D. A. Wharam, *et al.*, Phys. Rev. B **51**, 13 872 (1995).
13. V. N. Popov and S. A. Fedotov, Zh. Éksp. Teor. Fiz. **94** (3), 183 (1988) [Sov. Phys. JETP **67**, 535 (1988)].
14. M. N. Kiselev and R. Oppermann, Phys. Rev. Lett. **85**, 5631 (2000).
15. P. W. Anderson, J. Phys. C **3**, 2435 (1970); A. Kaminski, Yu. V. Nazarov, and L. I. Glazman, Phys. Rev. Lett. **83**, 384 (1999).
16. A. Rosch, J. Kroha, and P. Wölfle, Phys. Rev. Lett. **87**, 156 802 (2001).
17. S. De Franceschi, S. Sasaki, J. M. Elzerman, *et al.*, Phys. Rev. Lett. **86**, 878 (2001).

Translated by P. Pozdeev

JETP Letters, Vol. 77, No. 7, 2003, pp. 371–375. Translated from Pis'ma v Zhurnal Éksperimental'noĭ i Teoreticheskoĭ Fiziki, Vol. 77, No. 7, 2003, pp. 439–444.

Observation of the External-ac-Current-Induced dc Voltage Proportional to the Steady Current in Superconducting Loops

S. V. Dubonos, V. I. Kuznetsov, I. N. Zhilyaev, A. V. Nikulov, and A. A. Firsov

Institute of Microelectronic Technology and Ultra-High-Purity Materials, Russian Academy of Sciences, Chernogolovka, Moscow region, 142432 Russia

Received February 20, 2003

A dc voltage induced by an external ac current was observed in a system of asymmetric aluminum loops at temperatures corresponding to 0.95–0.98 of the superconducting transition temperature. The voltage magnitude and sign change periodically in a magnetic field with a period corresponding to the magnetic flux quantum through the loop. The amplitude of these oscillations depends nonmonotonically on the amplitude of ac current and is almost independent of its frequency in the range from 100 Hz to 1 MHz. The observed phenomenon is interpreted as the result of displacing the loop into a dynamic resistive state by the external current, where the loop is "switched" back and forth between the closed superconducting state with a nonzero steady current and the nonclosed state with a nonzero resistance along the loop circle. It is shown that voltages are summed up in a system of loops connected in series. For systems with one, three, and twenty loops, the voltage reaches 10, 40, and 300 μV, respectively. © *2003 MAIK "Nauka/Interperiodica".*

PACS numbers: 74.40.+k

It is known that, due to the momentum circulation

$$\oint_l dlp = \oint_l dl(mv + 2eA) = m\oint_l dlv + 2e\Phi = n2\pi\hbar \quad (1)$$

in superconducting loops, the current $I_p = sj_p = s2en_sv_s$ is stable. Its magnitude and sign show periodic dependence on the magnetic flux Φ through the loop, with a period corresponding to the magnetic-flux quantum $\Phi_0 = \pi\hbar/e$, because the quantized velocity circulation

$$\oint_l dlv_s = \frac{2\pi\hbar}{m}\left(n - \frac{\Phi}{\Phi_0}\right) \quad (2)$$

of superconducting pairs takes values corresponding to energy minimum; i.e., the value of $(n - \Phi/\Phi_0)$ varies, with varying Φ, within the interval from –1/2 to 1/2 [1]. In the stationary state with a time-independent density of superconducting pairs, the steady current can flow only in a closed superconducting state, i.e., if there is phase coherence along the entire loop circle and the resistance R_l along the circle is zero.

However, according to the Little–Parks experiment [2] and theory [3], steady current $I_p \neq 0$ is observed not only in the superconducting state with $R_l = 0$ but also for $R_l > 0$. It is known that, if a current $I = \oint_l dlE/R_l$ induced by the Faraday electromotive force $\oint_l dlE = -d\Phi/dt$ flows along the loop circle, then the potential difference $V = (\langle\rho/s\rangle_{ls} - \langle\rho/s\rangle_l)l_sI$ should be nonzero in the segment l_s with the average resistance $R_{ls}/l_s = \langle\rho/s\rangle_{ls} = \int_{ls} dl\rho/sl_s$ differing from the average resistance $R_l/l = \langle\rho/s\rangle_l = \oint_l dl\rho/sl$ along the entire circle. If the analogy with the ordinary current applies to the steady current, then a constant potential difference proportional to $I_p(\Phi/\Phi_0)$ will be observed in the segment of inhomogeneous superconducting loop with $I_p \neq 0$ and $R_l > 0$.

The voltage oscillations $V(\Phi/\Phi_0) \propto I_p(\Phi/\Phi_0)$ of this type were observed in our work [4] for the segments of an asymmetric aluminum loop. We observed them in a narrow temperature range of $(0.988–0.994)T_c$, where T_c corresponds to the midpoint of the resistive transition; their amplitude increased with lowering temperature in this interval. Such a dependence testifies that $V(\Phi/\Phi_0)$ is induced by external noises. The purpose of this work is to elucidate how noises of various frequency and intensity act on $V(\Phi/\Phi_0)$. With this aim, the effect of the ac current $I_{ac} = \Delta I\sin(2\pi ft)$ varying in frequency f and amplitude ΔI on $V(\Phi/\Phi_0)$ was studied at lower temperatures of $(0.95–0.98)T_c$ where the low-intensity random noise shows a weak dependence on $V(\Phi/\Phi_0)$ because of the higher critical current.

Systems composed of 3 and 20 (Fig. 1) asymmetric aluminum loops with the superconducting transition temperature $T_c \approx 1.3$ K, resistance of a square of ≈0.5 Ω/□ at 4.2 K, and the resistance ratio $R(300\text{ K})/R(4.2\text{ K}) \approx 2$ were used for the study. We used a loop system, rather than a single loop, as in [4], with the aim to verify whether the voltages are summed in the loops connected in series. All loops had a diameter of 4 μm and

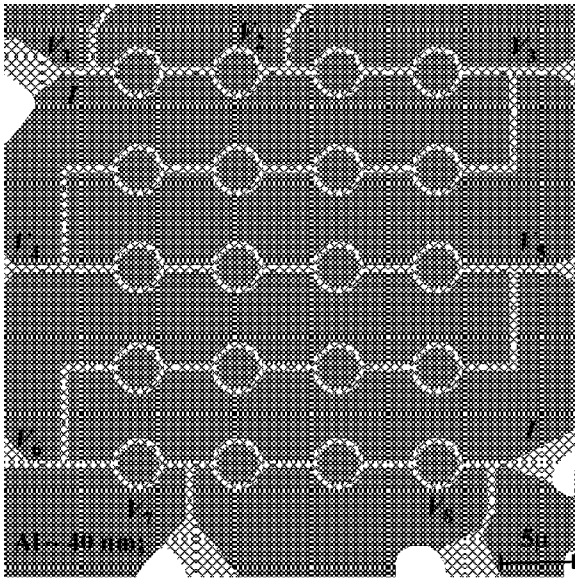

Fig. 1. Photograph of a system of series 20 aluminum asymmetric loops with the current I and potential V_i contacts.

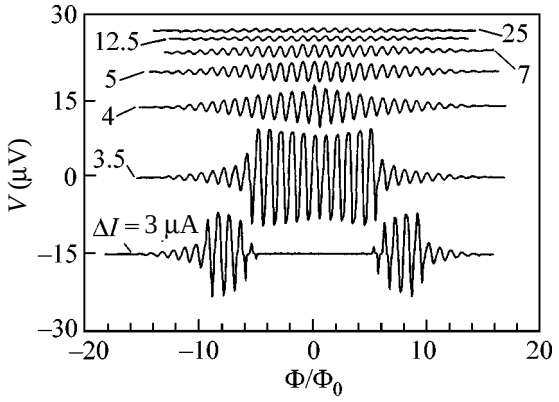

Fig. 2. Dc voltage oscillations in a magnetic field, as measured for one of the loops at $T = 1.280$ K $\approx 0.97T_c$ and the external current I_{ac} with frequency $f = 2.03$ kHz and amplitude $\Delta I = 3$, 3.5, 4, 5, 7, 12, and 25 μA. All curves except for $\Delta I = 3.5$ μA are vertically shifted.

a thickness of 40 nm. They were asymmetric; their halves l_w and l_n had different widths $w_w = 0.4$ μm and $w_n = 0.2$ μm (Fig. 1) and, respectively, the cross-sections $s_w \approx 0.016$ μm^2 and $s_n \approx 0.008$ μm^2. The microstructures were fabricated on a Si substrate using electron-beam lithography based on a JEOL-840A electron microscope. Exposure was performed at a voltage of 25 kV and a current of 30 pA. The electron beam was controlled by a PC using the PROXY program package.

Measurements were made in a standard cryostat with He^4 as a coolant, whose evacuation allowed the temperature to be lowered to 1.2 K. A magnetic field perpendicular to the sample plane was produced by a superconducting magnet. Each structure had ten contacts, two of which (e.g., *I–I* in Fig. 1) were used to deliver ac current I_{ac} with a frequency from $f = 100$ Hz to $f = 1$ MHz and the amplitude ΔI up to 50 μA, and the others (e.g., V_1–V_8 in Fig. 1) served as potential contacts.

Measurements showed that, for any frequency in the interval from $f = 100$ Hz to $f = 1$ MHz, I_{ac} induced oscillations of $V(\Phi/\Phi_0)$ if the amplitude of ac current exceeded some critical value ΔI_{cr} (Fig. 2). Similar to the critical superconducting current I_c, this critical value decreased with increasing temperature and magnetic field. This is reflected in Fig. 2 by the fact that the oscillations of $V(\Phi/\Phi_0)$ appear for $\Delta I = 3$ μA only at high Φ/Φ_0 values. Similar to the Little–Parks oscillations (see, e.g., [5]), the oscillations of $V(\Phi/\Phi_0)$ are damped at large Φ/Φ_0 (Fig. 2), which is explained by the field-induced suppression of superconductivity and, hence, I_p in finite-thickness strips.

The oscillations of $V(\Phi/\Phi_0)$ observed at $\Delta I > \Delta I_{cr}$ are similar to the $I_p(\Phi/\Phi_0)$ oscillations [1]. Both curves pass through zero at $\Phi = n\Phi_0$ and $\Phi = (n + 0.5)\Phi_0$. This is explained by the fact that the quantum value n of pair momentum circulation in a closed superconducting state acquires, with an overwhelming probability, the only integer value corresponding to the energy minimum, except for the vicinity of $\Phi = (n + 0.5)\Phi_0$, where, simultaneously, the energies of two states with oppositely directed velocities are minimal. For this reason, $V(\Phi/\Phi_0) \propto I_p(\Phi/\Phi_0) \propto (\langle n\rangle - \Phi/\Phi_0)$, where the mean $\langle n\rangle \approx n$ for Φ/Φ_0 far from $(n + 0.5)$, $(\langle n\rangle - \Phi/\Phi_0) \approx 0$ for $\Phi/\Phi_0 \approx (n + 0.5)$, and the voltage maxima $|V|_{\max}$ occur at $\Phi/\Phi_0 \approx (n + 0.25)$ and $\Phi/\Phi_0 \approx (n + 0.75)$.

$|V|_{\max}$ depends nonmonotonically on the ac current amplitude ΔI both in a single loop (Fig. 2) and in a loop system and shows no appreciable dependence on the I_{ac} frequency over the whole range studied from $f = 100$ Hz to $f = 1$ MHz. After the amplitude $|V|_{\max}$ rapidly reaches its maximum at a current amplitude close to ΔI_{cr}, it decreases monotonically upon further increase in ΔI (Fig. 2). At large ΔI, the $|V|_{\max}(\Delta I)$ dependence is close to $|V|_{\max} \propto 1/\Delta I$. Measurements showed that, both the position of the $|V|_{\max}(\Delta I)$ curve maximum and the critical value ΔI_{cr} shift to lower ΔI values with increasing temperature.

In loops with similar asymmetry and size, the voltage $V(\Phi/\Phi_0)$ should oscillate synchronously in a magnetic field. For this reason, there is a fundamental possibility of summing this voltage in a system of series loops. Our studied showed that this possibility can easily be realized. We managed to observe oscillations with amplitude $|V|_{\max}$ up to 10 μV (Fig. 2) in a single loop, up to 40 μV in a system of three loops, and up to 300 μV in a system of 20 loops (Fig. 3).

As with every rectification, the observed "rectification" of the external ac current I_{ac} is possible only if the current–voltage characteristic (CVC) is asymmetric about the external current (Fig. 4). The observed periodic change in the sign and magnitude of this asymmetry in a magnetic field occurs in a steady current, because $V(\Phi/\Phi_0) \propto I_p(\Phi/\Phi_0)$. This change can be explained by the fact that the steady current flowing along the loop circle increases the overall current in one of its halves (cf. Fig. 4, bottom right), as a result of which the criticality arises at lower I_{ac} values.

In a closed superconducting state, the distribution of $I_{ac} = I_w + I_n$ over loop halves l_w and l_n is determined by the quantization of velocity circulation (2): $l_n v_n - l_w v_w = l_n I_n/s_n 2en_{sn} - l_w I_w/s_w 2en_{sw} = l_n j_n/2en_{sn} - l_w j_w/2en_{sw} = (2\pi\hbar/m)(\langle n\rangle - \Phi/\Phi_0)$. Since the lengths l_w and l_n of the halves and the corresponding superconducting pair densities n_{sn} and n_{sw} are the same, the current densities in both halves are the same for $I_p = 0$ (i.e., for $(\langle n\rangle - \Phi/\Phi_0) = 0$ and equal to $j_n = j_w = j_{ac} = I_{ac}/(s_n + s_w)$), so that they simultaneously reach the critical value at $I_{ac}/(s_n + s_w) = j_c$. The steady current alters the current densities in the loop halves (Fig. 4). Depending on the directions of I_p and I_{ac}, the density increases either in one or another half. In Fig. 4, the density increases in the narrow half, when I_p flows counter-clockwise while I_{ac} flows from left to right, or vice versa. The current densities in the loop halves change differently, by I_p/s_n and I_p/s_w. For this reason, the CVC is asymmetric about the external current I_{ac} at $\Phi \neq n\Phi_0$ and $\Phi \neq (n + 0.5)\Phi_0$, while the asymmetry value and its sign change with changing I_p. For an external current directed along I_p in the narrow half, the critical value $|I_{ac}|_{c+}/(s_n + s_w) = j_c - I_p/s_n$ is achieved at lower I_{ac} values than for I_{ac} directed along I_p in the broadened half, where the criticality is achieved at $|I_{ac}|_{c-}/(s_n + s_w) = j_c - I_p/s_w$ (Fig. 4). The difference $|I_{ac}|_{c-} - |I_{ac}|_{c+} = (s_n + s_w)(j_c - I_p/s_w) - (s_n + s_w)(j_c - I_p/s_n) = (s_w/s_n - s_n/s_w)I_p \approx 1.5I_p$. According to the experimental data, $|I_{ac}|_{c+} \approx 0.45$ μA and $|I_{ac}|_{c-} \approx 1.0$ μA, as is shown in the CVC in Fig. 4 for $T \approx 0.99T_c$, $I_p = (|I_{ac}|_{c-} - |I_{ac}|_{c+})/1.5 \approx 0.37$ μA, and $(s_n + s_w)j_c \approx 1.6$ μA. At $|I_{ac}| \approx (s_n + s_w)j_c \approx 1.6$ μA, the CVC shows a singularity, and, at larger $|I_{ac}|$ values, it coincides with its normal-state shape (Fig. 4).

The effect of a persistent current on the transition to the resistive state is illustrated by three upper oscillograms in Fig. 5, which were recorded at temperature $T \approx 0.96T_c$ and external current amplitude $\Delta I = 9$ μA. At $\Phi = 0$, the resistive state is not observed. This signifies that, at a temperature of $\approx 0.96T_c$, the critical current density j_c exceeds $\Delta I/s_w \approx 9$ μA/0.016 m^2 $\approx 5.6 \times 10^8$ A/m^2, because the loop-connecting strip cross section is equal to s_w (Fig. 1). For $\Phi = 0.75\Phi_0$ corresponding to the maximum of I_p, the resistive state is observed only for a single I_{ac} direction, which is shown in Fig. 5. This signifies that $\Delta I(s_n + s_w) + I_p/s_n > j_c$ and $\Delta I(s_n + s_w) + I_p/s_w < j_c$. From the first inequality and the $j_c > \Delta I/s_w$ inequality obtained above, it follows that $I_p > \Delta I s_n^2/s_w(s_n + s_w) =$

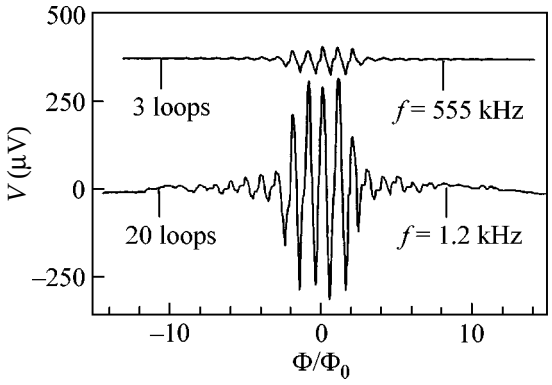

Fig. 3. Magnetic-field induced oscillations of the dc voltage in a system of 20 loops at $T = 1.245$ K $\approx 0.97T_c$ for the external current I_{ac} with $f = 1.2$ kHz and $\Delta I = 3.2$ μA and in a system of three loops at $T = 1.264$ K $\approx 0.96T_c$ for the external current I_{ac} with $f = 555$ kHz and $\Delta I = 4.5$ μA. The second curve is shifted vertically by 370 μV.

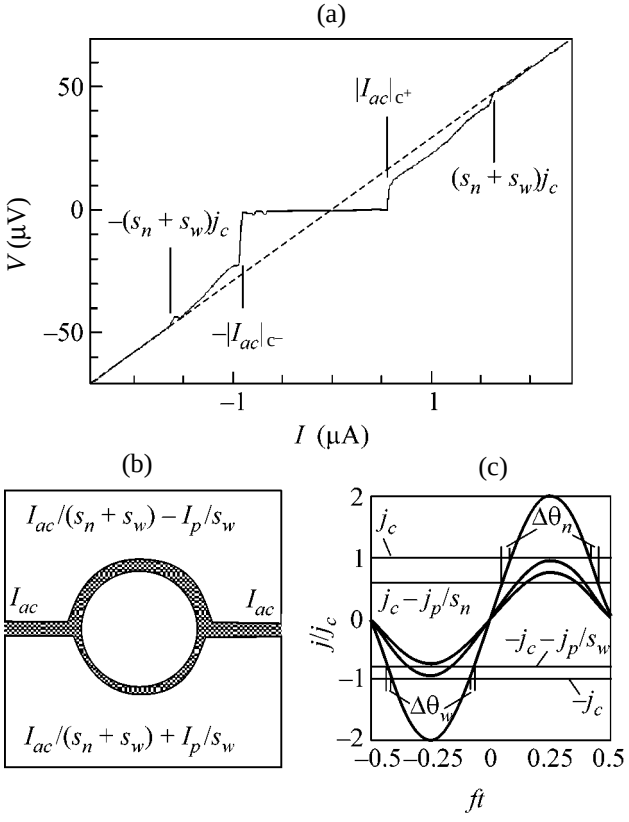

Fig. 4. (a) CVC of a system of two loops at $T \approx 0.99T_c$, $\Phi \neq n\Phi_0$ and $\Phi \neq (n + 0.5)\Phi_0$; (b) variation of the current density in the loop halves for $I_p \neq 0$; and figure (c) clarifies the nonmonotonic dependence of the oscillation amplitude $V(\Phi/\Phi_0)$ on ΔI.

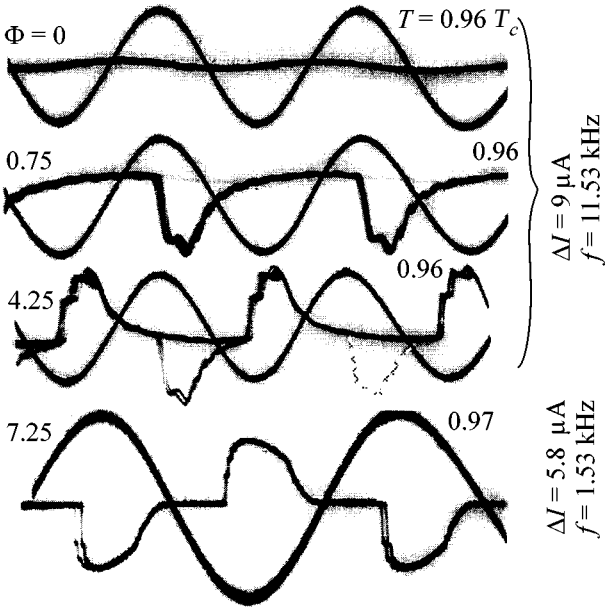

Fig. 5. Four pairs of voltage oscillograms measured in a system of three loops, together with the currents induced this voltage.

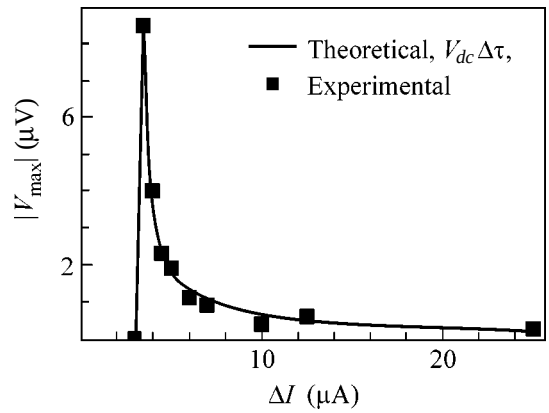

Fig. 6. The $V(\Phi/\Phi_0)$ oscillation amplitude as a function of the amplitude ΔI of the external current with $f = 2.03$ kHz, as measured for one of the loops at $T = 1.280$ K $\approx 0.97T_c$. The curve shows the $V_{dc}(\Delta\Theta_n - \Delta\Theta_w)/\Theta = V_{dc}\Delta\tau$ dependence calculated for $I_c = 4.5$ μA, $I_p \approx 0.5$ μA, and $V_{dc} \approx 25$ μV.

$\Delta I/6 \approx 1.5$ μA for $T \approx 0.96T_c$ and $\Phi = 0.75\Phi_0$. In a higher magnetic field with $\Phi = 4.25\Phi_0$ corresponding to the opposite direction of I_p, the steady resistive state is observed for the oppositely directed I_{ac}, while the resistive state in the other direction is unstable (Fig. 5), evidencing the suppression of j_c by a magnetic field. The amplitude $\Delta I = 9$ μA corresponds to the maximum of the $|V|_{\max}(\Delta I)$ curve for $T \approx 0.96T_c$. At larger amplitudes, $\Delta I(s_n + s_w) + I_p/s_w > j_c$, the resistive state is observed for both I_{ac} directions (Fig. 5).

The resistive state induced by a persistent current cannot be stationary, because, e.g., the current in this case should be damped upon the transition of, e.g., l_n to the resistive state with $R_n > 0$, which signifies that the current through l_n decreases to $j_n < j_c$. For this reason, both superconducting stationary states with different connectivities are unstable at $j_c - I_p/s_n < I_{ac}/(s_n + s_w) < j_c$, so that the loop should switch between them with the eigenfrequency ω, which is determined by the relaxation time to the equilibrium superconducting state [6]. A half of this dynamical resistive state, in which I_{ac} and I_p are directed oppositely and $I_{ac}/(s_n + s_w) - I_p/s_w < I_{ac}/(s_n + s_w) < j_c$, is in the superconducting state, whereas its other half, where they coincide, is switched between the states with $R = 0$ and $R > 0$.

Upon switching, the pair momentum Δp changes in the superconductivity half (e.g., l_w), and, as a result, the external current $I_{ac} = I_w + I_n$ is redistributed between the loop halves. This change proceeds under the action of electric field $dp/dt = md\mathbf{v}_s/dt + 2edA/dt = 2eV_w/l_w = 2eR_nI_n/l_w$ with $R_n > 0$, while the initial state is restored due to the quantization of momentum circulation (1) after returning l_n to the superconducting state [6]. This fact makes it clear why the pair momentum does not change, on the average, despite the fact that the time-averaged voltage $V_{dc} = \langle V_w \rangle_t \neq 0$. Since its one-directional change is caused by an electric field, one has

$$V_{dc} = \Delta p \omega l_w/2e. \qquad (3)$$

The change Δp in momentum is limited, because I_n can change only from $I_{ac}s_n/(s_n + s_w) + I_p$ to zero, while I_w cannot exceed the critical value $s_w j_c$. According to the initial restriction, $\Delta I_w < I_{ac}/3 + I_p$, and, according to the second, $\Delta I_w < 3I_p$. As the steady current decreases to zero, the pair-momentum circulation changes by $2\pi\hbar(\langle n \rangle - \Phi/\Phi_0)$. Hence, $\Delta p < 3(2\pi\hbar/l)(\langle n \rangle - \Phi/\Phi_0)$. From this inequality and Eq. (3) it follows that, for the voltage $V_{dc} = 70$ μV, which was observed by us for $n - \Phi/\Phi_0 = 0.25$, the switching frequency $\omega = 2eV_{dc}/\Delta p l_w > 4/3(e/\pi\hbar)(l/l_w)V_{dc} = 8/3(483.6\ \text{MHz}/\mu\text{V})V_{dc}$ should exceed 90 GHz.

Changes in the momentum $\Delta p = \int_{t_{R>0}} dt(dp/dt) = \int_{t_R>0} dt 2eV_m/l_w$ and current I_n can be lower than their limiting values, if the residence time $t_{R>0}$ in the resistive state is shorter than the current relaxation time, which is determined by the kinetic $(l_w m/2e)d\mathbf{v}_s/dt = (l_w m/s4e^2 n_s)dI_w/dt = L_{\text{kin}}dI_w/dt$ and geometric $l_w dA/dt = LdI_w/dt$ inductances and resistance R_n. Since $L_{\text{kin}}/L \approx \lambda_L^2/s$ for a thin superconductor [6], one has in the weak screening case with $s_w \approx 0.016\ \mu\text{m}^2 \ll \lambda_L^2(T) =$

$\lambda_L^2(0)/(1 - T/T_c) \approx 0.0025\ \mu m^2/(1 - T/T_c) \approx 0.1\ \mu m^2$ that the kinetic inductance $L_{kin} \approx m0.5l/4e^2 n_{sw} s_w \approx \mu_0 0.5 l \lambda_L^2(T)/s_w \approx 4 \times 10^{-11}$ H exceeds the geometric inductance. The normal-state resistance $R_{n,n} \approx 15\ \Omega$ of the narrow half corresponds to the relaxation time $L_{kin}/R_n \approx 0.3 \times 10^{-11}$ s. The measured values $V_{dc} = \langle V_w \rangle_t = \langle R_n I_n \rangle_t < R_{n,n} \langle I_n \rangle_t$ indicate that the time-averaged current, e.g., through the narrow half $\langle I_n \rangle_t > V_{dc}/R_{n,n}$ exceeds $I_{ac} s_n/(s_n + s_w)$ and is close to $I_{ac} s_n/(s_n + s_w) + I_p$ in the superconducting state. For example, for the CVC shown in Fig. 4, $V_{dc} \approx 7.4\ \mu V$ per one loop at $I_{ac} \approx 0.7\ \mu A$, which corresponds to $\langle I_n \rangle_t > V_{dc}/R_{n,n} \approx 0.49\ \mu A$, $I_{ac} s_n/(s_n + s_w) \approx 0.23\ \mu A$, and $I_{ac} s_n/(s_n + s_w) + I_p \approx 0.6\ \mu A$.

Inasmuch as the loop is in the superconducting state with $R_l = 0$ at $|I_{ac}|/(s_n + s_w) < j_c - I_p/s_n$ and undergoes transition to the usual resistive state with $I_p = 0$ at $|I_{ac}|/(s_n + s_w) > j_c$, only the dynamic resistive state with $\langle I_p \rangle_t \neq 0$ and $\langle R_l \rangle_t > 0$ can contribute to the dc voltage $V(\Phi/\Phi_0) \propto I_p$. For this reason, the time-averaged voltage $V(\Phi/\Phi_0) = \int_\Theta dt V_{dc}/\Theta$ can be estimated at $V = (V_{dc,n}\Delta\Theta_n - V_{dc,w}\Delta\Theta_w)/\Theta$, where $\Delta\Theta_n$ and $\Delta\Theta_w$ are the portions of the period $\Theta = 1/f$ during which $j_c - I_p/s_n < |\Delta I \sin(2\pi f t)|/(s_n + s_w) < j_c$ and $j_c - I_p/s_w < |\Delta I \sin(2\pi f t)|/(s_n + s_w) < j_c$ (Fig. 4), and $V_{dc,n}$ and $V_{dc,w}$ are the average voltages induced during these times. The oscillation amplitude $V(\Phi/\Phi_0)$ is maximal at $j_c - I_p/s_n < \Delta I/(s_n + s_w) < j_c - I_p/s_w$, where the voltage is induced only for one of the ac current directions (Fig. 5) and $V = V_{dc,n}\Delta\Theta_n/\Theta$. For $\Delta I/(s_n + s_w) > j_c + I_p/s_w$, the time-average voltage $V = (V_{dc,n}\Delta\Theta_n - V_{dc,w}\Delta\Theta_w)/\Theta$ decreases sharply because of the appearance of the resistive state with $-V_{dc,w}\Delta\Theta_w/\Theta$ for the oppositely directed I_{ac} (Fig. 5). However, the oscillation amplitude for $V(\Phi/\Phi_0)$ is still nonzero, because $\Delta\Theta_n$ and $\Delta\Theta_w$ are different in magnitude (Fig. 4). The further decrease of this amplitude with increasing ΔI (Figs. 2, 6) can be explained by a decrease in $\Delta\Theta_n$ and $\Delta\Theta_w$ (Fig. 4). The dependence $V_{dc}(\Delta\Theta_n - \Delta\Theta_w)/\Theta = V_{dc}\Delta\tau(\Delta I)$, where $\Delta\tau(\Delta I) = (\Delta\Theta_n - \Delta\Theta_w)/\Theta$ is calculated with parameters $I_c \approx 4.5\ \mu A$ and $I_p \approx 0.5\ \mu A$ and describes the $|V|_{max}(\Delta I)$ dependence (Fig. 6) in the $V_{dc,n} \approx V_{dc,w} \approx V_{dc} \approx 25\ \mu V$ approximation rather well.

In summary, the oscillations of $V(\Phi/\Phi_0)$ voltage observed in [4] could be induced by a broad-spectrum noise. Since the critical current and the critical value ΔI_{cr} decrease to zero as T_c is approached, these oscillations can be induced at $T \approx T_c$ by a low-intensity noise, and a system of asymmetric superconducting loops can be used for their detection.

We are grateful to V.A. Tulin for discussion of the results. This work was supported by the Presidium of the Russian Academy of Sciences within the framework of the fundamental program "Low-Dimensional Quantum Structures."

REFERENCES

1. M. Tinkham, *Introduction to Superconductivity* (McGraw-Hill, New York, 1975; Atomizdat, Moscow, 1980).
2. W. A. Little and R. D. Parks, Phys. Rev. Lett. **9**, 9 (1962).
3. I. O. Kulik, Zh. Éksp. Teor. Fiz. **58**, 2171 (1970) [Sov. Phys. JETP **31**, 1172 (1970)].
4. S. V. Dubonos, V. I. Kuznetsov, A. V. Nikulov, and V. A. Tulin, in *Abstracts of All-Russian Scientific and Technical Conference on Micro- and Nano-Electronics 2001* (2001), Vol. 2, P2-25; S. V. Dubonos, V. I. Kuznetsov, and A. V. Nikulov, in *Proceedings of 10th International Symposium on Nanostructures: Physics and Technology* (Physicotechnical Inst., St. Petersburg, 2002), p. 350.
5. H. Vloeberghs, V. V. Moshchalkov, C. van Haesendonch, *et al.*, Phys. Rev. Lett. **69**, 1268 (1992).
6. A. V. Nikulov, Phys. Rev. B **64**, 012505 (2001).

Translated by V. Sakun

JETP Letters, Vol. 77, No. 7, 2003, pp. 376–380. Translated from Pis'ma v Zhurnal Éksperimental'noĭ i Teoreticheskoĭ Fiziki, Vol. 77, No. 7, 2003, pp. 445–449.

Phononless Hopping Conduction in Two-Dimensional Layers of Quantum Dots

A. I. Yakimov*, A. V. Dvurechenskiĭ*, A. I. Nikiforov*, and A. A. Bloshkin**

** Institute of Semiconductor Physics, Siberian Division, Russian Academy of Sciences, Novosibirsk, 630090 Russia*
e-mail: yakimov@isp.nsc.ru
*** Novosibirsk State University, Novosibirsk, 630090 Russia*
Received February 20, 2003

Regularities are studied in charge transport due to the hopping conduction of holes along two-dimensional layers of Ge quantum dots in Si. It is shown that the temperature dependence of the conductivity obeys the Efros–Shklovskii law. It is found that the effective localization radius of charge carriers in quantum dots varies nonmonotonically upon filling quantum dots with holes, which is explained by the successive filling of electron shells. The preexponential factor of the hopping conductivity ceases to depend on temperature at low temperatures ($T < 10$ K) and oscillates as the degree of filling quantum dots with holes varies, assuming values divisible by the conductance quantum e^2/h. The results obtained indicate that a transition from phonon-assisted hopping conduction to phononless charge transfer occurs as the temperature decreases. The Coulomb interaction of localized charge carriers has a dominant role in these phononless processes. © *2003 MAIK "Nauka/Interperiodica".*

PACS numbers: 73.63.Kv; 72.20.Ec

INTRODUCTION

If the resistance of a two-dimensional disordered system is larger than a value determined by the resistance quantum h/e^2, where h is Planck's constant and e is the elementary charge unit, then the system occurs on the dielectric side of the metal–insulator transition and its conductance G tends to zero as the temperature T decreases [1, 2]. In the regime of the strong localization of charge carriers, when the localization radius ξ is much smaller than the distance between localized states, charge transfer is carried out through tunneling hops of electrons from one center to another, and the hopping length at low temperatures increases with decreasing temperature [3]. The occurrence of disorder of certain origin in a system is the reason for the spread of energy levels corresponding to various localized states. Therefore, in a transition between localization centers, an electron is forced to absorb or emit phonons. Under conditions of this conventional phonon-assisted mechanism of hopping transport, the temperature dependence of the conductance takes the form

$$G(T) = G_0 \exp[-(T_0/T)^x], \quad (1)$$

where the parameter T_0 is determined by the properties of the material and the exponent $x < 1$ is determined by the energy dependence of the density of states at the Fermi level $g(E_f)$. If the electron–electron interaction in the system is insignificant and $g(E_f) = \text{const}$, then $x = 1/3$ (the Mott law for a two-dimensional system) and $T_0 = 13.8/k_B g(E_f)\xi^2$, where k_B is the Boltzmann constant [4]. It was predicted theoretically [5, 6] and then demonstrated in experiments with $GaAs/Al_xGa_{1-x}As$ [7] and Ge/Si heterostructures with Ge quantum dots (QDs) [8] with an artificial screen introduced in the system that the occurrence of long-range Coulomb interaction leads to the Efros–Shklovskii law

$$G(T) = G_0 \exp[-(T_0/T)^{1/2}], \quad (2)$$

where $T_0 = 6.2e^2/k_B\kappa\xi$ [6], where κ is the relative dielectric constant. Within the mechanism of phonon-assisted hopping conduction, the preexponential factor G_0 takes the form $G_0 = \gamma T^m$, where γ is a temperature-independent parameter reflecting the characteristic frequency of "attempts" of electron hops. Theoretical calculations [6, 9] and experimental studies [7, 10, 11] indicate that the exponent m has a value of about $m \sim -1$.

In 1994, Aleiner, Polyakov, and Shklovskii hypothesized that under certain conditions electron–electron interaction rather than phonons can stimulate electron transitions between localized states [12]. In this case, the preexponential factor G_0 does not depend on temperature. The question of the effect of electron–electron interaction on the conductivity of two-dimensional systems became especially pressing after the repeated discovery of the metal–insulator transition [1]. For systems with small disorder in which the fluctuation amplitude of the Coulomb potential is larger than the characteristic disorder energy because of random charge exchange between groups of closely spaced localized states, the phononless mechanism of hopping conduction was proposed by Kozub, Baranovskii, and

Shlimak [13]. Because of random acts of electron hops between states, the Coulomb potential in the surrounding system fluctuates in time. In turn, the interaction of this potential with carriers bound on the centers and participating in hopping charge transfer changes their energy and, hence, the probability of tunneling transitions. At certain instants of time a resonance situation arises when two spatially close levels coincide in energy and the charge carrier passes from one center to another. In this case, phonons are not necessary for charge transport, and Coulomb interaction is the factor assisting hopping charge transfer. The authors of [13] showed that, under conditions when this phononless mechanism is manifested, the temperature dependence of conductivity must be described by an equation similar to Eq. (2) with a temperature-independent preexponential factor having a value of order e^2/h.

Recently, experimental works appeared carried out with Si MIS transistors [14], Si/SiGe quantum wells [15], GaAs/AlGaAs heterostructures [2, 16], and Ge/Si quantum dots [8], in which two-dimensional hopping conduction of the type given by Eq. (2) was observed but with a temperature-independent preexponential factor equal to either e^2/h [8, 14, 16] or $2e^2/h$ [2, 15]. These results were contradictory to the model of phonon-assisted hopping conduction in two-dimensional disordered systems and pointed to the necessity of searching for new mechanisms of hopping charge transport. The drawback of the works cited above was the fact that G_0 = const was *a priori* assumed in the analysis of experimental data, whereas it was necessary to show that actually $m = 0$. Because of this instance, the problem of experimentally revealing phononless hopping conduction has not yet been solved.

In our opinion, Ge/Si heterostructures containing layers of self-assembled Ge quantum dots that are formed during the heteroepitaxy of elastically strained systems [17] are best suitable for this purpose as the object of investigations, because (1) it is possible to obtain dense arrays with a QD layer density of up to 10^{12} cm^{-2} [18], in which the hopping transport of holes between QDs is the dominating mechanism of current flow at low temperatures [8]; (2) because of the specificity of heteroepitaxy, Ge nanoclusters lie exactly in one plane (growth plane); that is, there is no disorder factor associated with disordering in the structure growth direction; (3) as distinct from the majority of impurities in semiconductors, assemblies of QDs can serve as a system of multicharged localization centers, in which the role of Coulomb potentials is especially important. The goal of this work was to determine the mechanism and regularities of charge transfer in layers of Ge/Si quantum dots.

FORMATION OF GE/SI HETEROSTRUCTURES WITH QDs

Samples were grown by molecular-beam epitaxy on Si(001) substrates with a resistivity of 1000 Ω cm doped with boron up to a concentration of ~10^{13} cm^{-3}. The growth temperature of Si layers was, respectively, 800 and 500°C before and after the deposition of the Ge layer. A Ge layer eight monolayers thick (≈10 Å) was introduced into the middle of the 90-nm Si layer grown on the substrate at a temperature of 300°C. The Ge nanoclusters formed in this case had the shape of pyramids. The average sizes of the pyramid base in the growth plane were 10 nm, the height was ~1 nm, and the layer density of nanoclusters was 4×10^{11} cm^{-2} [19]. The controlled filling of Ge islands with holes was carried out by introducing a Si layer δ-doped with boron in the samples at a distance of 5 nm below the QD layer. Because the ionization energy of boron impurities in silicon comprises only 45 meV, and the energies of the first ten hole levels in germanium pyramids of this size counted from the Si valence band top are 200–320 meV [20], holes at temperatures below room temperature leave the impurities and fill levels in QDs. The concentration of boron in various samples varied from 2×10^{11} cm^{-2} to 2.4×10^{12} cm^{-2}, which allowed the average number of holes N_h per one Ge QD to be varied from 0.5 to 6 at a step of 0.5. Ohmic contacts were formed by sputtering Al islands on the sample surface followed by heating the structure at a temperature of 400°C in a nitrogen atmosphere. The current was measured at different T at voltages no higher than 20 mV, which corresponded to the ohmic region of current–voltage characteristics throughout the entire temperature range studied in this work.

EXPERIMENTAL RESULT

Experimental temperature dependences of the conductance in e^2/h units are given in Fig. 1 in Arrhenius coordinates for samples with different numbers of holes N_h. In all samples at low temperatures $G(T) \lesssim e^2/h$, which is characteristic of the dielectric side of the metal–insulator transition. In order to obtain detailed information on the functional dependence $G(T)$, we used the differential method for an analysis of the dimensionless conductance activation energy [21] $w(T) = \partial \ln G(T)/\partial \ln T = m + x(T_0/T)^x$. In this approach, if $m \ll x(T_0/T)^x$, then $\log w(T) = A - x \log T$, and $A = x \log T_0 + \log x$. Constructing $\log w(T)$ as a function of $\log T$, one can find the exponent x from the slope of the straight line. The parameter A can be found by the intersection point of the straight line with the ordinate axis, which gives the characteristic temperature $T_0 = (10^A/x)^{1/x}$. Typical plots of $\log w(T)$ versus $\log T$ for some samples are given in Fig. 2. At $T \lesssim 10$ K, a linear relationship is observed between $\log w(T)$ and $\log T$, pointing to the fact that $m \ll x(T_0/T)^x$ at these tempera-

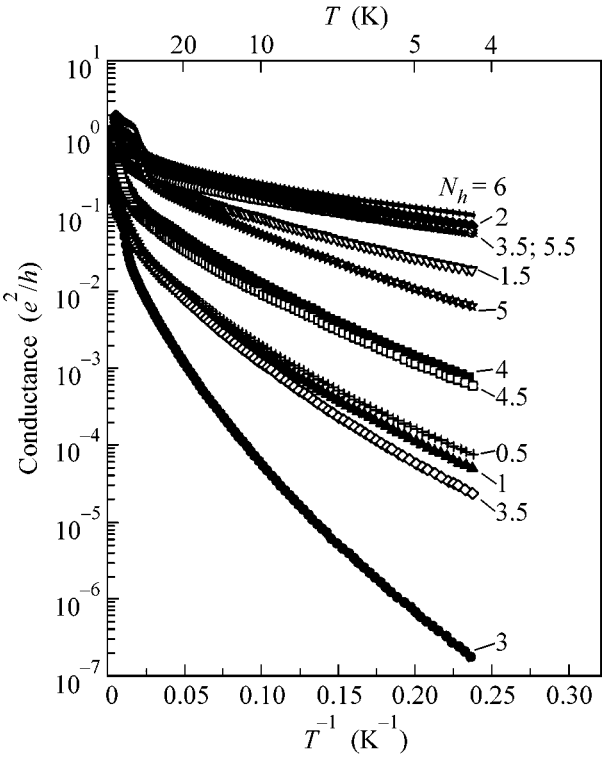

Fig. 1. Temperature dependences of the conductance in samples differing in the average number of holes per one Ge QD.

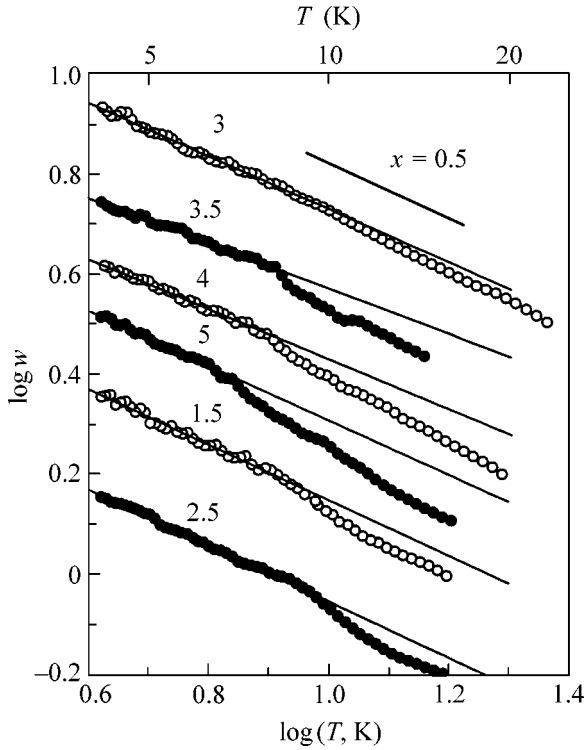

Fig. 2. Temperature dependences of the logarithmic derivative $w(T) = \partial \ln G(T)/\partial \ln T$ for samples differing in the average number of holes per one Ge QD.

tures. From the slope angle of the approximating straight lines (solid lines in Fig. 2), we found that the exponent x takes approximately the same value $x = 0.51 \pm 0.05$ for all the 12 samples in accordance with Eq. (2).

Because it was already stated that $x \simeq 0.5$, the nonlinear regression method can be used for further determining the exponent m in the region of low temperatures. With this aim, the experimental dependences $G(T)$ at $T < 10$ K were approximated by the equation $G(T) = \gamma T^m \exp[-(T_0/T)^{1/2}]$, and the parameters γ, m, and T_0 were varied until the coincidence of the calculated and experimental curves. The results of this procedure are presented in Fig. 3. Symbols correspond to experimental data, and solid lines depict calculated curves. It was found that m lies in the region $-(0.11 \pm 0.09)$ (Fig. 4a). The closeness of m to zero allows a conclusion to be made that actually the preexponential factor G_0 is virtually temperature-independent at low temperatures.

A similar approach to determining the temperature dependence $G_0(T)$ was applied to the region of high temperatures ($10 < T < 40$ K). The high-temperature exponent m in samples differing in the numbers of holes N_h is given in Fig. 4a. In order to understand the observed dependence $m(N_h)$, it is necessary to consider the structure of electron shells in Ge QDs. A numerical simulation of the hole energy spectrum and hole wave functions in pyramidal Ge nanoclusters in Si was performed by Dvurechenskii, Nenashev, and Yakimov [20]. The hole ground state has an *s*-type symmetry and is doubly degenerate by the spin direction. The first excited state possesses a *p*-type symmetry with the degree of degeneracy equal to 4. One pair is associated with the spin degree of freedom, and another one, with the equivalence of crystallographic directions along which the diagonals of the Ge pyramid base are oriented [20]. It is evident in Fig. 4a that, at the very beginning of filling each of the shells ($N_h = 0.5$ for the *s* shell and $N_h = 3$–4 for the *p* shell), $m = -(0.75 \pm 0.05)$; that is, conduction is phonon-assisted; however, at the end of filling, a considerable contribution from phononless processes arises even at high temperatures ($m \longrightarrow 0$). The most probable hypothesis that can explain this behavior is that the intensity of charge exchange between localized electron states is small when the shell is completely empty or fully filled (in the first case, there is no mobile charge, and in the second, there is no vacant places with close energy levels). Therefore, the mechanism of hopping transport stimulated by Coulomb interaction [13] is suppressed. The dependence of the effective localization radius ξ shown in Fig. 4b gives evidence in favor of this interpretation. The value of ξ was found from the relationship $T_0 = 6.2e^2/k_B\kappa\xi$ with $\kappa = 12$ for Si. In the situation of hop-

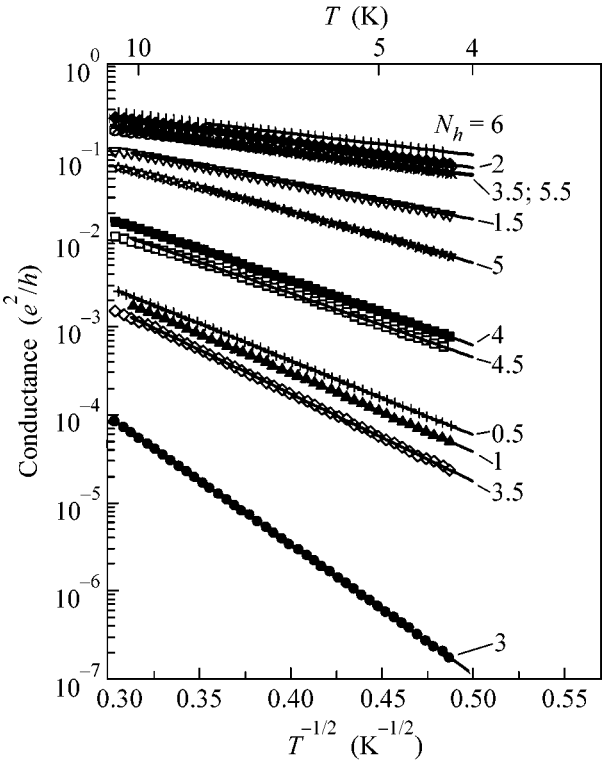

Fig. 3. Temperature dependences of the conductance constructed on the $\log G$–$T^{-1/2}$ coordinates. Symbols correspond to experimental points, solid lines are approximations of the experimental data using the equation $G(T) = \gamma T^m \exp[-(T_0/T)^{1/2}]$. T_0, γ, and m are variable parameters.

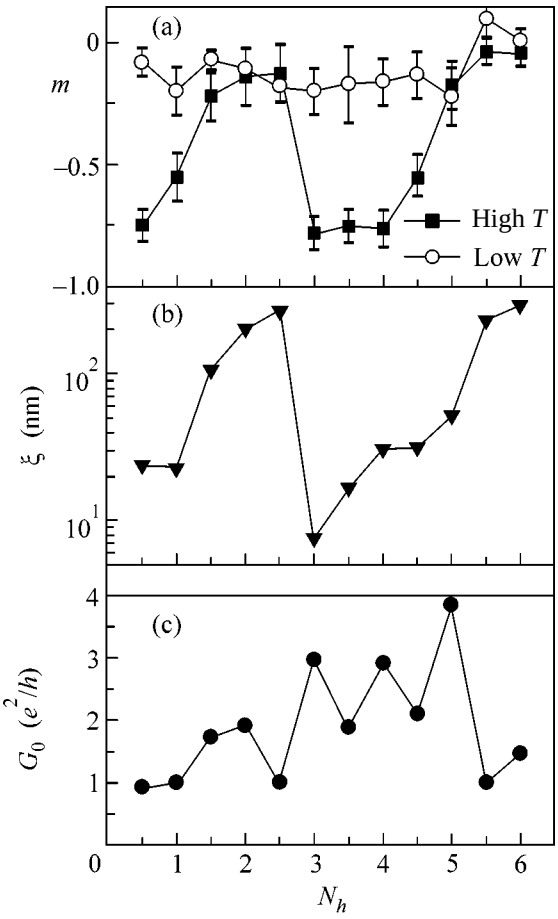

Fig. 4. Dependence of (a) the exponent m characterizing the temperature dependences of the preexponential factor G_0 in the region of high ($10 < T < 40$ K) and low ($T < 10$ K) temperatures, (b) the effective localization radius ξ, and (c) the preexponential factor G_0 at low temperatures ($T < 10$ K) on the average number of holes in QDs N_h.

ping conduction over the impurity band, ξ is as a rule nothing more nor less than the Bohr radius of the charge carrier at an impurity. In the case of QDs, when in each of them there are several bound states, electrons can pass, for example, from the ground state of one QD to the excited state of another QD. In this case, the effective localization radius reflects the spatial range of overlap between the wave functions in the initial and final states. It is evident in Fig. 4b that the lowest value of ξ is attained in a sample with $N_h = 3$. This means that the filling of the *s* shell is actually completed at these values of N_h, and holes in hopping are forced to pass into the *p* shell with a completely different electron configuration.

Let us turn back to the analysis of the preexponential factor in the region of low temperatures. The dependence $G_0(N_h)$ is presented in Fig. 4c. It turned out that the prefactor actually has a value of order e^2/h in agreement with the theory of electron–electron interaction; however, it is not constant but varies upon varying the degree N_h of filling the QD with holes, assuming values divisible by e^2/h. Currently, there is no preconceived explanation of the oscillating behavior of G_0, and further theoretical and experimental investigations into the effects of Coulomb interaction in charge-transfer processes in two-dimensional disordered systems in the strong localization regime are necessary.

In conclusion, let us make another comment. The number of phonons with a particular energy decreases with decreasing temperature. As a consequence, two alternatives arise. First, an electron is forced to hop onto a spatially more distant state with a minimum difference in energy. Second, it can make a hop onto a closer state by changing the energy of the state through the Coulomb interaction with centers with fluctuating charges. Apparently, the probability of the second process at low T is higher. For this reason, a change in hopping conduction mechanisms takes place on cooling the system.

The authors are grateful to S.D. Baranovskiĭ for useful discussions.

This work was supported by the Russian Foundation for Basic Research, project no. 03-02-16526, and the program "Universities of Russia," project no. UR.01.01.019.

REFERENCES

1. S. V. Kravchenko, W. E. Mason, G. E. Bowker, *et al.*, Phys. Rev. B **51**, 7038 (1995).
2. M. Y. Simmons, A. R. Hamilton, M. Pepper, *et al.*, Phys. Rev. Lett. **80**, 1292 (1998).
3. N. Mott, J. Non-Cryst. Solids **1**, 1 (1968).
4. B. I. Shklovskiĭ and A. L. Éfros, *Electronic Properties of Doped Semiconductors* (Nauka, Moscow, 1979; Springer, New York, 1984).
5. A. L. Efros and B. I. Shklovskii, J. Phys. C **8**, L49 (1975).
6. D. N. Tsigankov and A. L. Efros, Phys. Rev. Lett. **88**, 176602 (2002).
7. F. W. Van Keuls, X. L. Hu, H. W. Jiang, and A. J. Damm, Phys. Rev. B **56**, 1161 (1997).
8. A. I. Yakimov, A. V. Dvurechenskii, V. V. Kirienko, *et al.*, Phys. Rev. B **61**, 10868 (2000).
9. E. I. Levin, V. L. Nguen, B. I. Shklovskiĭ, and A. Éfros, Zh. Éksp. Teor. Fiz. **92**, 1499 (1987) [Sov. Phys. JETP **65**, 842 (1987)].
10. G. Ebert, K. von Klitzing, C. Probst, *et al.*, Solid State Commun. **45**, 625 (1983).
11. A. Briggs, Y. Guldner, J. P. Vieren, *et al.*, Phys. Rev. B **27**, 6549 (1983).
12. I. L. Aleiner, D. G. Polyakov, and B. I. Shklovskii, in *Proceedings of the 22nd International Conference on the Physics of Semiconductors, Vancouver, 1994*, Ed. by D. S. Lockwood (World Sci., Singapore, 1994), p. 787.
13. V. I. Kozub, S. D. Baranovskii, and I. S. Shlimak, Solid State Commun. **113**, 587 (2000).
14. W. Mason, S. V. Kravchenko, G. E. Bowker, and J. Furneaux, Phys. Rev. B **52**, 7857 (1995).
15. J. Lam, M. D'Iorio, D. Brown, and H. Lafontaine, Phys. Rev. B **56**, R12741 (1997).
16. S. I. Khondaker, I. S. Shlimak, J. T. Nicholls, *et al.*, Phys. Rev. B **59**, 4580 (1999).
17. O. P. Pchelyakov, Yu. B. Bolkhovityanov, A. V. Dvurechenskiĭ, *et al.*, Fiz. Tekh. Poluprovodn. (St. Petersburg) **34**, 1281 (2000) [Semiconductors **34**, 1229 (2000)].
18. A. I. Yakimov, A. V. Dvurechenskii, A. I. Nikiforov, *et al.*, Phys. Rev. B **67**, 125318 (2003).
19. N. P. Stepina, R. Beyer, A. I. Yakimov, *et al.*, Phys. Low-Dimens. Semicond. Struct. **11/12**, 262 (2001).
20. A. V. Dvurechenskii, A. V. Nenashev, and A. I. Yakimov, Nanotechnology **13**, 75 (2002).
21. A. G. Zabrodskiĭ and K. N. Zinov'eva, Zh. Éksp. Teor. Fiz. **86**, 727 (1984) [Sov. Phys. JETP **59**, 425 (1984)].

Translated by A. Bagatur'yants

JETP Letters, Vol. 77, No. 7, 2003, pp. 381–384. Translated from Pis'ma v Zhurnal Éksperimental'noĭ i Teoreticheskoĭ Fiziki, Vol. 77, No. 7, 2003, pp. 450–454.

Modification of the Superconducting Order Parameter Δ(k) by Long-Range Interactions

V. V. Val'kov[1, 2, 3, *] and D. M. Dzebisashvili[1, 3]

[1] *Kirenskiĭ Institute of Physics, Siberian Division, Russian Academy of Sciences, Akademgorodok, Krasnoyarsk, 660036 Russia*

**e-mail: vvv@iph.krasn.ru*

[2] *Krasnoyarsk State Technical University, Krasnoyarsk, 660074 Russia*

[3] *Krasnoyarsk State University, Krasnoyarsk, 660075 Russia*

Received December 9, 2002; in final form, February 21, 2003

It is demonstrated that the inclusion of long-range intersite interactions qualitatively modifies the dependence of a superconducting gap on quasimomentum for both *s*- and *d*-symmetry types. In particular, the order parameter of a superconducting phase with the $d_{x^2-y^2}$ symmetry type depends on two amplitudes and has the form $\Delta(\mathbf{k}) = \Delta_1(\cos k_x - \cos k_y) + \Delta_2(\cos 2k_x - \cos 2k_y)$. In this case, the theoretical dependence of the critical temperature on the degree of doping agrees with the experimental dependence. © *2003 MAIK "Nauka/Interperiodica"*.

PACS numbers: 74.20.-z

1. It is known that the (*t*–*J*) model [1] properly describes, on a qualitative level, the magnetic pairing mechanism in high-temperature superconductors (see, e.g., review [2]). If this model is developed on the basis of the Hubbard model in the strong-correlation regime, the effective Hamiltonian H_{eff} includes so-called three-center terms [3, 4]. In [5], it was shown that the three-center terms $H_{(3)}$make a weak contribution to the dispersion curves of energy spectrum. This result is quite natural, because the corrections $H_{(3)}$ to the hopping parameters contain the additional smallness. A different situation appears in the analysis of a superconducting phase. In the case of the magnetic pairing mechanism, the exchange interaction plays the role of coupling constant. The energy parameters in the three-center terms are of the same order of magnitude. For this reason, the contribution $H_{(3)}$ to the self-consistent equation for the superconducting gap becomes appreciable. The influence of three-center terms on the formation of superconductivity was studied in [6, 7]. It was shown in [7] that the inclusion of three-center terms results in the renormalization of the coupling constant. This substantially reduces the region of a superconducting phase with the $d_{x^2-y^2}$ symmetry type of order parameter [8].

Beyond the nearest-neighbor approximation, the effective Hamiltonian includes the exchange interaction between the spins of quasiparticles separated by a distance larger than the lattice parameter. The important role of quasiparticle hopping between the sites from the distant coordination spheres and the exchange interactions between the non-nearest-neighboring spins was demonstrated in many works dealing with the quasiparticle energy spectrum (see, e.g., [9–13]). In these cases, the theoretical positions agreed satisfactorily with the APRES data. In particular, it was pointed out that the inclusion of frustrated bonds ($J_2 > 0$) is important for the description of the evolution of spectral dependence in the presence of doping [12]. Since, as was mentioned above, the exchange interaction parameters play the role of coupling constants in the magnetic mechanism of superconducting pairing, one can expect that J_2 and J_3 may influence both the functional form of the order parameter and the conditions for the appearance of superconducting state.

Below, the effective Hamiltonian based on the strong-correlation Hubbard model (extended (*t*–*J*) model with three-center interactions) is used to demonstrate that the exchange interactions between the spins of non-nearest neighbors have an appreciable effect both on the quasimomentum dependence of the order parameter and on the form of the equation for the superconducting gap and critical temperature T_c.

2. The Hubbard Hamiltonian

$$H = \sum_{f\sigma}(\varepsilon - \mu)a^+_{f\sigma}a_{f\sigma} + \sum_{fm\sigma} t_{fm}a^+_{f\sigma}a_{m\sigma} + U\sum_{f\sigma}\hat{n}_{f\uparrow}\hat{n}_{f\downarrow} \quad (1)$$

is chosen as the initial model, and it is assumed that three hopping parameters are nonzero: $t_{f,\, f+\delta_1} = -t_1$,

$t_{f,\,f+\delta_2} = -t_2$, and $t_{f,\,f+\delta_3} = -t_3$, where δ_i are the radius vectors of the sites from the ith coordination sphere.

It is well known that, in the regime of strong electron correlations ($U \gg |t_{fm}|$) and for concentrations $n < 1$, one can pass, in the Hubbard operator representation, to the effective Hamiltonian of the form

$$H = \sum_{f\sigma}(\varepsilon - \mu)X_f^{\sigma\sigma} + \sum_{fm\sigma} t_{fm}X_f^{\sigma 0}X_m^{0\sigma} + \sum_{fm\sigma}\left(\frac{t_{fm}t_{mf}}{U}\right)(X_f^{\sigma\bar{\sigma}}X_m^{\bar{\sigma}\sigma} - X_f^{\sigma\sigma}X_m^{\bar{\sigma}\bar{\sigma}}) + \sum_{\substack{fmg\sigma \\ (f\neq g)}}\left(\frac{t_{fm}t_{mg}}{U}\right)(X_f^{\sigma 0}X_m^{\bar{\sigma}\sigma}X_g^{0\bar{\sigma}} - X_f^{\sigma 0}X_m^{\bar{\sigma}\bar{\sigma}}X_g^{0\sigma}) \quad (2)$$

with a quadratic accuracy in $|t_{fm}|/U$ [7, 2, 8]. The notation is standard, and its meaning can be found in the cited works and in review [2]. Note, nevertheless, that the last term in the Hamiltonian depends on three sites and describes the correlated hopping.

By using the diagram technique for the Hubbard operators [14, 15] or the method of irreducible Green's functions in the atomic representation with anomalous means [16], one arrives at the self-consistency equation for the superconducting order parameter (SOP) $\Delta_{\mathbf{q}}$ with allowance made for the three-center terms [8]:

$$\Delta_{\mathbf{k}} = \frac{1}{N}\sum_{\mathbf{q}}\left\{2t_{\mathbf{q}} + \frac{n}{2}(J_{\mathbf{k}+\mathbf{q}} + J_{\mathbf{k}-\mathbf{q}}) + 4\left(1 - \frac{n}{2}\right)\frac{t_{\mathbf{k}}t_{\mathbf{q}}}{U} - n\left(\frac{t_{\mathbf{q}}^2}{U} - \frac{J_0}{2}\right)\right\}\left(\frac{\Delta_{\mathbf{q}}}{2E_{\mathbf{q}}}\right)\tanh\left(\frac{E_{\mathbf{q}}}{2T}\right). \quad (3)$$

In this equation, t_k and J_k are the Fourier transforms of the parameters t_{fm} and $2t_{fm}^2/U$. The energy of Bogoliubov quasiparticles is denoted by $E_k = \sqrt{(\tilde{\varepsilon}_{\mathbf{k}} - \mu)^2 + |\Delta_{\mathbf{k}}|^2}$, and the renormalized electronic spectrum is

$$\tilde{\varepsilon}_{\mathbf{k}} = (1 - n/2)\left(1 - \frac{n}{2}\frac{t_{\mathbf{k}}}{U}\right)t_{\mathbf{k}} - \frac{1}{N}\times\sum_{\mathbf{q}}\left\{t_{\mathbf{q}} + \frac{n}{2}J_{\mathbf{k}-\mathbf{q}} + [(2-n)t_{\mathbf{k}} + (1-n)t_{\mathbf{q}}]\frac{t_{\mathbf{q}}}{U}\right\}n_{\mathbf{q}\sigma},$$

$$n_{\mathbf{q}\sigma} = (1 - \vartheta_{\mathbf{q}})/2 + \vartheta_{\mathbf{q}}(\exp(E_{\mathbf{q}}/T) + 1)^{-1}, \quad \vartheta_{\mathbf{q}} = \xi_{\mathbf{q}}/E_{\mathbf{q}}, \quad \xi_{\mathbf{q}} = \tilde{\varepsilon}_{\mathbf{q}} - \mu. \quad (4)$$

Note that, when deriving Eq. (3) from H_{eff}, only $\langle X_f^{0\downarrow}X_m^{0\uparrow}\rangle$ anomalous means appear. If, however, one starts from the Hamiltonian (1) written in the atomic representation, then, as was shown by Zaĭtsev *et al.* in [17], the anomalous means $\langle X_f^{0\sigma}X_m^{\sigma 2}\rangle$ and $\langle X_f^{\sigma 2}X_m^{\bar{\sigma}2}\rangle$ also appear, which are caused by the transitions from the lower to the upper Hubbard subband and the transitions inside the upper subband that make contribution at finite U. The formal absence of these anomalous means in our approach does not mean that we ignore these processes. The matter is that, when passing to H_{eff}, all calculations are carried out in the new representation, for which the indicated processes are taken into account by different operator structures. This statement can be clarified as follows.

We first consider the $\langle X_f^{02}\rangle$ and $\langle X_f^{0\sigma}X_m^{02}\rangle$ means that are associated with the transitions from the lower to upper Hubbard subband (in this case, it is tacitly assumed that the representation is induced by the original Hamiltonian). The transition to H_{eff} implies the unitary transformation ($S^+ = -S$)

$$H \longrightarrow H_{\text{eff}} = \exp(S)H\exp(-S); \quad H|\Psi_n\rangle = E_n|\Psi_n\rangle,$$

$$H_{\text{eff}}|\Phi_n\rangle = E_n|\Phi_n\rangle, \quad |\Phi_n\rangle = \exp(S)|\Psi_n\rangle,$$

after which the Hamiltonian, the basis functions, and all operators, whose averaging gives the physical quantities of interest, change their form. For example, the operators X_f^{02} and $X_f^{0\sigma}X_m^{\sigma 2}$ are transformed as

$$X_f^{02} \longrightarrow \tilde{X}_f^{02} = -\sum_g (t_{fg}/U)(X_f^{0\downarrow}X_g^{0\uparrow} - X_f^{0\uparrow}X_g^{0\downarrow}) + O\{(t_{fg}/U)^3\},$$

$$X_f^{0\sigma}X_m^{\sigma 2} \longrightarrow \tilde{X}_f^{0\sigma}\tilde{X}_m^{\sigma 2} = -\sum_g (t_{mg}/U)\eta(\sigma) \times (X_f^{0\sigma}X_m^{\sigma\bar{\sigma}}X_g^{0\sigma} - X_f^{0\sigma}X_m^{\sigma\sigma}X_g^{0\bar{\sigma}}) + O\{(t_{fm}/U)^3\}.$$

The transformation laws clearly demonstrate that, in the new representation, the above-mentioned anomalous means are not ignored within the linear accuracy in (t_{fm}/U), and their contribution is determined by the means of operators which are responsible only for the transitions between the states without pairs. In essence, this is a particular case that follows from the general statement made in [18]. As for the anomalous means associated with the transitions inside the upper Hubbard band, one can readily verify that the corresponding contribution is nonzero only in the quadratic (and not linear) approximation in (t_{fm}/U). For this reason, these means make no contribution to our theory.

As known, Eq. (3) has solutions differing in the type of $\Delta_{\mathbf{k}}$ symmetry. We will consider the influence of long-range hopping separately on the type of SOP symmetry and on the $\mathbf{k}$ dependence for a given symmetry.

(a) *s* Symmetry; due to the presence of three nonzero t_1, t_2, $t_3 \neq 0$, the solution to Eq. (3) for this symmetry type is given by $\Delta_\mathbf{k}$, which is expressed as

$$\Delta_\mathbf{k} = \Delta_0 + \Delta_1 S_1(\mathbf{k}) + \Delta_2 S_2(\mathbf{k}) + \Delta_3 S_3(\mathbf{k}). \quad (5)$$

Hereafter, the following invariants are used for brevity:

$$S_1(\mathbf{k}) = (\cos k_x a + \cos k_y a)/2,$$
$$S_2(\mathbf{k}) = \cos(k_x a)\cos(k_y a),$$
$$S_3(\mathbf{k}) = (\cos 2k_x a + \cos 2k_y a)/2.$$

The order parameter in the form of Eq. (5) is the solution to the integral Eq. (3), if the unknown coefficients Δ_i satisfy the set of four equations

$$\Delta_0 = \sum_{l=0}^{3}\left\{\sum_{j=1}^{3} 2G_{lj}T_j + \left(\frac{n}{2}\right)J_0 G_l - \frac{n}{U}\sum_{i,j=1}^{3} G_{lij}T_i T_j\right\}\Delta_l$$
$$(T_j = -4t_j, \quad j = 1, 2, 3),$$
$$\Delta_m = 4\sum_{l=0}^{3}\left\{nJ_m G_{ml} + (1-n/2)T_m\sum_{i=1}^{3} G_{li}T_i/U\right\}\Delta_l, \quad (6)$$
$$J_m = 2t_m^2/U, \quad m = 1, 2, 3,$$

where

$$G_i = G_{i00}, \quad G_{ij} = G_{ij0},$$
$$G_{ijl} = \frac{1}{N}\sum_{\mathbf{q}} S_i(\mathbf{q})S_j(\mathbf{q})S_l(\mathbf{q})\Psi_\mathbf{q},$$
$$\Psi_\mathbf{q} = \frac{\tanh(E_\mathbf{q}/2T)}{2E_\mathbf{q}}, \quad S_0(\mathbf{k}) = 1.$$

From the set of Eqs. (6) it follows that, in the limit of infinitely strong repulsion, for which the superconducting pairing is governed only by the Zaĭtsev kinematic mechanism, the order parameter includes only the contributions linear in *t*;

(b) d_{xy} symmetry; $\Delta_\mathbf{k} = \Delta_1 \sin(k_x a)\sin(k_y a)$ This symmetry type is absent for the SOP in the nearest-neighbor approximation and appears only if $t_2 \neq 0$. The corresponding SOP amplitude Δ_1 is found from the transcendental equation

$$1 = (4nJ_2/N)\sum_{\mathbf{q}} \sin^2 q_x \sin^2 q_y \Psi_\mathbf{q}; \quad (7)$$

(c) $d_{x^2-y^2}$ symmetry. Due to the distant hopping (t_2, $t_3 \neq 0$), the well-known SOP $\Delta_\mathbf{k} = \Delta_0(\cos(k_x a) - \cos(k_y a))$ is impossible, because it does not satisfy the integral Eq. (3). The solution to this equation can be represented in a two-parameter form

$$\Delta_\mathbf{k} = \Delta_1\varphi_1(\mathbf{k}) + \Delta_2\varphi_2(\mathbf{k}),$$
$$\varphi_l(\mathbf{k}) = (\cos(lk_x a) - \cos(lk_y a)), \quad l = 1, 2, \quad (8)$$

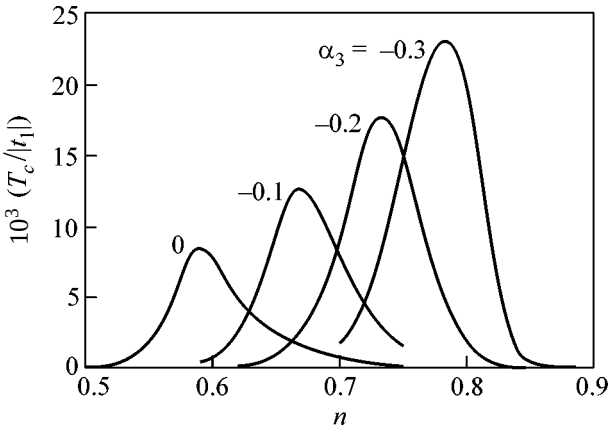

Fig. 1. Effect of hopping to the third coordination sphere on the concentration dependence of T_c for different $\alpha_3 = t_3/t_1$. Parameters: $t_2/t_1 = -0.2$ and $|t_1|/U = 0.2$.

if the amplitudes Δ_1 and Δ_2 are the solutions to the following two equations:

$$\Delta_i = \lambda_i\sum_{j=1}^{j=2}\Phi_{ij}\Delta_j; \quad \lambda_1 = n\left(\frac{t_1^2}{U}\right), \quad \lambda_2 = n\left(\frac{t_3^2}{U}\right),$$
$$\Phi_{nm} = \frac{1}{N}\sum_{\mathbf{q}}\varphi_n(\mathbf{q})\varphi_m(\mathbf{q})\tanh\left(\frac{E_\mathbf{q}}{2T}\right). \quad (9)$$

It follows that, for $t_3 \neq 0$, $\Delta_1$is always nonzero. The condition for the compatibility of this set of equations leads to the equation

$$(1-\lambda_1\Phi_{11})(1-\lambda_2\Phi_{22}) = \lambda_1\lambda_2\Phi_{12}^2, \quad (10)$$

which determines, in particular, the critical temperature. One can see that the well-known equation for the critical temperature in the (t–J*) model is obtained only for $t_3 = 0$.

3. Because of the lack of volume, we only present the results of numerical analysis for the influence of distant hopping on the characteristics of superconducting state for $\Delta_\mathbf{k}$ of the $d_{x^2-y^2}$-type symmetry. Figure 1 shows the concentration dependence of the transition temperature to the $d_{x^2-y^2}$ phase with inclusion of the parameter t_3. One can see that the electron hopping from the third coordination sphere exerts a substantial effect on the position of the maximum of the $T_c(n)$ curve. It is notable that the experimentally observed situation with a T_c maximum at $n \sim 0.8$ can easily be realized. Curves *1* and *2* in Fig. 2 demonstrate the effect of modified Eq. (10) with long-range interactions on the critical temperature. Curve *1* is constructed using the solution to the complete Eq. (10), and curve *2* is obtained on the assumption that $\lambda_2 = 0$.

In the superconducting phase ($T < T_c$), the amplitudes Δ_1 and Δ_2 are nonzero and change synchronously

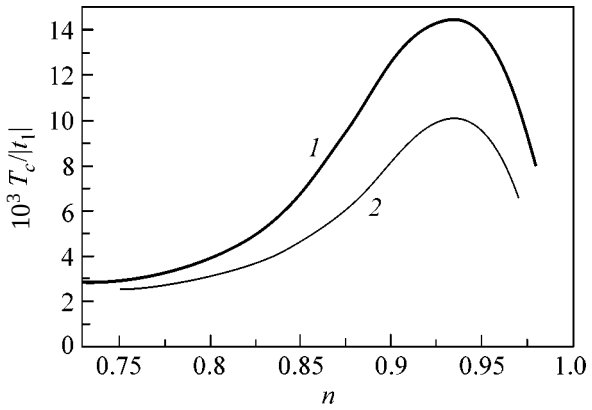

Fig. 2. Concentration dependence $T_c(n)$: $t_2/t_1 = 0.4$, $t_3/t_1 = 0.3$, and $|t_1|/U = 0.2$. For the values for curves *1* and *2*, see the text.

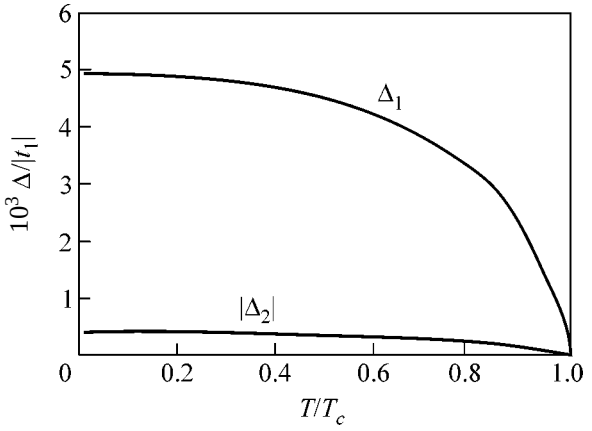

Fig. 3. Temperature dependence of the amplitudes Δ_1 and $|\Delta_2|$ for $n = 0.84$. Parameters are as in Fig. 2.

with temperature. An example of the behavior of this type is demonstrated in Fig. 3. One can see that, over the entire temperature range where the superconducting solution occurs, the temperature of $|\Delta_2|$ ($\Delta_2 < 0$) is the same as for Δ_1.

Note in conclusion that the effect of long-range hopping both on the occurrence of superconducting state and on the momentum dependence of the order parameter has been demonstrated in this work by the example of effective Hamiltonian obtained from the Hubbard model in the strong electron-correlation regime. In this case, there is a correspondence between t_3 and exchange parameter J_3. Nevertheless, a situation is often considered where the hopping parameters and the exchange constants are thought to be independent. In this case, a situation can in principle be realized where the magnitude of long-range exchange interactions will not be related to the hopping amplitudes.

It is worth noting that the more general results could be obtained using the original Hamiltonian (1), if the set of four equations is written in the form as it was done by Zaĭtsev *et al.* in [17]. However, if one is interested in the leading approximation with respect to (t_{fm}/U), the variant presented in this work is simpler. It is this fact that allows the influence of the long-range hopping on the possible symmetry type of order parameter and on the modification of the quasimomentum dependence to be analyzed for any symmetry type.

This work was supported by the Russian Foundation for Basic Research + KKFN "Eniseĭ" (project no. 02-02-97705) and the program "Quantum Macrophysics" of the Presidium of the Russian Academy of Sciences. One of us (D.M.D.) is grateful to the Foundation for the Assistance of the Native Science and Siberian Division of the Russian Academy of Sciences (Lavrent'ev Competition of Youth Projects).

REFERENCES

1. P. W. Anderson, Science **235**, 1196 (1987).
2. Yu. A. Izyumov, Usp. Fiz. Nauk **167**, 465 (1997) [Phys. Usp. **40**, 445 (1997)].
3. L. P. Bulaevskiĭ, É. L. Nagaev, and D. L. Khomskiĭ, Zh. Éksp. Teor. Fiz. **54**, 1562 (1968) [Sov. Phys. JETP **27**, 836 (1968)].
4. K. A. Chao, J. Spalek, and A. M. Oles, J. Phys. C **10**, L271 (1977).
5. V. Yu. Yushankhay, V. S. Oudovehko, and R. Hayn, Phys. Rev. B **55**, 15562 (1997).
6. J. E. Hirsch, Phys. Lett. A **136**, 163 (1989).
7. V. Yu. Yushankhay, G. M. Vujicic, and R. B. Zakula, Phys. Lett. A **151**, 254 (1990).
8. V. V. Val'kov, T. A. Val'kova, D. M. Dzebisashvili, and S. G. Ovchinnikov, Pis'ma Zh. Éksp. Teor. Fiz. **75**, 450 (2002) [JETP Lett. **75**, 378 (2002)].
9. A. Nazarenko, K. J. E. Vos, S. Haas, *et al.*, Phys. Rev. B **51**, 8676 (1995).
10. O. P. Sushkov, G. A. Sawatzky, R. Eder, and H. Eskes, Phys. Rev. B **56**, 11769 (1997).
11. A. F. Barabanov, O. V. Urazaev, A. A. Kovalev, and L. A. Maksimov, Pis'ma Zh. Éksp. Teor. Fiz. **68**, 386 (1998) [JETP Lett. **68**, 412 (1998)].
12. R. Hayn, A. F. Barabanov, J. Schulenburg, and J. Richter, Phys. Rev. B **53**, 11714 (1996).
13. T. Tohyama and S. Maekawa, Supercond. Sci. Technol. **13**, R17 (2000).
14. R. O. Zaĭtsev, Zh. Éksp. Teor. Fiz. **70**, 1100 (1976) [Sov. Phys. JETP **43**, 574 (1976)].
15. R. O. Zaĭtsev and V. A. Ivanov, Pis'ma Zh. Éksp. Teor. Fiz. **46** (S1), 140 (1987) [JETP Lett. **46**, S116 (1987)].
16. N. M. Plakida, V. Yu. Yushankhay, and I. V. Stasyuk, Physica C (Amsterdam) **162–164**, 787 (1989).
17. R. O. Zaĭtsev, V. A. Ivanov, and Yu. V. Mikhaĭlova, Fiz. Met. Metalloved. **68**, 1108 (1989).
18. N. N. Bogolyubov, *Selected Papers* (Naukova Dumka, Kiev, 1970), Vol. 2, p. 423.

Translated by V. Sakun

JETP Letters, Vol. 77, No. 7, 2003, pp. 385–388. Translated from Pis'ma v Zhurnal Éksperimental'noĭ i Teoreticheskoĭ Fiziki, Vol. 77, No. 7, 2003, pp. 455–458.

Multiphonon Ionization of Deep Centers in Amorphous Silicon Nitride: Experiment and Numerical Simulations

K. A. Nasyrov*, Yu. N. Novikov, V. A. Gritsenko**, S. Y. Yoon***, and C. W. Kim*****

* *Institute of Automatics and Electrometry, Siberian Division, Russian Academy of Sciences, Novosibirsk, 630090 Russia*

** *Institute of Semiconductor Physics, Siberian Division, Russian Academy of Sciences, Novosibirsk, 630090 Russia*

e-mail: grits@isp.nsc.ru

*** *Samsung Advanced Institute of Technology, Suwon, 440-600 Korea*

Received March 3, 2003

The conductivity of amorphous silicon nitride has been studied experimentally in a wide range of electric fields and temperatures. The experimental results are in a quantitative agreement with the theory of multiphonon ionization of deep centers for the bipolar model of conductivity. The best agreement between experiment and the calculation has been obtained for the same parameters of deep electron and hole centers. © *2003 MAIK "Nauka/Interperiodica".*

PACS numbers: 77.22.-d; 77.84.Bw

The majority of amorphous dielectrics, such as Si_3N_4, Ce_3N_4, BN, Ta_2O_5, HfO_2, Y_3O_3, and TiO_2, contain a high density of deep centers (traps). The conductivity of such dielectrics in strong electric fields (10^6–10^7 V/cm) is limited by the ionization of deep centers. Silicon nitride is the dielectric that is most comprehensively studied from the viewpoint of the mechanism of charge transfer.

Amorphous silicon nitride (Si_3N_4) is characterized by a high density (>10^{19} cm^{-3}) of electron and hole traps with a giant confinement time of electrons and holes in a localized state (>10 years at 300 K) [1]. Currently, it is commonly accepted that the ionization of deep centers in Si_3N_4 is confined to the Frenkel effect [2–5]. However, it was demonstrated in [4–8] that the interpretation of Si_3N_4 conductivity within the Frenkel model gives an anomalously small value of the frequency factor $\nu \approx 10^6$–10^9 s^{-1}. The frequency factor was estimated in the original paper by Frenkel at a level of $\nu \approx 10^{15}$ s^{-1} [9]. Moreover, the formal agreement with the modified Frenkel model that takes into account tunnel ionization can be obtained only at an anomalously large value of the effective tunneling mass $m^* = 4m_e$ [8]. At the same time, experiment gives a value of the effective tunneling mass in silicon nitride close to $m^* = 0.4m_e$ [10]. As distinct from dielectrics, the ionization of deep centers in semiconductors is interpreted within the theory of multiphonon ionization [11].

In [8], experimental results on the conductivity of metal nitride–oxide–semiconductor (MNOS) structures were quantitatively compared with the theory of multiphonon ionization for the unipolar model of conductivity, which takes into account only electron injection from silicon and does not take into account hole injection from the metal; see Fig. 1a. On the other hand, in this work experimental results are compared with the more general bipolar model, in which the injection of electrons from silicon, the injection of holes from the metal, and the recombination of free electrons with localized holes and free holes with localized electrons are taken into account; see Fig. 1b. The goal of this work is to experimentally study the mechanism of charge transfer in Si_3N_4 over a wide range of temperatures and fields and to quantitatively compare the experiment with the calculation based on the bipolar

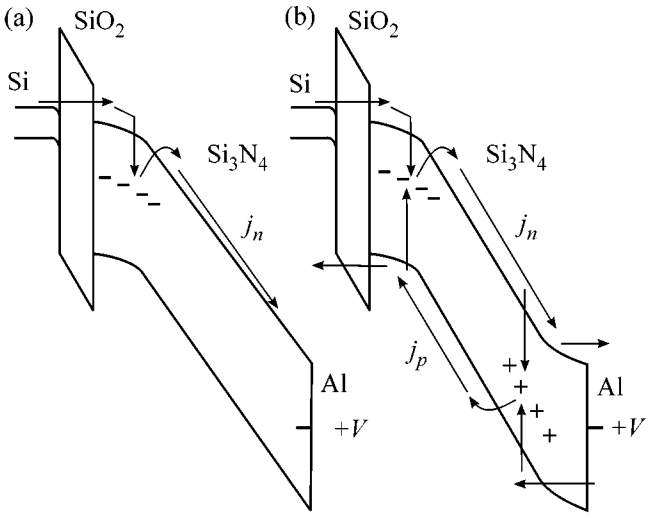

Fig. 1. Energy diagram for (a) unipolar and (b) bipolar models of conductivity for an MNOS structure at a positive voltage on an aluminum electrode. Symbols (–) and (+) mark respectively electrons and holes captured by a trap.

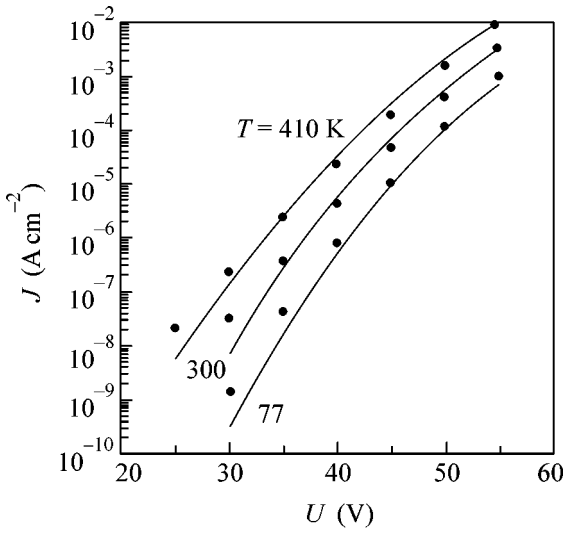

Fig. 2. Experimental (dots) and calculated (solid lines) current–voltage characteristics for the model of the multiphonon ionization of traps in Si_3N_4 at a positive voltage on an aluminum electrode. The calculation was carried out for the same parameters of electron and hole traps $\sigma^e = \sigma^h = \sigma_r = 5 \times 10^{-13}$ cm^2, $W_t^e = W_t^h = W_t = 1.7$ eV, $W_{opt}^e = W_{opt}^h = W_{opt} = 2.7$ eV, $W_{ph}^e = W_{ph}^h = W_{ph} = 0.045$ eV, and $N_t^e = N_t^h = N_t = 7 \times 10^{19}$ cm^{-3}.

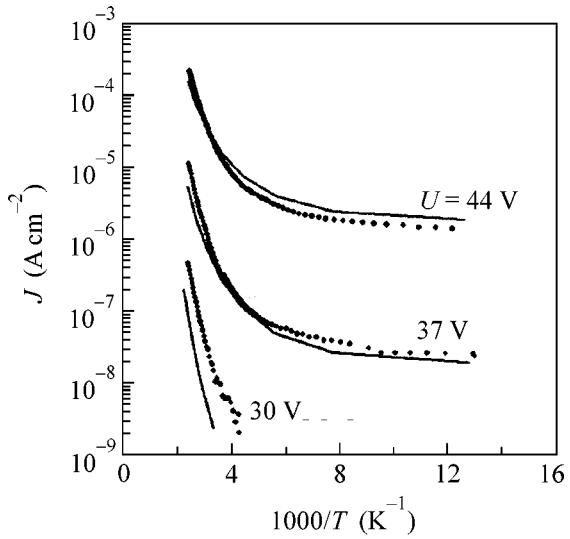

Fig. 3. Experimental (dots) and calculated (solid lines) temperature dependences of the current for the model of the multiphonon ionization of traps for a positive voltage on an aluminum electrode. The calculation was carried out for the same parameters of electron and hole traps $\sigma^e = \sigma^h = \sigma_r = 5 \times 10^{-13}$ cm^2, $W_t^e = W_t^h = W_t = 1.7$ eV, $W_{opt}^e = W_{opt}^h = W_{opt} = 2.7$ eV, $W_{ph}^e = W_{ph}^h = W_{ph} = 0.045$ eV, and $N_t^e = N_t^h = N_t = 7 \times 10^{19}$ cm^{-3}.

conductivity model and the multiphonon mechanism of trap ionization in silicon nitride.

Samples of MNOS structures were manufactured on a *p*-type silicon substrate with a resistivity of 20 Ω cm grown using the Czochralski method. A thin, tunnel-transparent oxide layer 18-Å thick was grown at a temperature of 760°C. Silicon nitride 670-Å thick was obtained at a temperature of 700°C by the deposition method in a low-pressure reactor. The SiH_2Cl_2/NH_3 ratio was 0.1. Aluminum electrodes with an area of 5×10^{-3} cm^2 were sputtered through a mask.

Current–voltage characteristics (Fig. 2) were measured experimentally at different temperatures, and temperature dependences of the current (Fig. 3) were measured for different voltages. The experimental dependences were obtained in a cryostat cooled by liquid nitrogen with controlled temperature in the range 77–450 K. The current–voltage characteristics were measured with voltage varied at a rate of 0.02 V/s. The heating rate of samples was ~5 K/min. All the measurements were carried out for positive voltages on the gate. At this voltage polarity, both the injection of electrons from the silicon substrate and the injection of holes from aluminum take place.

A one-dimensional bipolar model of Si_3N_4 conductivity was used for comparison with experiment. Previously, this model was used in [12]. Charge transfer was described with the use of the Shockley–Read–Hall equation and the Poisson equation taking into account the nonuniform electric field distribution in silicon nitride

$$\frac{\partial n(x,t)}{\partial t} = \frac{1}{e}\frac{\partial j(x,t)}{\partial x} - \sigma^e \nu n(x,t)(N_t^e - n_t(x,t)) + n_t(x,t)P(x,t) - \sigma_r \nu n(x,t) p_t(x,t), \quad (1)$$

$$\frac{\partial n_t(x,t)}{\partial t} = \sigma^e \nu n(x,t)(N_t^e - n_t(x,t)) - n_t(x,t)P(x,t) - \sigma_r \nu n(x,t) n_t(x,t), \quad (2)$$

$$\frac{\partial p(x,t)}{\partial t} = \frac{1}{e}\frac{\partial j_p(x,t)}{\partial x} - \sigma^h \nu p(x,t)(N_t^h - p_t(x,t)) + p_t(x,t)P(x,t) - \sigma_r \nu p(x,t) n_t(x,t), \quad (3)$$

$$\frac{\partial p_t(x,t)}{\partial t} = \sigma^h \nu p(x,t)(N_t^h - p_t(x,t)) - p_t(x,t)P(x,t) - \sigma_r \nu p(x,t) n_t(x,t), \quad (4)$$

$$\frac{\partial F}{\partial x} = -e\frac{(n_t(x,t) - p_t(x,t))}{\varepsilon\varepsilon_0}. \quad (5)$$

Here, n and n_t are the concentrations of free and trapped electrons, p and p_t are respectively the concentrations of free and trapped holes, N_t^e and N_t^h are the concentra-

tions of electron and hole traps, $F(x, t)$ is the local electric field, e is the electron charge, $\sigma^{e,h}$ is the capture cross section of a trap, σ_r is the recombination cross section between free and trapped carriers of opposite sign, v is the drift velocity, and $\varepsilon = 7.5$ is the low-frequency permittivity of Si_3N_4. The following values were used in this work for the capture and recombination cross sections $\sigma^e = \sigma^h = \sigma_r = 5 \times 10^{-13}$ cm^2 [6, 7, 13]. The drift velocity of electrons is related to the current density by the equation $j = env$. The multiphonon ionization model [11, 14] was used for the ionization probability P of a trap in Si_3N_4

$$P = \frac{eF}{2\sqrt{2m^* W_{\text{opt}}}} \exp\left(-\frac{4}{3}\frac{\sqrt{2m}}{\hbar eF} W_{\text{opt}}^{3/2} + 4\frac{m^*}{\hbar^2}\frac{W_{\text{ph}}}{F^2} W_{\text{opt}}(W_{\text{opt}} - W_t)\coth\frac{W_{\text{ph}}}{2T}\right), \quad (6)$$

where W_{opt} and W_t are the optical and thermal ionization energies of a trap, W_{ph} is the phonon energy, m^* is the effective mass of a carrier. The same effective masses equal to $0.5m_0$ (where m_0 is the free electron mass) were chosen in modeling for electrons and holes. The electron and hole injection from the silicon substrate and aluminum electrode, respectively, was calculated based on the Fowler–Nordheim mechanism.

We carried out two series of experiments, in one of which the current–voltage characteristic was recorded at a fixed sample temperature, and the temperature dependence of the current through the MNOS was recorded in the second series at a constant applied voltage. The current–voltage characteristics (Fig. 2) were measured at temperatures $T = 77$, 300, and 410 K in the voltage range 30–55 V, which corresponds to average electric fields of ~$(4–8) \times 10^6$ V/cm in silicon nitride. It is evident in the figure that the current increases exponentially with increasing voltage on the aluminum electrode.

The temperature dependences of the current were measured in the temperature range 77–410 K for voltages of 44, 37, and 30 V and were plotted on the Arrhenius coordinates $\ln(j) - T^{-1}$ (Fig. 3). The figure demonstrates that the current weakly depends on the temperature at $T < 200$ K. The weak temperature dependence of the current points to the tunneling mechanism of trap ionization. The same behavior of the measured currents with temperature was observed previously in [2, 3].

The direct tunneling of carriers through the triangular barrier without the participation of phonons is the main mechanism of trap ionization at low temperatures. The ionization probability in the presence of an electric field is given by the equation [15]

$$P = \frac{eF}{2\sqrt{2m^* W_{\text{opt}}}} \exp\left(-\frac{4}{3}\frac{\sqrt{2m^*}}{\hbar eF} W_{\text{opt}}^{3/2}\right). \quad (7)$$

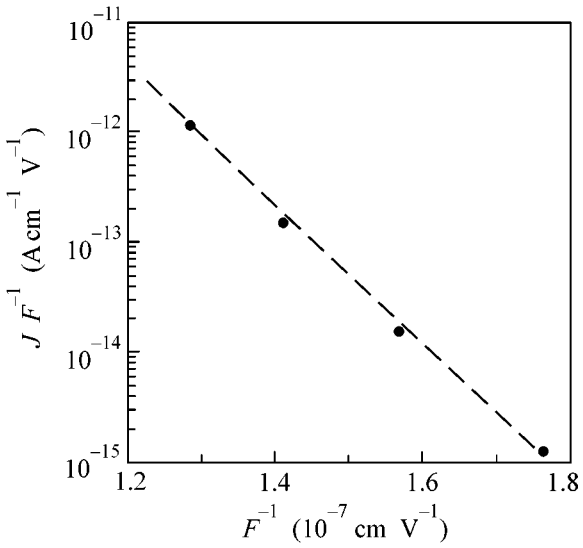

Fig. 4. Experimental dependence j/F versus $1/F$ for the temperature $T = 77$ K constructed on a semilogarithmic scale.

The lowest field F_{min} necessary for such tunneling is determined from the relationship

$$F_{\text{min}} = \frac{2\omega\sqrt{2m^* W_{\text{ph}}}}{e}, \quad (8)$$

where ω is the frequency of the trap "nucleus," which can be estimated from the relationship $\omega \approx W_{\text{ph}}/\hbar$. The estimation gives $F_{\text{min}} = 5 \times 10^6$ V/cm.

The experimental current–voltage characteristic constructed on the $\ln(j/F)$–$1/F$ coordinates for the temperature $T = 77$ K and electric fields higher than 5×10^6 V/cm is shown in Fig. 4. The average field $F = V/d$ (V is voltage, and d is the nitride thickness) is plotted in Fig. 4. On these coordinates, the rectification of the experimental curve is observed. The optical energy of the trap $W_{\text{opt}} = 2.5$ eV was estimated by the slope of the curve for $m^* = 0.5$.

It was found that the best agreement with the experiment is obtained for the same parameters of electron and hole traps: $W_t^e = W_t^h = W_t = 1.7$ eV, $W_{\text{opt}}^e = W_{\text{opt}}^h = W_{\text{opt}} = 2.7$ eV, $W_{\text{ph}}^e = W_{\text{ph}}^h = W_{\text{ph}} = 0.045$ eV, and $N_t^e = N_t^h = N_t = 7 \times 10^{19}$ cm^{-3}. The current–voltage characteristics calculated for temperatures of 77, 300, and 410 K are shown in Fig. 2 (solid lines), and temperature dependences of the current for voltages U (44, 37, and 30 V) on the aluminum electrode are shown in Fig. 3 (solid lines). The largest discrepancy between the calculated and experimental data was observed for voltages less than 35 V. This discrepancy can be explained by slow current relaxation in silicon nitride, whose nature remains unclarified [16]. The value $W_{\text{opt}} = 2.5$ eV estimated by the slope of the current–voltage characteristic (Fig. 4) turned out to be smaller than the value

W_{opt} = 2.7 eV obtained from an accurate simulation of the experiment (Figs. 2, 3). This small discrepancy can be explained by the fact that the ionization probability of a trap was estimated with the use of the average value of the electric field ($F = V/d$) in the first case and with the use of the local (depending on the coordinate) electric field obtained as an accurate solution of the Poisson equation taking into account the nonuniformity of the trapped charge in the bulk of silicon nitride in the second case.

Thus, the experiment on charge transfer in silicon nitride carried out over a wide range of electric fields and temperatures is quantitatively described by the theory of the multiphonon ionization of traps. An agreement with the experiment was obtained for the bipolar model of conductivity with the same parameters (concentration, capture cross section, and optical and thermal ionization energies) of electron and hole traps in silicon nitride.

The large difference found between the thermal and optical ionization energies within the theory of multiphonon ionization is evidently due to the occurrence of a strong polaron effect in Si_3N_4. Previously, the polaron model of electron and hole traps in Si_3N_4 was discussed in [1, 17, 18]. According to this model, electrons and holes in Si_3N_4 are captured by a minimal silicon cluster, namely, a Si–Si bond. The polaron model suggests that a Si–Si bond or a silicon cluster composed of several silicon atoms is a deep center for electrons, a deep center for holes, and a recombination center. A quantum-chemical simulation of a Si–Si bond in Si_3N_4 carried out in [19] qualitatively confirms this hypothesis.

This work was supported by the National Program of the Korean Ministry of Science and Technology on Terabit-Scale Nanoelectronics and by the Siberian Branch of the Russian Academy of Sciences, integration project no. 116.

REFERENCES

1. V. A. Gritsenko, *Atomic and Electronic Structure of Amorphous Insulators in Silicon MIS Devices* (Nauka, Novosibirsk, 1993).
2. S. M. Sze, J. Appl. Phys. **18**, 2951 (1967).
3. V. A. Gritsenko and A. V. Rzhanov, Zh. Tekh. Fiz. **46**, 2155 (1976) [Sov. Phys. Tech. Phys. **21**, 1263 (1976)].
4. R. A. Williams and M. M. E. Beguwala, IEEE Trans. Electron Devices **25**, 1019 (1978).
5. S. Manzini, J. Appl. Phys. **62**, 3278 (1987).
6. V. A. Gritsenko, E. E. Meerson, I. V. Travkov, *et al.*, Mikroélektronika **16** (1), 42 (1987).
7. H. Bachhofer, H. Reisinger, E. Bertagnolli, *et al.*, J. Appl. Phys. **89**, 2791 (2001).
8. K. A. Nasyrov, V. A. Gritsenko, M. K. Kirn, *et al.*, IEEE Electron Device Lett. **23**, 336 (2002).
9. Ya. I. Frenkel', Zh. Éksp. Teor. Fiz. **8**, 1292 (1938).
10. V. A. Gritsenko, E. E. Meerson, and Yu. N. Morokov, Phys. Rev. B **57**, R2081 (1998).
11. V. N. Abakumov, V. I. Perel', and I. N. Yassievich, *Nonradiative Recombination in Semiconductors* (S.-Peterb. Inst. Yad. Fiz. Ross. Akad. Nauk, St. Petersburg, 1997).
12. G. V. Gadiyak, M. S. Obrekht, and S. P. Sinitsa, Mikroélektronika **14**, 512 (1985).
13. F. L. Hampton and J. R. Cricchi, Appl. Phys. Lett. **35**, 802 (1979).
14. S. S. Makram-Ebeid and M. Lannoo, Phys. Rev. B **25**, 6406 (1982).
15. S. D. Ganichev, I. N. Yassievich, and V. Prettl, Fiz. Tverd. Tela (St. Petersburg) **39**, 1905 (1997) [Phys. Solid State **39**, 1703 (1997)].
16. V. A. Gritsenko, E. E. Meerson, and S. P. Sinitsa, Phys. Status Solidi A **48**, 31 (1978).
17. V. A. Gritsenko and P. A. Pundur, Fiz. Tverd. Tela (Leningrad) **28**, 3239 (1986) [Sov. Phys. Solid State **28**, 1829 (1986)].
18. P. A. Pundur, J. G. Shvalgin, and V. A. Gritsenko, Phys. Status Solidi A **94**, K701 (1986).
19. V. A. Gritsenko, H. Wong, J. B. Xu, *et al.*, J. Appl. Phys. **86**, 3234 (1999).

Translated by A. Bagatur'yants

JETP Letters, Vol. 77, No. 7, 2003, pp. 389–392. Translated from Pis'ma v Zhurnal Éksperimental'noĭ i Teoreticheskoĭ Fiziki, Vol. 77, No. 7, 2003, pp. 459–463.

Millisecond Photoluminescence Kinetics in a System of Direct-Bandgap InAs Quantum Dots in an AlAs Matrix

T. S. Shamirzaev*, A. M. Gilinsky*, A. K. Bakarov*, A. I. Toropov*, D. A. Ténné*, K. S. Zhuravlev*, C. von Borczyskowski, and D. R. T. Zahn****

** Institute of Semiconductor Physics, Siberian Division, Russian Academy of Sciences, Novosibirsk, 630090 Russia*
e-mail: timur@thermo.isp.nsc.ru
*** Institut für Physik, TU Chemnitz, D-09107 Chemnitz, Germany*
Received March 4, 2003

Anomalously long millisecond kinetics of photoluminescence (PL) is observed at low temperatures (4.2–50 K) in direct-bandgap InAs quantum dots formed in an AlAs matrix. An increase in temperature leads to a decrease in the duration of PL decay down to several nanoseconds at 300 K, whereas the integral PL intensity remains constant up to 210 K. In order to explain the experimental results, a model is proposed that takes into account the singlet–triplet splitting of exciton levels in small quantum dots. © *2003 MAIK "Nauka/Interperiodica".*

PACS numbers: 78.55.Cr; 78.67.Hc

The relaxation and recombination of excitons in self-assembling InAs quantum dots have been actively studied in recent years, because this system is promising for creating high-performance light-emitting devices [1]. Most attention has been concentrated on quantum dots formed in a GaAs matrix [2, 3]. It has been stated that the radiative recombination time of excitons in this system comprises several nanoseconds [2]. At the same time, the recombination dynamics of excitons in a system of InAs quantum dots formed in a wide-bandgap AlAs matrix has remained poorly understood. Only one work devoted to studying the transient photoluminescence (PL) of InAs quantum dots in an AlAs matrix has been published to date [4], whose authors note that photoluminescence in this system at liquid-helium temperature demonstrates microsecond decay times.

This work is devoted to studying the temperature dependence of the transient and steady-state PL of InAs quantum dots formed in an AlAs matrix. We have shown for the first time that the radiative recombination of excitons at low temperatures (4.2–50 K) is characterized in this system by an anomalously long, millisecond decay time. With increasing temperature, the duration of PL decay decreases by five orders of magnitude, reaching several nanoseconds at 300 K. The experimental results have been explained within a model taking into account the singlet–triplet splitting of exciton levels in small quantum dots arranged in a system of closely packed quantum dots with local coupling between dots.

Structures with self-assembled InAs quantum dots in an AlAs matrix were grown by molecular-beam epitaxy on semi-insulating GaAs substrates with (100) orientation using a Riber-32P setup. Samples consisted of five layers of InAs quantum dots separated with AlAs layers 8-nm thick. The amount of InAs deposited in the growth of each layer with quantum dots was equivalent to two monolayers. The layers with quantum dots were grown at a temperature of 480°C. A detailed description of the growth process is given in [5]. The sizes of quantum dots were estimated by electronic images of cross sections of samples and varied from 60 to 240 Å in the plane perpendicular to the growth direction and from 20 to 60 Å in the growth direction. As distinct from InAs quantum dots in a GaAs matrix, InAs quantum dots in an AlAs matrix form into a system with the dot density NQ_{Ds} higher than 10^{11} cm^{-2}, and a decrease in growth temperature leads to an increase in density and a decrease in dot sizes [5–8]. Because the growth temperature of our samples was lower than that in [7], whose authors report obtaining samples with $NQ_{Ds} = 7 \times 10^{11}$ cm^{-2}, we believe that the density of quantum dots in the system under study is at least not lower.

Transient and steady-state PL was measured. The excitation of PL was carried out by Ar^+, Ti : Sapphire, and semiconductor laser radiation, and the exciting photon energy was both larger and smaller than the bandgap of the AlAs matrix (E_g^{AlAs}). Steady-state PL was excited by Ar^+ laser radiation ($h\nu = 2.54$ eV > E_g^{AlAs}) or by a semiconductor laser with $h\nu = 1.82$ eV < E_g^{AlAs}. The excitation of transient PL was carried out by rectangular pulses of the semiconductor laser ($h\nu$ = 1.82 eV) or 200-fs pulses of a Ti : Sapphire laser ($h\nu$ =

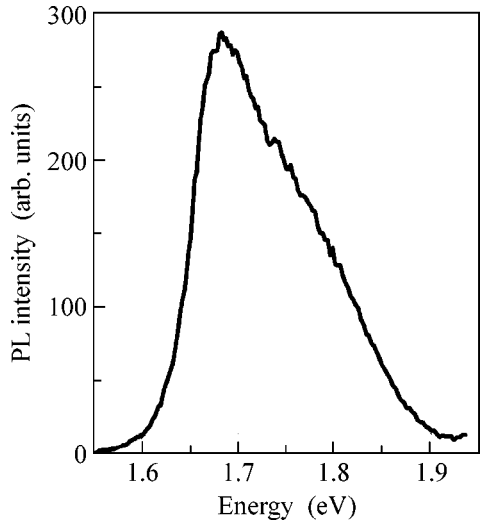

Fig. 1. PL spectrum of InAs/AlAs quantum dots at 4.2 K.

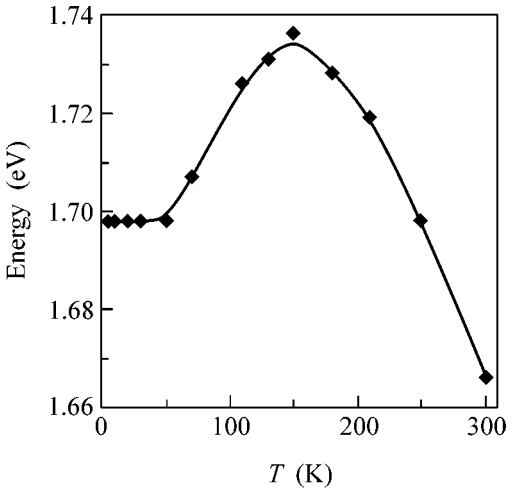

Fig. 2. Temperature dependence of the maximum position of the line caused by recombination in InAs/AlAs quantum dots. The solid line is a guide to the eye.

3.10 eV > E_g^{AlAs}) operating in the mode locking regime. The signal of steady-state and transient PL in the micro- and millisecond time range was recorded by a cooled photomultiplier with an *S*20 type photocathode operating in the photon counting regime. The measurement of PL kinetics in the submicrosecond time range was carried out by a Hamamatsu C4334 streak camera (time resolution, 15 ps) mounted on a CROMEX 250IS spectrometer.

It is seen in Fig. 1 that a line positioned at an energy of 1.684 eV and due to radiative recombination in quantum dots dominates in the steady-state PL spectrum of the structure with InAs/AlAs quantum dots measured at liquid-helium temperature with an excitation energy of 2.54 eV and an excitation density of 2 W cm^{-2}. An increase in excitation intensity leads to an increase in the half-width and to a short-wavelength shift of the line. Similar behavior of the line generated by recombination in InAs/AlAs quantum dots was observed previously in [6]. This behavior is due to the redistribution of charge carriers among quantum dots of different size in the system of closely packed, coupled quantum dots.

The temperature dependence of the position of the PL line maximum shown in Fig. 2 demonstrates a nonmonotonic character. The maximum position remains constant in the temperature range 4.2–50 K; as the temperature increases from 50 to 150 K, the line shifts toward the short-wavelength side; and with a further increase in temperature, the line exhibits a long-wavelength shift.

The photoluminescence kinetics of InAs/AlAs quantum dots at various temperatures is shown in Fig. 3. We note the following features of PL kinetics: (*1*) the shape of a kinetic curve and the duration of PL decay are independent of the exciting light photon energy and are similar for excitation with a photon energy of both larger and smaller than the bandgap width of the AlAs matrix; (*2*) the kinetics is of nonexponential character throughout the entire temperature range and is described by a power law $I(t, T) \sim (1/t)^{\gamma(T)}$; and (*3*) the duration of PL decay down to an intensity of 2.5×10^{-3} of the initial magnitude is independent of temperature in the range 4.2–50 K and equals at least 2 ms, as illustrated in Fig. 4. With increasing temperature, the duration of decay decreases by five orders of magnitude and becomes equal to 25 ns at 300 K.

It is evident in Fig. 4 that the integrated intensity of PL remains constant in the temperature range 4.2–210 K, which indicates that the sharp change in decay time with increasing temperature is not associated with the inclusion of additional channels of nonradiative recombination. A further increase in temperature up to 300 K leads to a decrease in integral intensity by a factor of 15 due to the thermal activation of charge carriers into the wetting layer and/or the AlAs matrix [6, 9].

The authors of [4] observed microsecond decay of the low-temperature (6 K) PL of InAs/AlAs quantum dots upon excitation by light with a photon energy exceeding the bandgap width of the AlAs matrix. In the model of recombination proposed in [4], it was suggested that the long decay of PL is explained by the spatial separation of charge carriers of different sign between neighboring quantum dots, which occurs because of electron scattering by the states of the *X* valley of the AlAs matrix in the process of electron energy relaxation.

The set of experimental data obtained in this work cannot be explained within the model proposed in [4]. Actually, upon exciting PL by light with a photon energy lower than the bandgap width of the matrix, the nonequilibrium charge carriers are excited inside a quantum dot and cannot reach the *X* valley of AlAs;

hence, the mechanism proposed in [6] is not realized. Moreover, this model does not contain temperature-dependent parameters and cannot explain the decrease by five orders of magnitude in the PL decay time with increasing temperature observed in our study.

In order to explain the millisecond PL kinetics observed in this work we took into account the fine structure of exciton levels strongly localized in quantum dots [10]. An exciton as a system of two paired spins can exist either in an optically active singlet state with a short radiative lifetime τ_C or in an optically inactive triplet state, which is characterized by a long lifetime $\tau_T \gg \tau_C$. Because of exchange interaction, the singlet and triplet exciton levels are split. The splitting Δ between the ground-state triplet and higher lying singlet exciton levels in three-dimensional semiconductor materials and large quantum dots is smaller than kT even at liquid-helium temperature. In this case, the kinetics of exciton PL is exponential and is characterized by the lifetime τ_C. However, for excitons strongly localized in small quantum dots embedded in a wide-bandgap matrix, as takes place for InAs quantum dots in an AlAs matrix, the splitting Δ strongly increases [11, 12]. In such a dot, in the absence of competing channels of charge carrier escape from the dot, the radiative lifetime of an exciton at low temperatures $kT < \Delta$ is determined by the exciton lifetime in the optically inactive triplet state τ_T.

In a system of isolated quantum dots with a spread of sizes, the dispersion of Δ values leads to a spectral dependence of the PL decay time [11]. A completely different pattern is observed in a system of locally coupled InAs quantum dots in an AlAs matrix. Because the distance between quantum dots is small, the wave functions of charge carriers in neighboring quantum dots strongly overlap; moreover, the potential barrier between dots can decrease locally [4, 7]. This leads to the migration of excitons from small dots to large ones. In this case, large dots with a small value of Δ and, hence, a short lifetime provide a channel for exciton recombination. At the same time, small dots with a large value of Δ and a long lifetime serve as a reservoir from which excitons find their way into large dots. In such a system of coupled quantum dots, the duration of PL decay in large dots is determined by the time during which excitons find their way from small dots into large dots rather than the radiative recombination time of excitons in a dot. It is evident that this time coincides in the order of magnitude with the lifetime of excitons in small dots. Because the lifetime values in dots of different size are randomly distributed over a wide range from τ_C to τ_T, the kinetic curve becomes nonexponential in shape. The power law of decay observed in this work is typical for decay processes characterized by a large set of characteristic lifetimes and was observed previously for the recombination of excitons localized at composition fluctuations in indirect-bandgap AlGaAs solid solutions [13]. An increase in temperature leads to

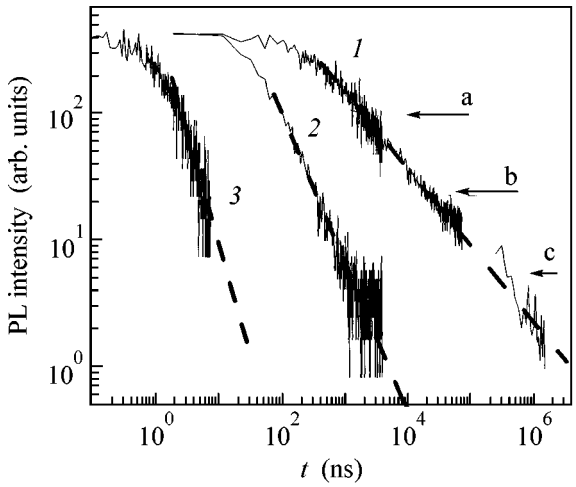

Fig. 3. PL kinetics of InAs/AlAs quantum dots at various temperatures (8, 150, and 300 K, curves *1–3*, respectively). Curves *2* and *3* were measured upon exciting PL by light with a phonon energy (3.10 eV) larger than the bandgap of the AlAs matrix. Curve *1* consists of three parts marked in the figure with arrows. In section (a) measurements were made by a streak camera, and PL was excited by light with a photon energy (3.10 eV) larger than the bandgap width of the AlAs matrix. In sections (b) and (c), PL was measured using a system of time-correlated photon counting, and PL was excited by light with a photon energy (1.82 eV) smaller than the bandgap width of the AlAs matrix. The dashed lines are guides to the eye.

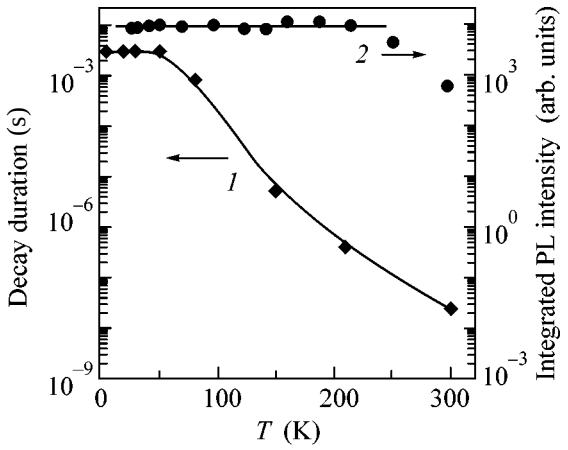

Fig. 4. Temperature dependences of (*1*) the duration of PL decay down to an intensity comprising 2.5×10^{-3} of the initial value and (*2*) the PL integrated intensity of InAs/AlAs quantum dots. Solid lines are guides to the eye.

an increase in the probability of exciton transfer between coupled dots and, simultaneously, to a decrease in the lifetime of excitons in small dots due to thermal activation from the triplet state to the singlet state. At high temperatures, when the condition $kT > \Delta$ is fulfilled in small dots, the PL decay time decreases down to the value of τ_C. The decrease in PL decay time

in the samples under study starts at temperatures exceeding 50 K; hence, the magnitude of singlet–triplet splitting must comprise at least several millielectron volts. Using the theory developed in [14] for crystals of T_d symmetry without regard for the long-range part of exchange interaction, we estimated the splitting Δ in small dots. Because InAs dots have a shape differing from a spherical one considered in [14], in our calculations we used the radius of a sphere with a volume equal to the volume of a real dot as the dot radius R. The obtained splitting $\Delta = 4.6$ meV agrees well with our experimental data.

The model of locally coupled quantum dots also provides an explanation for the temperature dependence of the PL line position. An increase in temperature results in an increase in the population of the optically active singlet state and, hence, in an increase in the probability of exciton recombination in small dots. This process leads to a redistribution of excitons among dots of different size. The short-wavelength shift of the PL line observed when the temperature increases in the range 50–150 K is thus due to an increase in the fraction of excitons recombining in the dots of smaller size. The long-wavelength shift of the line observed when the temperature increases above 150 K is due to a decrease in the bandgap of InAs and AlAs [6].

Thus, the transient and steady-state PL of self-assembled InAs quantum dots in an AlAs matrix has been studied in this work. Anomalously long millisecond nonexponential PL decay has been observed at low temperatures. The duration of decay significantly decreases as the temperature increases above 50 K and reaches a value of several nanoseconds at 300 K. The experimental results have been explained within the model of locally coupled quantum dots. The long decay at low temperatures is due to the singlet–triplet splitting of exciton levels in small quantum dots.

The authors are grateful to Dr. A.V. Efanov for fruitful discussion of the results.

This work was partially supported by grants of Volkswagen Foundation, project no. I/76 837; the Russian Foundation for Basic Research, project no. 01-02-16969; and the Ministry of Industry, Science, and Technology of the Russian Federation.

REFERENCES

1. Y. Arakawa and H. Sakaki, Appl. Phys. Lett. **40**, 939 (1982).
2. R. Heitz, A. Kalburge, Q. Xie, *et al.*, Phys. Rev. B **57**, 9050 (1998).
3. P. D. Buckle, P. Dawson, S. A. Hall, *et al.*, J. Appl. Phys. **86**, 2555 (1999).
4. P. Dawson, Z. Ma, K. Pierz, and E. O. Gobel, Appl. Phys. Lett. **81**, 2349 (2002).
5. D. A. Tenne, A. K. Bakarov, A. I. Toropov, and D. R. T. Zahn, Physica E (Amsterdam) **13**, 199 (2002).
6. U. H. Lee, D. Lee, H. G. Lee, *et al.*, Appl. Phys. Lett. **74**, 1597 (1999).
7. Z. Ma, K. Pierz, and P. Hinze, Appl. Phys. Lett. **79**, 2564 (2001).
8. P. Ballet, J. B. Smathers, H. Yang, *et al.*, J. Appl. Phys. **90**, 481 (2001).
9. L. Zang, T. F. Boggess, D. G. Deppe, *et al.*, Appl. Phys. Lett. **76**, 1222 (2000).
10. H. Fu, Lin-Wang Wang, and A. Zunger, Phys. Rev. B **59**, 5568 (1999).
11. P. D. J. Calcott, K. J. Nash, L. T. Canham, *et al.*, J. Phys.: Condens. Matter **5**, L91 (1993).
12. Al. L. Efros, M. Rosen, M. Kuno, *et al.*, Phys. Rev. B **54**, 4843 (1996).
13. M. V. Klein, M. D. Sturge, and E. Cohen, Phys. Rev. B **25**, 4331 (1982).
14. S. V. Gupalov and E. L. Ivchenko, Fiz. Tverd. Tela (St. Petersburg) **42**, 1976 (2000) [Phys. Solid State **42**, 2030 (2000)].

Translated by A. Bagatur'yants

JETP Letters, Vol. 77, No. 7, 2003, pp. 393–396. From Pis'ma v Zhurnal Éksperimental'noĭ i Teoreticheskoĭ Fiziki, Vol. 77, No. 7, 2003, pp. 464–467.

Quantum and Classical Binomial Distributions for the Charge Transmitted through Coherent Conductor¶

G. B. Lesovik[1] and N. M. Chtchelkatchev[1, 2]

[1] *Landau Institute for Theoretical Physics, Russian Academy of Sciences, Moscow, 117940 Russia*
e-mail: lesovik@landau.ac.ru

[2] *Institute for High Pressure Physics, Russian Academy of Sciences, Troitsk, Moscow region, 142092 Russia*
e-mail: nms@itp.ac.ru

Received February 27, 2003

We discuss controversial results for the statistics of charge transport through coherent conductors. Two distribution functions for the charge transmitted was obtained previously, one actually coincides with classical binomial distribution, the other is different, and we call it here quantum binomial distribution. We show that high-order charge correlators, determined by the either distribution functions, all can be measured in different setups. The high-order current correlators, starting with the third order, reveal (missed in previous studies) special oscillating frequency dependence on the scale of the inverted time flight from the obstacle to the measuring point. Depending on setup, the oscillating terms give substantially different contributions. © *2003 MAIK "Nauka/Interperiodica".*

PACS numbers: 05.60.Gg; 72.10.Bg

In last years, new direction has appeared in quantum transport investigations—description of the statistics of a charge transmitted through a quantum conductor. The distribution functions are usually investigated for a charge Q_{t_0} transmitted during a large interval of time through a certain cross-section of a conductor, and, what is essential, all observables are calculated from the first principles. Despite of the appreciable amount of articles (see the review [1]) and obtained results, some questions, in particular concerning the measurement theory, still remain unclear. One of the problems is that (in contrast to classical) the question arises in the quantum case of how to define the observable which should be calculated. Technically, this uncertainty is connected with the noncommutativity of the current operators at different times. As it appears, it is possible to present several definitions for the distribution function (DF) and characteristic function (CF) which (a) coincide in the classical case, (b) satisfy some general principles (in particular, correlators $\langle Q^n_{t_0}\rangle$ prove to be real), although lead to different answers in quantum case. It is possible to understand which definition is "correct" only after analysis of a definite setup for (at least gedanken) measurement.

In this paper, we consider several variants of measurements and the corresponding CF definitions. We will also comment the results obtained earlier. In the first paper devoted to the microscopic description of the distribution function [2], the following definition was adopted:

$$\chi(\lambda) = \langle \exp\{i\lambda\hat{Q}(t_0)\}\rangle = \left\langle \exp\left\{i\lambda\int_0^{t_0} dt\hat{I}(t)\right\}\right\rangle \quad (1)$$

(here, $\langle\ldots\rangle$ denotes the ensemble averaging). This definition is the most direct generalization of the classical definition; it differs only in the replacement of the charge and current observables by the appropriate operators. Performing calculations, we considered large time intervals at which the correlators $\langle\langle \hat{Q}(t_0)^n\rangle\rangle = \langle\langle \int_0^{t_0} dt_1 \ldots \int_0^{t_0} dt_n \hat{I}(t_1)\ldots\hat{I}(t_n)\rangle\rangle$ are approximately equal to

$$\langle\langle \hat{Q}(t_0)^n\rangle\rangle = t_0\langle\langle \hat{I}_0^n\rangle\rangle, \quad (2)$$

where $\langle\langle \hat{I}_0^n\rangle\rangle_0$ is the irreducible current correlator of the nth order at zero frequency limit (the irreducible correlators satisfy the equation $\langle \exp\{i\lambda\hat{Q}(t)\}\rangle = \exp\{\sum_{n=1}^{\infty}(i\lambda)^n\langle\langle \hat{Q}(t)^n\rangle\rangle/n!\}$).

The method of calculation used in [2] can be generalized to the case of finite temperatures, and (for normal single-channel conductors) we find

$$\chi(\lambda) = \exp\left\{t_0 g\int\frac{d\epsilon}{2\pi\hbar}\ln\{(1-n_L)(1-n_R) + n_L n_R + n_L(1-n_R)\chi_\epsilon(\lambda) + n_R(1-n_L)\chi_\epsilon(-\lambda)\}\right\}, \quad (3)$$

¶ This article was submitted by the authors in English.

where $\chi_\epsilon(\lambda) = \cos\{\lambda e\sqrt{T(\epsilon)}\} + i\sqrt{T(\epsilon)}\sin\{\lambda e\sqrt{T(\epsilon)}\}$, $g = 2$ is the factor taking into account spin degeneracy, T is the transparency, and $n_{L,R}$ are the filling factors in the left and right reservoirs, respectively. This distribution (at $k_BT = 0$, $eV \neq 0$) will be called *quantum* binomial distribution. In the multichannel case, $\chi(\lambda)$ is the product $\Pi_n\chi_n(\lambda)$ of the characteristic functions $\chi_n(\lambda)$ corresponding to the transmission eigenvalues T_n. The distribution function (3) formally describes fractional charge transport. In the indirect measurements of a charge in the solid-state systems, the fractional charge may, in principle, appear, for example, in the shot noise under the conditions of fractional quantum Hall effect [3]. In our case, the size "of a charge quantum" $2e\sqrt{T}$ is determined by the eigenvalue of the current operator, provided that it acts on the subspace of one-particle excitations with the given energy $e\sqrt{T} = \pm\langle\pm|\hat{I}(t_0)|\pm\rangle$, where the normalized one-particle excitations $|\pm\rangle$ satisfy the condition $\langle+|\hat{I}(t_0)|-\rangle = 0$; see also [2]. If we take into account the logarithmic, in time t_0, corrections to the irreducible correlators, then the exact charge quantization, which follows from the discrete distribution function, will be replaced, apparently, by small modulations in the continuous distribution function. If we restrict ourselves to the corrections (occurring from the vacuum fluctuations) to the pair correlator, then the distribution function becomes

$$P(Q) = \sum_n P^{(0)}(ne\sqrt{T})\left(\frac{2\pi}{G\hbar\ln\{t_0\omega\}}\right)^{1/2} \times \exp\{-(Q - ne\sqrt{T})^2/2G\hbar\ln\{t_0\omega\}\},$$

where $P^{(0)}(ne\sqrt{T})$ is the discrete distribution function without logarithmic corrections, G is the conductance, and ω is a characteristic frequency scale of the conductance dispersion.

Using Eq. (3), we find for the third-order correlator:

$$\langle\langle\hat{Q}^3_{t_0}\rangle\rangle = -t_0 g\int\frac{d\epsilon}{2\pi\hbar}e^3T^2(n_L - n_R) \times[\{3[n_L(1-n_R) + n_R(1-n_L)] - 1\} - 2T(n_L - n_R)^2].$$

At small voltage (and for energy-independent transparency T), the correlator is proportional to V^3, and at large V we get [2]

$$\langle\langle Q^3_{t_0}\rangle\rangle = -2e^3T^2(1-T)\frac{2eVt_0}{h}. \quad (4)$$

According to Eq. (2), the third-order current correlator at zero frequency is

$$\langle\langle I^3_0\rangle\rangle = -2e^3T^2(1-T)\frac{2eV}{h}. \quad (5)$$

Since it was not quite clear how one can measure *quantum* binomial DF and correlators of the type given in Eq. (4), it was suggested in [4] that a spin located near a wire can be used as the counter of electrons passed through it. Thus, it appears that the definition for CF in this case differs from (1) by the presence of time ordering:

$$\chi(\lambda) = \langle\tilde{T}\exp i\lambda/2\int_0^{t_0}\hat{I}(x)dt T\exp i\lambda/2\int_0^{t_0}\hat{I}(x)dt\rangle \quad (6)$$

in this (and only in this) formula, the symbol T means the usual time ordering, and $\tilde{T}$ means the ordering in the opposite direction.

It was found in [4, 5] (see also references in [1]) for the third-order correlator of the transmitted charge that

$$\langle\langle Q^3_{t_0}\rangle\rangle = e^3T(1-T)(1-2T)\frac{2eVt_0}{h}. \quad (7)$$

As we see, the third-order correlators (4) and (7) are essentially different. It would seem that there is nothing unexpected in such a distinction, because definitions (1) and (6) are different. However, for example, the third-order charge correlator, according to both definitions (1) and (6), actually contains the current correlator at small frequencies; but such a current correlator can be calculated with the help of the first definition (1) correctly in the zero-frequency limit (5), and it can be checked independently using the same technique as was used in [6] for the calculation of the pair correlator [7]. It appears that the dispersion of the third-order current correlator at small frequencies (along with the difference in the definitions) leads to different answers for the third-order correlators. Really, at frequencies $\omega \ll eV/\hbar$ and $x_{1,2,3} > 0$, we have

$$\langle\langle I_{\omega_1}(x_1)I_{\omega_2}(x_2)I_{\omega_3}(x_3)\rangle\rangle = 2\pi\delta(\omega_1+\omega_2+\omega_3) \times T(1-T)e^{i\omega_1x_1/v_F + i\omega_2x_2/v_F + i\omega_3x_3/v_F} \times[1 - 2T - e^{-2i\omega_2x_2/v_F}]eV\frac{2e^3}{h}. \quad (8)$$

For $x_1 = x_2 = x_3 = x$,

$$\langle\langle I_{\omega_1}(x)I_{\omega_2}(x)I_{\omega_3}(x)\rangle\rangle = 2\pi\delta(\omega_1+\omega_2+\omega_3) \times T(1-T)[1 - 2T - e^{-2i\omega_2x/v_F}]eV\frac{2e^3}{h}. \quad (9)$$

Formally, assuming that such a frequency dependence is correct for all frequencies, we find for the correlators in the time representation:

$$\langle\langle I(t_1,x)I(t_2,x)I(t_3,x)\rangle\rangle = eV\frac{2e^3}{h}T(1-T) \times \mathrm{Sym}([1-2T]\delta(t_i-t_j)\delta(t_j-t_k) - \delta(\tilde{t}_i-\tilde{t}_j)\delta(\tilde{t}_j-\tilde{t}_k)), \quad (10)$$

where the symbol Sym means symmetrization in the indices $i \neq j \neq k$; $\tilde{t}_2 \equiv t_2 + 2x/v_F$, $\tilde{t}_1 = t_1$, $\tilde{t}_3 = t_3$ (if a real frequency dependence is taken into account instead of the δ functions, there should stand functions which decay with characteristic times $t \sim \tau_0$,[1] but, for simplicity, we will describe the case with δ functions). Substituting this expression into the expression for the third-order charge correlator which follows from Eq. (6), we get

$$\langle\langle Q_T^3\rangle\rangle = \frac{3}{4}\left[\int_0^T dt_1\int_0^T dt_2\int_0^{t_2} dt_3 + \int_0^T dt_2\int_0^{t_2} dt_1\int_0^T dt_3 + \int_0^T dt_1\int_0^{t_1} dt_2\int_0^{t_2} dt_3 + \int_0^T dt_3\int_0^{t_3} dt_2\int_0^{t_2} dt_1\right]\langle\langle I(t_1)I(t_2)I(t_3)\rangle\rangle, \quad (11)$$

and, integrating over times, we find for finite x the answer (7) proportional to $T(1-T)(1-2T)$, which is typical of the *classical* binomial distribution (the same phenomenon takes place for other irreducible high-order correlators).

This occurs because the terms in the Eq. (10) containing δ functions depending on $\tilde{t}_i$ do not make contribution to the answer, because they are nonzero only when, simultaneously, $t_3 > t_2$ and $t_1 > t_2$ and the integration volume in Eq. (11) does not cover this sector. Consider, e.g., the contribution to the correlator $\langle\langle Q_T^3\rangle\rangle$ from the term in Eq. (10) proportional to

$$\delta(\tilde{t}_1 - \tilde{t}_3)\delta(\tilde{t}_3 - \tilde{t}_2) = \delta(t_1 - t_3)\delta(t_3 - t_2 - 2x/v_F). \quad (12)$$

From Eq. (12) it follows that the region where $t_1 \approx t_3 \approx t_2 + 2x/v_F$ in Eq. (11) should give the leading contribution to the integrals. But from the requirement $x > 0$ it follows that $t_3 > t_2$ and $t_1 > t_2$. The region defined by these inequalities does not overlap with the integration volume in Eq. (11); thus, contribution (12) to $\langle\langle Q_T^3\rangle\rangle$ is zero. Similarly, it is possible to show that all terms proportional to $\delta(\tilde{t}_i - \tilde{t}_j)\delta(\tilde{t}_j - \tilde{t}_k)$ in Eq. (10) do not make contribution to $\langle\langle Q_T^3\rangle\rangle$ at $x > 0$.

One can say that, when the incident wave packet first completely passes through the detector and, with a time delay, a part of the wave packet reflected from the barrier goes back through the detector, the specific quantum interference disappears and the answer (7) is true. But if the distance to the detector is small, the incident wave packet interferes with the reflected wave in the measurement region, leading eventually to the answer (4). So, Eq. (7) is true when the electron-flight time from the scatterer to the spin of the detector situated at the distance d from the wire and L from the scatterer is larger than the decay time τ_0 of the correlators. If these requirements are violated, the answer will be different. In the calculations described in [4], although it was formally assumed that the distance L is zero, the limit was considered where L actually exceeded the wave-packet size (which was also set equal zero).

For the case where the spin detector is located near the scatterer $x \ll v_F\tau_0$ and close to the wire $d \ll v_F\tau_0$, the answer for $\langle\langle Q_{t_0}^3\rangle\rangle$ is proportional to $-T^2(1-T)$ and it coincides with the answer (4) obtained from the quantum distribution. Indeed, using the general expression for the correlator (8) at $x_{1,2,3} \ll v_F\tau_0$ we get

$$\langle\langle I_{\omega_1}(x_1)I_{\omega_2}(x_2)I_{\omega_3}(x_3)\rangle\rangle \simeq -2\pi\delta(\omega_1+\omega_2+\omega_3)2T^2(1-T)eV\frac{2e^3}{h}. \quad (13)$$

Using this expression at $\omega \ll eV/\hbar$ and the definition (11), we obtain the expression for $\langle\langle Q_{t_0}^3\rangle\rangle$ proportional to $-T^2(1-T)$, as well as in the calculation with the use of CF (1).

The measurement with spin basically can be implemented in practice with the help of muons, which can be trapped near the conductor, and then the measurement of the direction of their decay would give the angle of their spin rotation in a magnetic field. As an additional example of the measuring procedure that, basically, can be implemented practically, we have analyzed the measurement of the irreducible charge correlators with the help of an ammeter represented by a semiclassical system (for example, an oscillatory circuit) weakly interacting with the current in a quantum conductor. The ammeter state is characterized by the magnitude ϕ. The interaction of the ammeter with a quantum conductor is described by the interaction Hamiltonian $H_i = \lambda\phi\hat{I}(t)$, where λ is the interaction constant, $\hat{I}(t)$ is the current operator in a quantum conductor, and $\hat{I}(t) = \int\hat{I}(t, x)f(x)dx$ (we do not take into account the retardation effects); thus, the area of integration is determined by some kernel $f(x)$. Correlators ϕ are expressed through the current correlators in a quantum conductor as follows:

$$\langle\langle(\phi(t))^n\rangle\rangle = \left(-\frac{\lambda}{2}\right)^n\int_c d\tau_1\ldots d\tau_n\kappa(|t-\tau_1|) \times \mathrm{sgn}(t-\tau_1)\ldots\kappa(t-\tau_n)\,\mathrm{sgn}(t-\tau_n) \times\langle\langle T_c I(\tau_1)\ldots I(\tau_n)\rangle\rangle, \quad (14)$$

where the integration is performed along the usual Keldysh contour, and $\kappa(\tau)$ is the ammeter susceptibility. In the specific case where the ammeter represents an oscillator, the equation of motion for ϕ is $\ddot{\phi} + \gamma\dot{\phi} +$

[1] Characteristic time scale of the correlator decay can be estimated as $\tau_0 \sim \hbar/eV$. We will consider the time dependence of the correlators in detail in a separate article.

$\Omega^2\phi = \lambda I(t)/M$; the susceptibility $\kappa(\tau) = \Theta(t)\exp(-\gamma t/2)\sin(\tilde{\Omega}t)/M\tilde{\Omega}$, where $\tilde{\Omega} = \sqrt{\Omega^2 - \gamma^2/4}$. The case $\gamma \approx 2\Omega$, $\gamma \ll 1/\tau_0$ is the most interesting to us. Then,

$$\langle\langle \phi^3(0)\rangle\rangle \approx \langle\langle I_0^3\rangle\rangle \lambda^3 \int \frac{d\omega_{1,2,3}}{(2\pi)^3} \kappa(\omega_1)\kappa(\omega_2)\kappa(\omega_3) \times \delta(\omega_1 + \omega_2 + \omega_3) = \frac{2}{27}\frac{\langle\langle I_0^3\rangle\rangle \lambda^3}{M^3\Omega^4}, \quad (15)$$

$$\langle\langle \phi^n(0)\rangle\rangle \approx \frac{n!}{n^{n+1}}\frac{\langle\langle I_0^n\rangle\rangle \lambda^n}{M^n\Omega^{n+1}}, \quad (16)$$

where $\langle\langle I_0^n\rangle\rangle$ is the irreducible current correlator of order n, defined by the quantum binomial distribution [in Eq. (16), we neglected the contribution from the own thermal ammeter noise].

Thus, by measuring *irreducible* correlators of coordinate ϕ of the ammeter, it is possible to measure the irreducible high-order current correlators in the zero-frequency limit (in particular, $\langle\langle I_0^3\rangle\rangle \propto -T^2(1 - T)$). Such measurements are possible also for less restrictive requirements on the ammeter frequencies if the kernel $f(x)$ defines the area of an integration so that $x \ll v_F\tau_0$. In the opposite limit, it is natural to expect "classical" answers for the correlators (in particular, $\langle\langle I_0^3\rangle\rangle \propto T(1 - T)(1 - 2T)$).

We are grateful to M. Reznikov and, especially, to D. Ivanov for fruitful discussions. D. Ivanov paid our attention to the special coordinate and frequency dependence of the third-order correlators which proved to be important for reviewing various conditions of measurement. We are also grateful to M. Feigelman for reading manuscript and useful remarks.

This work was supported by the Russian Science Support Foundation, the Russian Foundation for Basic Research, the Russian ministry of science (the project "Physics of quantum computations"), and SNF (Switzerland).

REFERENCES

1. L. S. Levitov, cond-mat/0210284.
2. L. S. Levitov and G. B. Lesovik, Pis'ma Zh. Éksp. Teor. Fiz. **55**, 534 (1992) [JETP Lett. **55**, 555 (1992)].
3. C. L. Kane and M. P. A. Fisher, Phys. Rev. Lett. **72**, 724 (1994); L. Saminadayar, D. C. Glattli, Y. Jin, *et al.*, Phys. Rev. Lett. **79**, 2526 (1997); R. de-Picciotto, M. Reznikov, M. Heiblum, *et al.*, Nature **389**, 162 (1997).
4. L. S. Levitov and G. B. Lesovik, cond-mat/9401004; L. S. Levitov, H. W. Lee, and G. B. Lesovik, J. Math. Phys. **37**, 4845 (1996).
5. L. S. Levitov and G. B. Lesovik, Pis'ma Zh. Éksp. Teor. Fiz. **58**, 225 (1993) [JETP Lett. **58**, 230 (1993)].
6. G. B. Lesovik, Pis'ma Zh. Éksp. Teor. Fiz. **49**, 513 (1989) [JETP Lett. **49**, 592 (1989)].